Université Libanaise
École Doctorale
Sciences et Technologies

UNIVERSITAT
POLITÈCNICA
DE VALÈNCIA

THESE de doctorat en Cotutelle

Pour obtenir le grade de Docteur délivré par

L'Université Libanaise

L'Ecole Doctorale des Sciences et Technologie

et

l'Université Universitat Politècnica de València

Mohamad Hassan Haroun

16-Juin-2019

Système du réseau d'antennes 8×1 pour le Beamforming de liaison montante dans les technologies LTE-A et 5G NR

8×1 Antenna Array System for Uplink Beamforming in LTE-A and 5G NR

Directeur de thèse **: Jalal Jomaa et Marta Cabedo Fabres**

Co-encadrement de la thèse **: Hussam Ayad**

I would like to dedicate this thesis to my loving parents, my sacrificing faithful wife and my little boys Ali and Taha

Acknowledgements

First and foremost, I would like to thank Almighty God.

I would like to express my sincere gratitude to my advisors Prof. Jalal Jomaa, Prof. Marta Cabedo Fabres, Dr. Hussam Ayad, and Prof. Miguel Ferrando Bataller for their support all over the thesis development time.

I would also like to thank my thesis reviewers Prof. Youssef Nasser, Dr. Elias Rachid, Dr Eva Rajo, Dr. Otman Aghzout, and the rest of my thesis committee: Prof. Mohammad Rammal and Dr. Amer Baghdadi for their time to review my work and their remarkable suggestions to improve it.

I am grateful to all of those who gave me love and support for my entire life and during my thesis. I'd like to thank my parents for all their unconditioned giving. Thanks to my lovely wife Hawraa, thanks for all the sacrifices, patience and support and I'd like to tell her that I truly find her a partner in the accomplishment of this thesis.

Also, I wish to thank my mentor Dr Ali Rahal for all his assistance. Thanks to my true friend Tarek Chehade for being there whenever I asked or sought help. My thanks and gratitude for my friend Dr. Abbas El Mestrah.

Contents

List of Figures

List of Tables

Abstract

Phased array technology made a turnover in radar industry decades ago. Nowadays, phased array, or beamforming, is becoming a necessity for digital communication. Exploiting beamforming would help in reducing the overall power consumption of base stations and user equipment. It will also enables the service to provide much higher datarates and enhance the quality of service.

Research on digital beamforming and communication requires antenna array and compatible hardware. The hardware should be capable of handling different scenarios and approaches for mobile communication problems. There are several systems used for beamforming research especially for mobile communication. These systems suffer from several deficiencies. They are either expensive to implement, not adaptive and fixed to an architecture related to certain beamforming algorithm or with fixed array elements number.

In this thesis, a new phased array system is proposed. This system could be exploited for research in mobile communication or radar problems. It is composed of 8x1 planar antenna array, RF to baseband conversion channels and base band processor. Beamforming and DOA estimation is done on base band digital samples. This provides the system with dynamicity regarding tested algorithms. For that purpose, agile SDR boards are used to acquire signals from antenna array and convert them to digital data streams. Data streams are then processed in an FPGA based base band processor. In addition to being low in cost and affordable by small research institutes and freelancing researches, the system can be adjusted to carry more antenna array elements.

The 8x1 planar monopole array is designed, simulated and measured. Impedance matching and radiation characteristics are plotted and described. SDRs are introduced and calibrated for multi-element operation and calibration method for phase and amplitude uncertainties are introduced. Overall system performance is tested by different beamforming algorithms and direction of arrival estimation algorithms. Measurement results show that the system is reliable. Beamforming with good resolution and high interference rejection is achieved. Direction of arrival estimation is accurate.

Resumen

La tecnología de matriz en fase hizo una rotación en la industria del radar hace décadas. Hoy en día, la matriz en fase, o formación de haz, se está convirtiendo en una necesidad para la comunicación digital. La explotación de la formación de haz ayudaría a reducir el consumo de energía general de las estaciones base y el equipo del usuario. También permitirá que el servicio brinde datos mucho más altos y mejore la calidad del servicio.

La investigación sobre la formación y comunicación de haces digitales requiere un conjunto de antenas y hardware compatible. El hardware debe ser capaz de manejar diferentes escenarios y enfoques para problemas de comunicación móvil. Hay varios sistemas utilizados para la investigación de conformación de haz, especialmente para la comunicación móvil. Estos sistemas sufren de varias deficiencias. Son costosos de implementar, no adaptativos y fijos a una arquitectura relacionada con cierto algoritmo de conformación de haz o con un número de elementos de arreglo fijo.

En esta tesis, se propone un nuevo sistema matricial por fases. Este sistema podría ser explotado para la investigación en comunicaciones móviles o problemas de radar. Está compuesto por un conjunto de antenas planas de 8x1, canales de conversión de RF a banda base y procesador de banda base. La formación de haz y la estimación de DOA se realizan en muestras digitales de banda base. Esto proporciona al sistema dinamismo con respecto a los algoritmos probados. Para ese propósito, las tarjetas SDR ágiles se utilizan para adquirir señales de la red de antenas y convertirlas en flujos de datos digitales. Los flujos de datos se procesan en un procesador de banda base basado en FPGA. Además de ser de bajo costo y asequible para los pequeños institutos de investigación e investigaciones independientes, el sistema se puede ajustar para llevar más elementos de la red de antenas.

El conjunto monopolo plano 8x1 está diseñado, simulado y medido. La correspondencia de impedancia y las características de radiación se representan y describen. Los SDR se introducen y se calibran para la operación de elementos múltiples y se introducen los métodos de calibración para las incertidumbres de fase y amplitud. El rendimiento general del sistema se prueba mediante diferentes algoritmos de conformación de haz y algoritmos de estimación de la dirección de llegada. Los resultados de las mediciones muestran que el sistema es confiable. Se logra una conformación de haz con buena resolución y alto rechazo de interferencia. Dirección de estimación de la llegada es precisa.

Resum

La tecnologia en fases de paquets es va convertir en dècades enrere en la indústria del radar. Avui en dia, la matriu de fases o la formació de bigues s'està convertint en una necessitat per a la comunicació digital. L'explotació d'un sistema de transmissió de feixos ajudarà a reduir el consum total d'energia de les estacions base i dels equips d'usuaris. També permetrà al servei oferir dades molt més elevades i millorar la qualitat del servei.

La investigació sobre la comunicació digital i la comunicació requereix una antena i un maquinari compatible. El maquinari hauria de ser capaç de gestionar diferents escenaris i enfocaments per a problemes de comunicació mòbil. Hi ha diversos sistemes utilitzats per a la investigació de la formació de bigues, especialment per a la comunicació mòbil. Aquests sistemes pateixen de diverses deficiències. Són cares d'implementar, no adaptatives i fixades a una arquitectura relacionada amb determinat algorisme de generació de feixos o amb un nombre d'elements d'array fix.

En aquesta tesi es proposa un nou sistema de matrius per fases. Aquest sistema es podria explotar per a la investigació en problemes de comunicació mòbil o radar. Està compost per una xarxa d'antenes planes de 8x1, canals de conversió de RF a banda base i processador de banda base. Es fa una estimació de la transformació de fases i de la DOA en mostres digitals de banda base. Això proporciona al sistema dinàmica quant als algorismes provats. Amb aquesta finalitat, es fan servir juntes SDR àgils per adquirir senyals de la matriu d'antenes i convertir-les en fluxos de dades digitals. Els fluxos de dades es processen després en un processador de banda base basat en FPGA. A més de ser baixos en costos i assequibles per part de petits instituts d'investigació i investigacions independents, el sistema es pot ajustar per portar més elements de matriu d'antenes.

La matriu monopola plana de 8x1 està dissenyada, simulada i mesurada. Es combinen i descriuen les característiques d'impedància i de radiació. Els SDR s'introdueixen i es calibren per al funcionament de diversos elements i s'introdueixen els mètodes de calibratge per incerteses de fase i amplitud. El rendiment global del sistema es prova mitjançant diferents algorismes de formulació de feixos i algorismes de direcció d'estimació d'arribada. Els resultats de la mesura mostren que el sistema és fiable. S'aconsegueix un model de beamformació amb bona resolució i un rebuig elevat de la interferència. La estimació de la direcció d'arribada és precisa.

Chapter 1 State of the Art

Beamforming, supported by phased arrays, had attained a great contribution in research and industry for the few past decades. Phased Array is said to be a group of antennas in which the relative phases of the respective signals feeding the antennas are varied in such a way that the effective radiation pattern of the array is reinforced in a desired direction and suppressed in undesired directions[1].

Phased arrays are used for three main purposes:

1. Produce narrow beams with low side lobes and back lobes levels.
2. Make a steerable main beam to have the maximum gain in the direction of interest.
3. Increase the immunity toward coherent interferers by adding nulls in the interferers' directions.

Phased arrays are essential contributors in a lot of essential domains and fields. They promise to have a great future in the domain of anti-accident radars. Such radars provide information about traffic situations ahead of the car, thus making it possible to react to altered traffic conditions by accelerating, braking or changing gear [2].

One of the most common applications of phased array antennas are the military radar systems. Phased arrays give a big added value to the military radar systems. Phased arrays enhance a military platform's mission effectiveness by providing reduced radar cross section (RCS) relative to reflector-based implementations. Also, it increases flexibility via simultaneous multi-beam operation, increased mean time between failure (MTBF), and increased operational availability resulting from graceful degradation [3]. For example of the effectiveness of phased arrays in military radar applications, Lockheed Martin NE and SS-Moorestown, under sponsorship of the Office of Naval Research, completed a series of land-based and at-sea exercises that demonstrated the ability of U.S. Navy tactical phased array radar to make accurate spectral moment measurements using the “*Tactical Environmental Processor (TEP)*” for meteorological community [4].

Phased arrays, and in addition to their big contribution in the development of military radar systems, are widely used in the mobile telecommunication field. The utilization of phased arrays in base stations of mobile networks improved co-channel interference, regulated fading via scanning, decreased transmitter power, and higher system capacity. By feeding each of the radiating elements with the appropriate channel dependent phase shift, narrow beams can be activated to simultaneously track and communicate with multiple mobile users [5]. In addition, using multi-beam phased arrays lead to the decrease in cell size which means that a larger number of mobile users can be concentrated in a smaller area without increasing spectrum allocation [6].

Phased arrays appeared as a solution for practical problems concerned with mechanically moving the antennas, especially in radars and early warning systems so beams where electronically steered instead of mechanically rotating the reflectors.

Scanned array term was first used by Friis. Friis, and after several investigations about directional antennas for short waves, has proposed an antenna similar to the rotatable loop antenna in which antennas are fixed and balance is obtained by phase shifting the received signals. This antenna was used to find the direction of arrival of short waves [7].

Friis continued his work and then designed a receiving system employing sharp vertical plane directivity, capable of being steered to meet the varying angles at which short radio waves arrive at a receiving location. This system comprises six rhombic antennas extending three quarters of a mile along the direction [8]. Bell Laboratories research and development didn’t stop and finally gave birth to the first *phase array radar,* This Bell Labs S-Band system used end-fire Poly-rod elements with mechanically driven phase shifters to provide rapid sector scan [9].

There has been much talk about the transfer of military technology to the commercial world, especially with the end of the cold war.

Here arises a very important question. Why this technology is needed to be available in modern mobile communication standards?

Exploiting beamforming in mobile communication would:

1. Increase SNR levels in uplink and downlink.
2. Antenna gain in the direction of interest is maximized, this would for sure minimize the need for high gain amplifier stages for transmission and reception in the mobile equipment which will consequently increase the battery operation time in a big factor.
3. The beamforming system would be able to cancel out interferences especially that the bands in which LTE operates are also used by other standards (i.e. Wi-Fi).
4. Increase the maximum range for base stations.
5. In mobile communication, the mobile user equipment is expected to be always in motion. Beamforming system would offer the base station the ability to track mobile equipment and meanwhile conserve a good quality of service.

Using beamforming in telecommunication is not new and took a lot of researchers' interest. A base station is equipped with an adaptive antenna array processor that allows in every GSM frame full beam adaptation in uplink and downlink is proposed and tested in [10]. Performance analysis of a smart antenna base station that has been implemented for CDMA-2000 system in [11]. a simple antenna array-based MC-CDMA receiver that combines efficient blind adaptive beamforming based on maximum signal-to-interference-and-noise ratio (MSINR) criterion with parallel interference cancellation (PIC) for an MC-CDMA uplink system is proposed in [12].

In addition to the research conducted on using beamforming and phased arrays for mobile communications, several projects did really deploy base stations with this feature. ArrayComm, a leading company in mobile communications, implemented a smart base station for GSM base stations which were named Intellicell. Intellicell has been deployed in 275000 GSM base stations in USA, Japan, Australia, South Africa, Thailand, Middle East and Philippines [13]. Another project for Metawave Company that has been shut down in 2002 is called Spot Light.

Spot light exploits switched beams and not adaptive antenna arrays. Metawave also developed another project, Smartcell that fit for CDMA, GSM, TDMA, CDMA-2000 and W-CDMA. Also, Quantenna Company made its commercial solution that uses a 4-element antenna array in a 802.11n Wi-Fi router [14].

All those examples were out of standard. These standards for mobile communication didn't discuss exploiting beamforming for the operative networks. For the most recent communication standard, this is changed. The latest release of the well-known wifi 802.11 protocol (802.11ac) has included the use of beamforming in 802.11ac routers [15]. Many products were manufactured for 802.11ac standard with beamforming capabilities. One of which is the apple "AirPort Extreme" router.

Despite MIMO has been included in LTE standard in the 8th release of 3gpp [16], beamforming has not been included until the 10th release of 3gpp [17]. This standard did not make restriction on number of antenna array elements or beamforming algorithm. So, it can choose the best choices that fit the system specifications.

Mobile telecommunication market is growing very fast which requires continuous upgrade of the providers' infrastructure. Mobile communication standards had passed through several evolution steps starting from GSM till the eagerly awaited revolutionary fifth generation (5G). Diversity techniques were introduced to help increase the SNR and though the quality of service for the mobile users. These include time diversity, frequency diversity and spatial diversity. Beamforming, that has been a well-known technique in defence radio systems, was recently exploited in mobile communication. Beamforming can be thought of as a space multiplexing way. In addition to the advantages stated previously, beamforming capable base stations would handle spectrum sharing feature. Two different communication protocol devices operating at the same frequency will not interfere with each other since each of them can place nulls in the direction of the other in its beam pattern.

For Long Term Evolution (LTE), beamforming was introduced in the 3GPP release 10 [17]. The standard supports passive arrays with horizontal beamforming and active arrays with 2D and 3D beamforming capabilities. Beamforming is getting more and more important in the latest releases of 3GPP. In Release 15, the proposed 5G New Radio (NR) relies on beamforming and beam management [18]. In 5G NR description, the specification states the possibility of exploiting beamforming in the uplink and downlink transport channels [19]. Despite beamforming specifications not being final yet, some potential beamforming related requirements were discussed such as null suppression and steering angle range [20]. 3GPP and the telecommunication community is giving beamforming a great attention for its promising expectations to increase the target number of users and decrease significantly the cost of services.

In the development process of such beamforming methods and techniques, the testing phase is one of the most essential and indispensable, and researchers are often confronted with several obstacles related to this phase.

a) Analog beamforming arrays are algorithm specific. Arrays beamforming networks are designed according to the topology of a specific beamforming algorithm. It is almost impossible to test new algorithms on an existing analog beamforming system.
b) Bulky size of the testbed that makes it hard to move it between test house and field trials.
c) High cost of measurement equipment renting and fees in case of research being conducted by academic institutes.
d) High cost of beamforming implementation using high end transceivers designed for phased array applications.
e) Fixed number of antenna array elements since beamforming network is designed according to a specific number of antenna elements.

Several beamforming arrays were proposed and used before. In [21], a switched array beamforming system is proposed and design which exploits a single RF receiver with sequential weighting of the 8 element linear array. Although this approach would save implementation cost and design complexity, this system needs an ultra-high-speed ADC, 8 times faster than ordinary, to handle coherent signals digitization and sampling. A complete beamforming system is presented in [22]. Inverted L -probe fed Microstrip patch antenna array is designed and an RF-frontend. The system suffers from 2 main issues. The antenna array is designed to handle 4 elements array and is not flexible to add more elements on the go. In addition, the processing unit used is a DSP which is weak relative to available FPGA digital boards. Realistic implementation of beamforming for UMTS is presented in [23]. The system is designed specifically to UMTS CDMA and is not flexible for telecommunication protocol. An eight-element, 2–16-GHz, programmable phased array receiver in a 0.13-µmSiGe BiCMOS package is designed in [24]. The work represents a wide band beamforming receiver for current and future telecommunication protocols. On the other hand, the system is totally analog and lacks computation gain and flexibility that digital beamforming provides. A smart small cell with hybrid beamforming for 5G is proposed and a prototype is built in [25]. Despite that the testbed was based on LTE, it illustrates the concept of beam management 5G NR is promising to handle. Nevertheless, this system is expensive as it requires small scale Virtrex FPGA boards and NI platform dedicated for data aggregation.

On the other hand, the big telecommunication development companies are leading the way in 5G NR research as they already have testbeds well designed for testing purposes. Ericsson researchers has conducted several beamforming trials for 5G using high end testbeds [26] [27] [28] [29] [30]. NTT Network Innovation Laboratories with Nokia Networks performed several field experiments on the downlink throughput and SNR performance of a beam forming 5G millimetre wave radio access system with beam tracking in a street canyon and a shopping mall [31] [32]. Also, Network Innovation Laboratories with Samsung Electronics Co. Ltd conducted several experiments to evaluate the effectiveness of using 28 GHz band with super-wide bandwidth of 800 MHz for 5G mobile communication systems. [33]. NTT Network Innovation Laboratories with Ericsson tested successfully tracking the position and movements of a given device and pointing one or more beams in the best direction for that device in real time in [34]. A team from China Mobile Communications Corporation made real field tests in urban areas to study the effectivity of exploiting elevation beamforming [35].The big resources and R&D fund those big companies have and on the other hand the limited funding for academic research laboratories make the academic institutes contribution in the development of LTE-A and 5G

NR beamforming limited. From here arises the need to have a system accessible by researchers and have the following strength points:

1. Dynamicity regarding the number of input channels and though number of antenna elements exploited in the phased array beamforming.
2. Algorithm Flexibility and the ability to implement any beamforming or DOA estimation algorithm efficiently and study their performance in real field trials.
3. Compactness in order for the researcher to be able to move the testbed between test house and field.
4. Low implementation cost.
5. Digital Beamforming, in which beamforming is implemented on baseband samples.

National Instruments have developed a modular testbed for Massive MIMO research for mobile communications applications [36]. The system is already used in wireless technology research [37]. The testbed can support up to 128 antenna elements and is programmable also through NI LabVIEW environment and supports phase calibration through a common 10MHz reference clock distribution network. This system, on the other hand, is not dedicated to the digital beamforming research field. Rather, its focus is on MIMO precoding and decoding and on channel estimation and equalization. In addition, it is based on USRP RIO Software Defined Radios (SDRs) with approximately 8000 USD per SDR card or 4000 USD per element. Another testbed, ARGOS, that can support up to 64 antenna array elements was demonstrated in [38]. The system’s hardware and calibration are described. This system focuses on multiuser beamforming for multiuser mobile communication and serves as a base station for mobile communication. Several researches at Rice University were then conducted exploiting ARGOS. One of them is a development of self-interference suppression method using digital beamforming instead of classical analog beamforming[39]. ARGOS is a scalable and modular system based on Wireless Open-Access Research Platform (WARP), developed by mangocomm engineers, adaptable and programmable according to the application being performed. Nevertheless, the system is expensive. Each WARP SDR, with 2 channels, cost around 4900 USD which is about 2450 USD per element. In addition, the hardware operates only at 2.4GHz and 5GHz while the proposed testbed operates from 60MHz to 6GHz.

In this Thesis, we propose a novel testbed for beamforming and DOA estimation algorithms evaluation for LTE-A and 5G. Based on SDR, beamforming is performed in the base band digital domain thus the testbed is flexible. Various algorithms could be evaluated by software modifications and without the need to change the expensive radio hardware. Having a compact size, this testbed could be transported between anechoic chamber, open space areas, urban areas and condensed urban areas and hence provide a controlled versus non-controlled experiments for performance analysis. After all, the testbed relies primarily on an agile wide band transceiver, AD9361, from Analog Devices. This transceiver is a mid-range commercial product intended for wireless networks applications. In addition, the antenna array is a planar monopole array that is printed on Rogers substrate and backed with low cost metallic reflector. These two factors keep the total cost of the system very low.

This will allow researchers from academic institutes to test steering capability, null suppression, sidelobe suppression and multibeam formation in various beamforming algorithms. This work is based on performing the beamforming in the baseband digital domain.

Chapter 2 Beamforming and Phased Arrays

In signal reception system design, several possible diversity techniques, such as time, frequency, and space diversities, can be used to obtain satisfactory signal reception performance even under harsh operation environments. For the space diversity technique, diversity is achieved basically using multiple sensors, arranged in a certain pattern, which is known as an array. The use of an array has long been an attractive solution for many applications such as sonar, radar, communications, and seismology. Particularly, because of the explosion of wireless communication applications such as land mobile and wireless local loop (WLL) communications, spatial filtering is of great interest to the wireless communication system designers to achieve space division multiple access (SDMA). In spatial filtering, the objective of using an array is to extract the desired signal copy while filtering out the unwanted interference, and environmental and system noise. This filtering in the spatial domain using an array is also known as array beamforming. In digital signal processing, filtering can be broadly classified into filter synthesis and adaptive filtering. As for array beamforming, it can also be divided into two types: array synthesis and adaptive array beamforming. Generally, adaptive array is able to provide better signal reception as compared with the synthesized array. This is because the adaptive processing of an array is performed on a signal data dependent basis or as a statistically optimum process, whereas the synthesized array always has a set of fixed weights that produces a fixed array response. However, this does not suggest that the adaptive array is always preferred as compared with the synthesized array because an adaptive array system is a costlier system, in the sense that a fast speed computing machine is required to calculate and adjust the array weights according to the data collected. For a special class of array synthesis, the desired array beam pattern may even be achieved, which involves no signal weighting at all, by arranging the array in a certain geometric pattern. Although adaptive beamforming techniques have been in existence for many years, there is still a major obstacle on the route to practical implementation. The problem is, when a physical sensor array is constructed, the array manifold associated with the array is always not completely known. Therefore, the estimation of array manifold parameters to minimize array uncertainties could pose a problem in the design of a modern array system. Signal cancellation, resulting from multipath or correlated signals, could also be a problem in some adaptive array processing algorithms. In many cases, a switched beam system is preferred as compared with a fully adaptive antenna array system (such a system is also known as Smart Antennas), because of its simplicity in the system itself and retrofitting to existing wireless communication technologies. In a switched beam system, a number of fixed beams are used at the base station or an antenna site. On receiving a signal, the receiver selects a beam to perform spatial filtering so as to provide the best signal enhancement while suppressing the interferences and noise. Besides its importance in switched beam system design, beam pattern synthesis is also an issue in the adaptive array system, or smart antenna system. This is because when an adaptive array is turned on, before it adjusts its weights according to the signal environment, its array weights have to be initialized while the array is adapting or being trained. One possibility is for the array to be initialized to certain presynthesized weights. In cases where a quiescent pattern is required, array synthesis techniques can be used to design such quiescent patterns.

2.1 Array Fundamentals

Array synthesis is a very interesting important concept. The array is made to have a radiation pattern with maximum gain at a direction, specific side lobe level, interference rejection and even combination of these and other features. Array synthesis is usually performed by permanently or adaptively weighting the signals of the array elements with gains and phases. Some researchers proposed array synthesis using geometrical redistribution of antenna array elements. In [40], [41] and [42], null steering was performed by altering the relative positions of the antenna array elements during operation. Nevertheless, this is a very tough action to do for an antenna array. Most research is concentrated in fixed and adaptive antenna array weighting for array synthesis.

In order to estimate the radiated power of an array antenna in the far-field region, one needs to understand the radiated field intensity of an element in the far-field region. The element pattern is defined as the field intensity distribution of a radiating element as a function of two far-field coordinates, while the radial distance remains constant. In a spherical coordinate system the radiated electric field in the far-field location can be expressed as

$$\vec{E}(r,\theta,\varphi) = A\frac{e^{(-jk_0r)}}{r}\vec{e}(\theta,\varphi) \tag{2.1}$$

In the above, A is a constant which is related to the input excitation of the antenna, $\vec{e}(\theta,\varphi)$ is the element pattern, (r,θ,φ) is the spherical coordinates of the far-field point, also known as the observation point, and k_0 is the wave number in free space. In (2.1, $\vec{e}(\theta,\varphi)$ is a complex vector function having components along $\hat{\theta}$ and $\hat{\varphi}$ directions only. The radial component does not exist in the far-field region. The complex directive pattern of an element is the far-field intensity pattern normalized with respect to the square root of the average radiated power per unit solid angle. The total radiated power is determined by integrating the Poynting vector on a spherical surface covering the antenna element as

$$P_r = \frac{|A|^2}{\eta}\int_0^{2\pi}\int_0^{\pi}|\vec{e}(\theta,\varphi)|^2 sin\theta d\theta d\varphi \tag{2.2}$$

In (2.2, represents free-space impedance, which is equal to 120π ohms. The average power per unit solid angle is

$$P_r^{av} = \frac{P_r}{4\pi} \tag{2.3}$$

Thus the complex directive pattern of the element becomes

$$\vec{D}(\theta,\varphi) = \sqrt{\frac{1}{\eta}}\sqrt{\frac{4\pi}{P_r}}\vec{e}(\theta,\varphi) \tag{2.4}$$

Substituting (2.2 in (2.4, we obtain

$$\vec{D}(\theta,\varphi)=\frac{\sqrt{4\pi}\vec{e}(\theta,\varphi)}{\sqrt{\int_0^{2\pi}\int_0^{\pi}|\vec{e}(\theta,\varphi)|^2 sin\theta d\theta d\varphi}} \tag{2.5}$$

The directivity of an element signifies the relative power flux per solid angle with respect to that of an isotropic radiator that radiates an equal amount of power. The directivity is the square of the magnitude of $\vec{D}(\theta,\varphi)$. Usually the directivity is expressed in dBi, where i stands for isotropic. The complex gain pattern of an element is the far-field intensity pattern normalized with respect to the incident power at the antenna input instead of the total radiated power. Thus the complex gain pattern with respect to the field intensity can be expressed as

$$\vec{G}(\theta,\varphi)=A\sqrt{\frac{4\pi}{\eta P_{inc}}}\vec{e}(\theta,\varphi) \tag{2.6}$$

In (2.56, P_{inc} is the incident power and A is related to P_{inc}. Since the total radiated power is reduced by the antenna mismatch loss and other radio-frequency (RF) losses, the gain does not exceed the directivity.

The radiated field of an array is the summation of the individual element fields. The far-field pattern of an array of identical elements can be represented by a product of two quantities, namely the *element pattern* and the *array factor*. The element pattern signifies the radiation behavior of an individual element and the array factor signifies the arraying effect, including array architecture and relative excitations of the elements. To establish this relation we consider a linear array of N identical elements along the x-axis with element spacing a as shown in Figure 2.1.

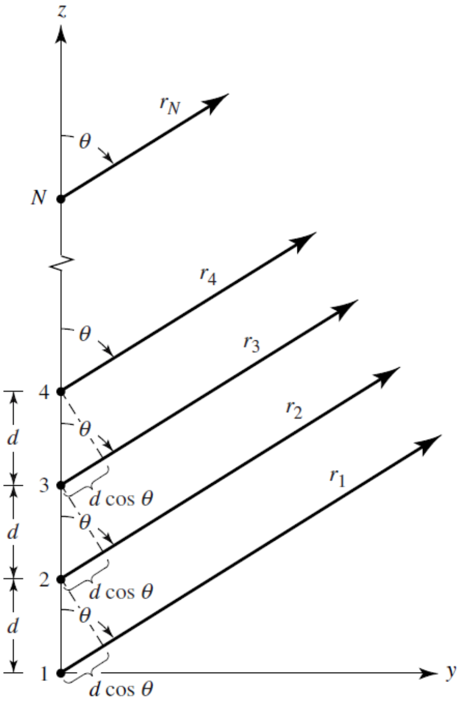

Figure 2.1-Linear Array of N elements

The excitation coefficient *A_n(n = 1,2, ..., N)* is assumed to be a complex number incorporating amplitude and phase in a single entity. Invoking (2.1 and applying superposition of the individual fields, the array field can be expressed as

$$\vec{E}_{array} = A_1 \frac{e^{(-jk_0 r_1)}}{r_1} \vec{e}(\theta,\varphi) + A_2 \frac{e^{(-jk_0 r_2)}}{r_2} \vec{e}(\theta,\varphi) + \cdots + A_N \frac{e^{(-jk_0 r_N)}}{r_N} \vec{e}(\theta,\varphi) \quad (2.7)$$

r_n(n = 1, 2, …, N) is the distance from the nth element to the observation point located at the far field. For r_n >> N×d we can have the following approximation

$$r_n \approx r_1 - (n-1)asin\theta cos\varphi \quad \text{n = 1, 2, …, N} \quad (2.8)$$

And $\frac{1}{r_n} \approx \frac{1}{r_1}$ then

$$\vec{E}_{array} = \frac{e^{(-jk_0r_1)}}{r_1}\vec{e}(\theta,\varphi)[\boldsymbol{A_1} + \boldsymbol{A_2e^{(jk_0asin\theta cos\varphi)}} + \cdots \\ + \boldsymbol{A_Ne^{(jk_0(N-1)asin\theta cos\varphi)}}] \tag{2.9}$$

The quantity in bold is known as the array factor (AF) for a linear array. Ignoring the radial dependence part we observe that the array pattern reduces to a product of the element pattern and the array factor.

The gain of an array can be determined after normalizing the field intensity in (2.9 with respect to the total incident power of the array. It is convenient to use the element gain pattern as the element pattern in (2.9 because the field intensity is already normalized with respect to its incident power. The array pattern thus can be written as

$$\vec{E}_{array} = \vec{G}(\theta,\varphi)[\boldsymbol{A_1} + \boldsymbol{A_2e^{(jk_0asin\theta cos\varphi)}} + \cdots + \boldsymbol{A_Ne^{(jk_0(N-1)asin\theta cos\varphi)}}] \tag{2.10}$$

The element gain pattern, $\vec{G}(\theta,\varphi)$, is normalized so that

$$\int_0^{2\pi}\int_0^{\pi}\left|\vec{G}(\theta,\varphi)\right|^2 sin\theta d\theta d\varphi = 4\pi(1-L) \tag{2.11}$$

where L is the antenna loss factor. We must emphasize here that for the array gain determination we consider *An* as the normalized incident voltage or current for the nth element such that $|A_n)|^2$ becomes its incident power. Thus the total incident power of the array is given by

$$P_{inc} = \sum_{n=1}^{N}|A_n|^2 \tag{2.12}$$

Thus the complex gain pattern of the array can be written as

$$\vec{G}_{array}(\theta,\varphi) = \frac{\sum_{n=1}^{N} A_n\vec{G}_n(\theta,\varphi)e^{(jk_0asin\theta cos\varphi)}}{\sqrt{\sum_{n=1}^{N}|A_n|^2}} \tag{2.13}$$

$\vec{G}_n(\theta,\varphi)$ represents the active element gain pattern for the nth element of the array.

2.2 Array Synthesis

In sensor array weight synthesis, the main concern is to determine the excitations of a given array so as to produce a beam pattern that suitably approximates a desired pattern. The desired beam pattern can vary widely depending on the application. Among these applications, there is a major class of pattern synthesis that aims to achieve a high mainlobe to sidelobe ratio or high-array resolution. Array weights are calculated to achieve a certain desired array response. One typical example for the type of pattern synthesis method is the Dolph–Chebyshev method [43], which designs the array pattern with equi-sidelobe response using an uniformly spaced linear array.

From an implementation viewpoint, it is desirable to synthesize an array with the fewest assumptions made about the array characteristics, such as isotropic elements, so that the synthesized array excitation gives the true array pattern for a set of selected array sensors with certain responses or characteristics. Moreover, most of the synthesis methods are only tailored to a certain array geometry.

There are many different methods to synthesize amplitude weights that produce desirable sidelobe levels. In what follows, several approaches are described. In general, the analytical synthesis approaches require linear.

2.2.1 Binomial Weights

These amplitude weights are the binomial coefficients, hence this array is known as a binomial array. Table I lists the binomial coefficients for up to nine element arrays. The taper efficiency for binomial arrays is very low. The price paid for lowering sidelobe levels is a decrease in taper efficiency (Table I) and directivity and a corresponding wide main beam. Errors are always present in an array, so even though the amplitude taper results in no sidelobes, the array factor has error sidelobes. Consequently, other more efficient sidelobe tapers with sidelobe levels comparable to the error sidelobes are more desirable.

Table I- Binomial Amplitude weights for an Array[44]

Number of Elements	Amplitude Weights	Taper Efficiency
1	1	1
2	11	1
3	121	0.889
4	1331	0.8
5	14641	0.731

2.2.2 Dolph–Chebyshev Weights

Sidelobe levels can be set to a specified level by mapping the array factor to a Chebyshev polynomial [43]. The Chebyshev polynomials are represented by

$$F_m(x) = \begin{cases} \cos(m cos^{-1} x) & |x| \leq 1 \\ \cosh(m cosh^{-1} x) & x > 1 \\ (-1)^m \cosh(m cosh^{-1} |x|) & x < 1 \end{cases} \tag{2.14}$$

Chebyshev polynomial lies between zero and unity if |x| < 1 and exceeds unity if |x| > 1. This property of the polynomial is utilized to construct the array factor. Toward that end, the variable x is defined in such a way that |x| < 1corresponds to the side-lobe region of the array, while the bore sight corresponds to a point where |x| > 1. A Dolph–Chebyshev (D–C) array has symmetrical amplitude distribution. Consider the following array factor of a linear array with N elements of Element spacing *a*:

$$AF(\theta) = \sum_{-(N-1)/2}^{(N-1)/2} A_n e^{(jk_0 nasin\theta)} \tag{2.15}$$

Using symmetrical feeding, the array factor becomes

$$AF(\theta) = A_0 + 2 \sum_{-(N-1)/2}^{(N-1)/2} A_n cos(2ncos^{-1}x) = BF_{N-1}(cx) \tag{2.16}$$

B is a constant and c determines the sidelobe level (SLL).

The main beam location corresponds to x=1 and the side-lobe region corresponds to |cx|<1. In the region |cx| < 1, $F_{N-1}(cx)$ becomes a cosine function with real argument, implying that the side lobes have uniform peaks of magnitude B. Thus the SLL of the array, R, is given by

$$R = \left|\frac{BF_{N-1}(c)}{B}\right| F_{N-1}(c) \tag{2.17}$$

The excitation coefficients should be calculated. This can be done by expressing Chebyshev functions in (2.16 as polynomials of x and then comparing term by term [45].

The Chebyshev weighting is practical for a small linear array; but as N becomes large, the amplitude weights at the edge of the aperture increase. Increasing the edge taper presents problems with edge effects and mutual coupling.

To calculate the synthesis weights are given by [46]

Let

$$\mu_0 = cosh\left[\frac{1}{L-1} cosh^{-1}\left(10^{-SLL/20}\right)\right] \tag{2.18}$$

$$w_{\Gamma-n+1} = \sum_{p=n}^{\Gamma} (-1)^{\Gamma-p} \frac{\Gamma}{\Gamma+p} \binom{\Gamma+p}{2p} \binom{2p}{p-n} \mu_0^{2p} \qquad \text{for } n=0,\ 1,\ 2,\ \dots,\ \Gamma \tag{2.19}$$

2.2.3 Taylor Weights

Taylor taper is suited for large and small arrays [47]. This technique differs from Chebyshev synthesis in that the relation between beam width and sidelobe level is not optimum. In this case, only a specific number of close-in sidelobes are of constant level but for the rest of the sidelobes, the heights decrease away from the broadside of the array. Though the Taylor pattern is different from the Chebyshev pattern, the beam width–sidelobe relationship of Taylor pattern is generally quite close to optimum. Moreover, the array weights for the end elements usually do not increase as much as compared with those of Chebyshev arrays. As a result, Taylor synthesis is of considerable practical interest.

The array weights are synthesized using the aperture sampling method.

Consider a linear array of L-element and let *N=L-1*.

$$w_i = \frac{1}{L}\left\{1 + 2\sum_{-(N-1)/2}^{(N-1)/2} f(n,A,\bar{n})A_n cos(\frac{2\pi n z_i}{L})\right\} \tag{2.20}$$

where $\bar{n}$ is the number used to decide the number of close-in sidelobes to be set with a constant sidelobe level. In practice, $\bar{n}$ is usually set in the range of 2 to 6. Other parts of the preceding expression are defined as

$$z_i = i - \left(\frac{N}{2} + 1\right) \tag{2.21}$$

$$f(n,A,\bar{n}) = \begin{cases} \dfrac{[(\bar{n}-1)!]^2}{(\bar{n}-1+n)!\,(\bar{n}-1-n)!}\displaystyle\prod_{m=1}^{\bar{n}-1}\left[1-\left(\frac{n}{u_m}\right)^2\right] & |n| < \bar{n} \\ 0 & |n| \geq \bar{n} \end{cases} \tag{2.22}$$

$$u_m = \begin{cases} \pm a\sqrt{A^2 + \left(m - \frac{1}{2}\right)^2} & 1 \le m < \bar{n} \\ \pm m & \bar{n} \le m < \infty \end{cases} \tag{2.23}$$

$$a = \frac{\bar{n}}{\sqrt{A^2 + \left(\bar{n} - \frac{1}{2}\right)^2}} \tag{2.24}$$

$$A = \frac{1}{\pi} cosh^{-1} R \tag{2.25}$$

$$R = 10^{SLL/20} \tag{2.26}$$

The beam width of the Taylor array in degree is approximated as

$$\theta_{Taylor} = 2sin^{-1}\left\{\frac{a}{L\pi}\sqrt{(cosh^{-1}R)^2 - \left(cosh^{-1}\frac{R}{\sqrt{2}}\right)^2}\right\} \tag{2.27}$$

2.3 Analog Beamforming

Beamforming, or radiation pattern synthesis, is realized by using antenna arrays with multiple antenna elements having control over the signal coming to each of the. The beam steering to a certain angle θ away from the centre can be achieved by delaying the signal to individual elements in such a manner that they add constructively in the intended direction θ. Let's assume the signal in the nth element is delayed by (n-1)τ. with antenna element spacing d, the signal transmitted by all the elements would have different delays among them. The free space delay between any nth antenna element signal and the last antenna element (Nth) signal is given as

$$t_n = \frac{(N-n)dsin\theta}{c} = (N-n)t_0 \qquad (2.28)$$

$$t_0 = \frac{dsin\theta}{c} \qquad (2.29)$$

The electric field vector (E) from a nth antenna at the wavefront is

$$E_n = e^{jw_0[t-t_n-(n-1)\tau]} \qquad (2.30)$$

$$E_n = e^{jw_0[t-(N-n)t_0]}e^{jw_0(n-1)\tau]} \qquad (2.31)$$

Summing the E-field vector for all the N antenna elements, we have

$$E_{array} = \sum_{n=1}^{N} E_n \qquad (2.32)$$

$$E_{array} = e^{jw_0[t-(N-1)t_0]} \sum_{n=1}^{N} e^{jw_0[n(t_0-\tau)]} \qquad (2.33)$$

$$E_{array} = e^{jw_0[t-(N-1)t_0]}e^{jw_0\frac{(N-1)(t_0-\tau)}{2}} \frac{\sin[\frac{1}{2}Nw_0(t_0-\tau)]}{\sin[\frac{1}{2}w_0(t_0-\tau)]} \qquad (2.34)$$

Therefore the magnitude of the summed E-field vector is

$$\left|E_{array}\right| = \left|\frac{\sin[\frac{1}{2}Nw_0(t_0-\tau)]}{\sin[\frac{1}{2}w_0(t_0-\tau)]}\right| \qquad (2.35)$$

The magnitude of the summed E-filed can be maximized for an angle μ by setting t=t0,

$$\tau_{opt} = t_0 = \frac{dsin\theta}{c} \tag{2.36}$$

Using this condition, the E-field obtained via summing is N times larger than the E-field of a single antenna element. Since power is proportional to the square of electric field, therefore the radiation intensity of an antenna array would be N^2 times greater than of single antenna. This also implies that the Effective Isotropic Radiated Power (EIRP) of an antenna array is N^2 times greater than of single antenna. The E-field for spatial angle θ using a fixed delay τ is given as

$$|E_{array}| = \left| \frac{\sin[\frac{1}{2} N w_0 \left(\frac{dsin\theta}{c} - \tau\right)]}{\sin[\frac{1}{2} w_0 \left(\frac{dsin\theta}{c} - \tau\right)]} \right| \tag{2.37}$$

The maximum directivity of an N-element is given as

$$D_{array,max} = \frac{U_{max}}{U_0} = \frac{E_{max}^2}{E_0^2} = \frac{\frac{1}{N} N^2}{1} = N \tag{2.38}$$

The programmable time delays at RF frequencies are relatively difficult to implement in a compact form [63]. In addition to that, for narrow band signal; time delays can be approximated by phase shifts. Therefore, the beamforming and steering is achieved by using N element phased array antenna as shown in Figure 2.1.

The signal in applied to each element in phased array antenna are progressively phase shifted. The signal to n^{th} element in an array has a phase shift of $(n-1)\varphi$. The magnitude of the E-field vector for an array is given as

$$|E_{array}| = \left| \frac{\sin[\frac{1}{2} N \left(w_0 \frac{dsin\theta}{c} - \varphi\right)]}{\sin[\frac{1}{2} \left(w_0 \frac{dsin\theta}{c} - \varphi\right)]} \right| \tag{2.39}$$

The antenna radiation pattern is also effected by the inter-element spacing of the antenna array “d”. When the spacing exceeds by half wavelength, multiple radiation lobe with similar magnitude as of main lobe appears in the radiation pattern. These un-intended radiation lobes are called as grating lobes. These grating lobes are undesired as the transmitted energy in unwanted direction which results in loss of signal but also it can cause interference signal of another users.

In analog beamforming, the weights, amplitude and phase, are applied to the signal in the RF domain. The architecture of a generic analog beamformer, in reception, is shown in Figure 2.2. Each one of the N received signals passes through a low noise amplifier, automatic gain controller and RF filter.

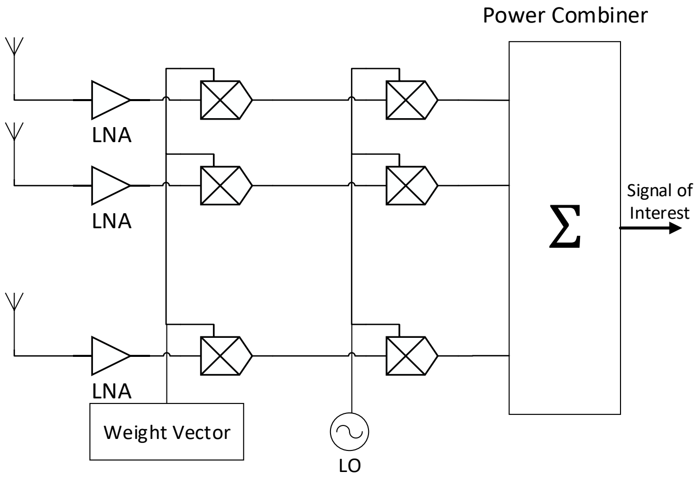

Figure 2.2-Analog Beamformer Architecture

Signal weighting is performed through various methods in analog beamforming. Phase shifting the signals in the RF domain would steer the radiation pattern toward a scan angle of interest. Let's assume phase shift between mth antenna element and nth phase shifter as φ_{mn}, where m=1, . . ., M and n=1,.. . . N. To direct the beam at angle θ_n which is off broad side for wavelength of λ_0, the required phase shift for the corresponding elements would be

$$\varphi_{\mathrm{nm}} - \varphi_{\mathrm{n(m-1)}} = \frac{2\pi d sin\theta_n}{\lambda_0} \qquad \mathrm{m}=2, \ldots, \mathrm{M} \qquad (2.40)$$

As the inter-element spacing "d" increases, the beam gets narrower at the cost of scanning range. Because as the inter-element distance increases, the grating lobe appears in the radiation patterns which limits the scanning range. In order to avoid the grating lobes, the inter-element distance “d” must satisfy the following inequality

$$\frac{\lambda_0}{d} > 1 + \max|sin\theta_n| \qquad n=1, \ldots, N \tag{2.41}$$

Amplitude weights are applied using RF adjustable attenuators. All the received signals after the AGC stage will have the same amplitude. The amplitude weights are relative, i.e. the amplitude ratio between different signals is what really matters, so the outputs of the AGCs are passed through adjustable attenuators. The attenuation ratio is equivalent to the amplitude weight[48][49][50].

Analog beamforming is advantageous among digital beamforming in many points. Exploiting analog beamformers would definitely reduce the number of needed local oscillators and ADCs to 1 instead of N[51]. In addition, the power consumption of all analog beamformer is less than digital beamformer as the additional digital circuits require more power.

2.4 Digital Beamforming and DOA estimation

Analog Beamforming is advantageous in many aspects. Nevertheless, digital beamforming might be better especially in massive MIMO and for high antenna array element number. Implementing beamforming on the baseband digital signal will make it possible to make use of most complex beamforming adaptive tracking algorithms. In addition, implementation cost will be much lower as no expensive microwave adjustable phase shifters and attenuators are needed. Instead, beamforming on all signals is done in a single baseband processor. Another advantage is that the digital receiver and digital beamformer could be realized on the same chip and hence decrease the parasitic effects and phase/amplitude uncertainties that might exist in these systems[52][53][54]. It is worth mentioning also that even if the system is a wideband system, narrowband beamforming algorithms could be implemented in the baseband as the phase change will be exported to the RF domain for all frequencies of operation.

The architecture of a digital beamformer is shown in Figure 2.3. Each antenna element is connected to a receiver chain. The frequency downconverted signal is digitized using ADC and the baseband digital signals are weighted inside the baseband processor.

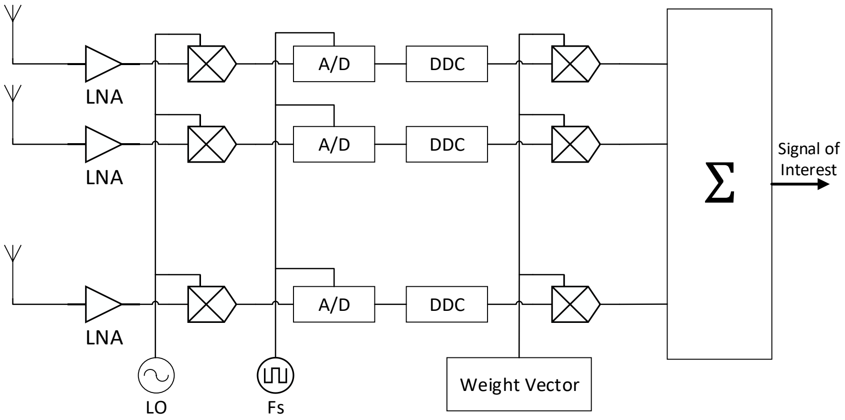

Figure 2.3-Digital Beamformer Architecture

The received RF signal from linear array is filtered, amplified and down converted and then transferred into digital domain through an ADC. The signal can be represented as

$$\mathrm{x_m} = \mathrm{x_1}, \mathrm{x_2}, \ldots, \mathrm{x_M} \qquad m = 1, 2, \ldots, M \tag{2.42}$$

Where $\mathrm{x_M}$ is the complex baseband signal from the mth antenna element. This signal contains both the I and Q components. A weighting vector in the digital domain can be applied to the received baseband samples defined as

$$\mathrm{w_m} = \mathrm{w_1}, \mathrm{w_2}, \ldots, \mathrm{w_M} \qquad m = 1, 2, \ldots, M \tag{2.43}$$

Where $\mathrm{w_m} = \mathrm{a_m} e^{j\varphi_m}$ is the complex weight for the nth beam coming from mth element. The coefficient a_m controls the amplitude tapering and φ_m determines the phase delay for each antenna element. These values can be changed with respect to different frequencies. The beamformed signal is then

$$\mathrm{y(\theta)} = w^H \mathrm{x} \tag{2.44}$$

Where H denotes the Hermitian transpose of the weighting matrix.

Beamforming is performed by multiplying the baseband digital signal with the convenient weights. In the case of transmission, the baseband digital data are weighted then converted to analog and modulated on a high frequency carrier. In the case of reception, the received signal is frequency down converted, converted to digital and then weighted with the convenient weights.

2.4.1 Beamforming Algorithms

Adaptive arrays provide significant advantages over conventional arrays in both communication and radar systems. They have well-known advantages for providing flexible, rapidly configurable, beamforming and null-steering patterns. However, this is often assumed because of its flexibility in using the available array elements in an adaptive mode and, thus, can overcome most, if not all, of the deficiencies in the design of the basic or conventional arrays [55]. Therefore, conventional goals, such as low sidelobes and narrow beamwidth in the array design can be ignored in the implementation of an adaptive array.

An adaptive antenna array is the one that continuously adjusts its own pattern by means of feedback control [56]. The principal purpose of an adaptive array sensor system is to enhance the detection and reception of certain desired signals. The pattern of the array can be steered toward a desired direction space by applying phase weighting across the array and can be shaped by amplitude and phase weighting the outputs of the array elements [57]. Additionally, adaptive arrays sense the interference sources from the environment and suppress them automatically. Several beamforming algorithms had been developed to make it possible to synthesize adaptive beams especially in the digital domain.

2.4.1.1 Conventional beamformer

A conventional beam former is a simple beam former with all its weights of equal magnitudes. The phases are selected to steer the array in a particular direction θ_0, known as the look direction. With denoting the steering vector S_0 in the look direction, the array weights are given by

$$w_c = \frac{1}{L} S_0 \tag{2.45}$$

The array with these weights has unity response in the look direction, that is, the mean output power of the processor due to a source in the look direction is the same as the source power. This may be understood as follows

Assume that there is a source of power p_s in the look direction, hereafter referred to as the signal source, with $m_s(t)$ denoting its modulating function. The signal induced on the l^{th} element due to this source only is given by

$$x_{ls}(t) = m_s(t)e^{j2\pi f_0(t+\tau_l)} \tag{2.46}$$

Thus, in vector notation, using a steering vector to denote relevant phases, the array signal vector due to the look direction signal becomes

$$x_s(t) = m_s(t)e^{j2\pi f_0(t)} s_0 \tag{2.47}$$

And the output of the array with weight vector w_c becomes

$$y_s(t) = w_s^H x_s(t) = m_s(t)e^{j2\pi f_0(t)} \tag{2.48}$$

Yielding the mean output power of the processor

$$p(w_c) = E[y(t)y^*(t)] \tag{2.49}$$

$$= p_s$$

Thus, the mean output power of the conventional beam former steered in the look direction is equal to the power of the source in the look direction. The process is similar to steering the array mechanically in the look direction except that it is done electronically by adjusting the phases.

2.4.1.2 Null Steering beamformer

A null-steering beam former is used to cancel a plane wave arriving from a known direction and thus produces a null in the response pattern in the DOA of the plane wave. One of the earliest schemes, referred to as DICANNE [58], achieves this by estimating the signal arriving from a known direction by steering a conventional beam in the direction of the source and then subtracting the output of this from each element. An estimate of the signal is made by delay-and-sum beam forming using shift registers to provide the required delay at each element such that the signal arriving from the beam-steering direction appears in phase after the delay. Then these waveforms are summed with equal weighting. This signal is then subtracted from each element after the delay. The process is very effective for cancelling strong interference and could be repeated for multiple interference cancellation. Though the process of subtracting the estimated interference using a delay-and-sum beam former used by DICANNE scheme is easy to implement for single interference, it becomes cumbersome as the number of interferences grows. A beam with unity response in the desired direction and nulls in interference directions may be formed by estimating the weights of a beam former, shown in Fig. 2, using suitable constraints [59]. Assume that S_0 is the steering vector in the direction where unity response is required and that $S_1, S_2, \ldots, S_k$ are k steering vectors associated with k directions where nulls are required. The desired weight vector is the solution of following simultaneous equations:

$$w^H S_0 = 1 \tag{2.50}$$

$$w^H S_i = 0 \quad \text{i=1, 2, ..., k}$$

Using matrix notation, this becomes

$$w^H A = e_1^T \tag{2.51}$$

Where A is a matrix with its columns being the steering vectors associated with all directional sources, including the look direction and e_1 is a vector of all zeros except the first element, which is one.

Assuming that the inverse of A exists, which requires that all steering vectors are linearly independent [60], the solution for the weight vector is given by

$$w^H = e_1^T A^{-1} \tag{2.52}$$

In case the steering vectors are not linearly independent, A is not invertible, and its pseudo inverse can be used in its place.

2.4.1.3 LCMV Beamformer

Beam-space processing is a two stage scheme where the first stage takes the array signals as input and produces a set of multiple outputs, which are then weighted and combined to produce the array output[61]. These multiple outputs may be thought of as the output of multiple beams. The processing done at the first stage is by fixed weighting of the array signals and amounts to produce multiple beams steered in different directions. The weights applied to different beam outputs to produce the array outputs are optimized to meet a specific optimization criteria. In general, for an L-element array, a beam-space processor consists of a main beam steered in the signal direction and a set of not more than L-1 secondary beams. The weighted output of the secondary beams is subtracted from the main beam as shown in the block diagram in Figure 2.4. The weights are adjusted to produce an estimate of the interference present in the main beam. The subtraction process then removes this interference. The secondary beams, also known as auxiliary beams, are designed such that they do not contain the desired signal from the look direction to avoid the signal cancellation in the subtraction process. Beam-Space beamformers were studied in literature. An adaptive processor for nulling of jammers in a satellite communications environment is described in [62]. The problem of generating simultaneous multiple beams from planar phased arrays with generic periodicity is discussed in [63]. A single-user multi-beam concurrent transmission scheme for future millimetre wave networks with multiple reflected paths is proposed. Based on spatial spectrum reuse, the scheme is multiple-input multiple-output (MIMO) technique in beamspace[64].

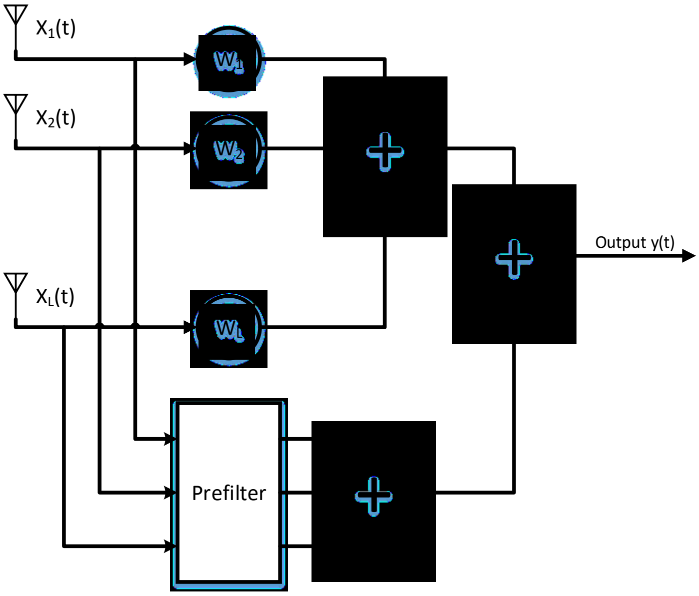

Figure 2.4-Beam-Space Beamforming Block Diagram

If a reference signal is not available, but we know the DOA angle of the signal of interest and their bandwidth range, then we can impose some constraints on the array coefficients and adaptively minimize the variance or power $E\{y(t) * y(t)\}$ of the beamformer output subject to the imposed constraints. This leads to the well-known, beam space based, linearly constrained minimum variance (LCMV) beamformer [65], where the response of the beamformer is constrained such that the desired signals impinging on the array from some specific directions are preserved subject to a specified gain and phase response, while the contributions in the beamformer output due to interfering signals arriving from other directions are minimized.

In order to ensure that any signal having a frequency ω_0 and DOA angle θ_0 passes the beamformer with a specified response G_0, where G_0 is a complex constant, we can set this constraint to:

$$w^H d(\theta_0, \omega_0) = G_0 \tag{2.53}$$

The value of the output power or variance is given by[65]:

$$E\{|y[n]|^2\} = w^H R_{xx} w \tag{2.54}$$

where R_{xx} is the observed array data's correlation matrix, and assumed to be positive definite and given in the form of:

$$R_{xx} = E\{x.x^H\} \tag{2.55}$$

The LCMV beamforming problem can be formulated as:

$$\arg\min_{w} w^H R_{xx} w \qquad \mathit{subject\ to} \qquad d^H(\theta_0, \omega_0)w = G_0^* \tag{2.56}$$

It is possible to have more than one linear constraint to enhance control of the beamformer[66]. The matricial form of the constraint imposed on w is:

$$C^H w = f \tag{2.57}$$

Where C is the constraint matrix and F is the response vector.

2.4.1.4 MVDR Beamformer

MVDR beamformer is also called optimal beamformer. Let an L-dimensional complex vector w represent the weights of the beam former, which maximizes the output SNR. For an array that is not constrained, an expression for w is given by[57][67]

$$w = \mu_0 R_N^{-1} S_0 \tag{2.58}$$

Where R_N is the array correlation matrix of the noise alone, that is, it does not contain any signal arriving from the look direction θ_0, and μ_0 is a constant. For an array constrained to have a unit response in the look direction, this constant becomes

$$\mu_0 = \frac{1}{S_0^H R_N^{-1} S_0} \tag{2.59}$$

Leading to the following expression for the weight vector:

$$w = \frac{R_N^{-1} S_0}{S_0^H R_N^{-1} S_0} \tag{2.60}$$

In practice, when the estimate of the noise-alone matrix is not available, the total R (signal plus noise) is used to estimate the weight. An expression for the weights for this case is given by

$$w = \frac{R^{-1} S_0}{S_0^H R^{-1} S_0} \tag{2.61}$$

These weights are the solution of the following optimization problem:

$$\min_{w} w^H R w \qquad \textit{subject to} \qquad w^H S_0 = 1 \tag{2.62}$$

2.4.2 DOA Estimation Algorithms

The problem of localization of sources radiating energy by observing their signal received at spatially separated sensors is of considerable importance, occurring in many fields, including radar, sonar and mobile communications.

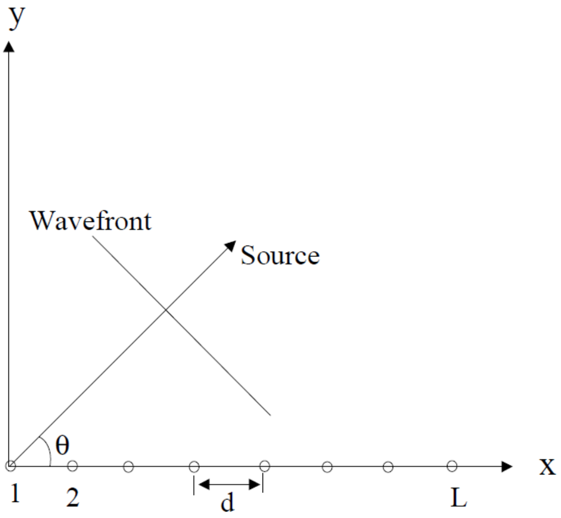

Figure 2.5- Signal Model Illustration

Assume that the array is located in the far field of directional sources. Thus, as far as the array is concerned, the directional signal incident on the array can be considered as a plane wave front. Also assume that the plane wave propagates in a homogeneous media. Thus, for the ideal case of nondispersive propagation and distortion free elements, the effect of propagation from a source to an element is a pure time delay. Let the origin of the coordinate system be taken as the time reference as shown in Figure 2.5. Thus, the time taken by a plane wave arriving from the kth source in direction θ_k and measured from the lth element to the origin is given by

$$\tau_l = \frac{r_l e^{j\theta}}{c} \tag{2.63}$$

$$\tau_l = \frac{d}{c}(l-1)cos\theta_k \tag{2.64}$$

The signal induced on the reference element (an element at the origin) due to the kth source is normally expressed in complex notation as

$$m_k(t)e^{j2\pi f_0 t} \tag{2.65}$$

With $m_k(t)$ denoting the complex modulating function and f_0 denoting the carrier frequency. The structure of the modulating function reflects the particular modulation used in a communication system.

Assuming that the wave front on the lth elements arrives $\tau_l(\theta)$ seconds before it arrives at the reference element, the signal induced on the l_{th} element due to the k_{th} source can be expressed as in (2.46).

$$m_k(t)e^{j2\pi f_0(t+\tau_l)} \tag{2.66}$$

Assume that there are M directional sources present. Let xl(t) denote the total signal induced due to all M directional sources and background noise on the lth element. Thus,

$$x_l(t) = \sum_{k=1}^{M} m_k(t)e^{j2\pi f_0(t+\tau_l)} + n_l(t) \tag{2.67}$$

Where *$n_l(t)$* is random noise component on the lth element, which includes background noise and electronic noise generated in the lth channel. It is assumed to be temporally white with zero mean and variance equal to σ_n^2.

Substituting from (2.67) in (2.64), the signal vector becomes

$$x(t) = \sum_{k=1}^{M} m_k(t) \begin{pmatrix} e^{j2\pi f_0 \tau_1} \\ e^{j2\pi f_0 \tau_2} \\ . \\ e^{j2\pi f_0 \tau_L} \end{pmatrix} e^{j2\pi f_0 t} + n(t) \tag{2.68}$$

Steering vector is an L-dimensional complex vector containing responses of all L elements of the array. Let S_k denote the steering vector associated with the k^{th} source. For an array of identical elements, it is defined as

$$S_k = \begin{pmatrix} e^{j2\pi f_0 \tau_1} \\ e^{j2\pi f_0 \tau_2} \\ . \\ e^{j2\pi f_0 \tau_L} \end{pmatrix} \tag{2.69}$$

For an array of identical elements, each component of this vector has unit magnitude. The phase of its i^{th} component is equal to the phase difference between signals induced on the i^{th} element and the reference element due to the source associated with the steering vector. As each component of this vector denotes the phase delay caused by the spatial position of the corresponding element of the array, this vector is also known as the space vector. It is also referred to as the array response vector as it measures the response of the array due to the source under consideration. In multipath situations such as in mobile communications, it also denotes the response of the array to all signals arising from the source[68].

Using (2.69) and (2.68)

$$x(t) = \sum_{k=1}^{M} m_k(t) S_k e^{j2\pi f_0 t} + n(t) \tag{2.70}$$

The array correlation matrix is

$$R = E[x(t)x^H(t)] \tag{2.71}$$

An expression of R is derived in terms of steering vectors by substituting the signal vector *x(t)* from (2.70) in the definition of the array correlation matrix given by (2.71) leads to the following expression for the array correlation matrix:

$$R = \sum_{k=1}^{M} p_k S_k S_k^H + \sigma_n^2 I \tag{2.72}$$

Where I is the identity matrix and $\sigma_n^2 I$ denotes the component of the array correlation matrix due to random noise and p_k denotes the power of the kth source measured at one of the elements of the array. The correlation matrix *R* may be expressed in the following compact form:

$$R = AMA^H + \sigma_n^2 I \tag{2.73}$$

Where columns of the L × M matrix A are made up of steering vectors, that is

$$A = [S_1, S_2, \dots, S_M] \tag{2.74}$$

And M × M matrix S denote the source correlation. For uncorrelated sources, it is a diagonal matrix with

$$M_{ij} = \begin{cases} p_i & i = j \\ 0 & i \neq j \end{cases} \tag{2.75}$$

2.4.2.1 Minimum Variance Distortionless Response (MVDR)

When there is more than one signal present, the array output power contains signal contributions from the desired angle as well as from the undesired angles. Capon's method [69] overcomes this problem by using the degrees of freedom to form a beam in the look direction and at the same time the nulls in other directions in order to reject other signals. In terms of the array output power, forming nulls in the directions from which other signals arrive can be accomplished by constraining a beam (or at least maintaining unity gain) in the look direction. Thus, for a particular look direction, Capon's method uses all but one of the degrees of the freedom to minimize the array output power while using the remaining degrees of freedom to constrain the gain in the look direction to be unity

$$minP(w) \qquad\qquad subject\ to \qquad\qquad w^H S(\theta) = 1 \tag{2.76}$$

The weight vector chosen in this way is often referred to as the minimum variance distortionless response (MVDR) beamformer, since, for a particular look direction, it minimizes the variance (average power) of the array output signal while passing the signal arriving from the look direction with no distortion. The resulting weight vector is shown to be given by

$$w = w_{cap} = \frac{R_{xx}^{-1} S(\theta)}{S^H(\theta) R_{xx}^{-1} S(\theta)} \tag{2.77}$$

The power spectrum is given by

$$P(\theta) = P_{cap} = \frac{1}{S^H(\theta) R_{xx}^{-1} S(\theta)} \tag{2.78}$$

2.4.2.2 MUSIC

Eigenstructure methods rely on the property of the array correlation matrix that the space spanned by its eigenvectors may be partitioned in two subspaces, namely the signal subspace and the noise subspace and the fact that the steering vectors corresponding to the directional sources are orthogonal to the noise subspace. As the noise subspace is orthogonal to the signal subspace, these steering vectors are contained in the signal subspace. In principle the eigenstructure based methods search for directions such that the steering vectors associated with these directions are orthogonal to the noise subspace and are contained in the signal subspace. In practice the search may be divided in two parts. First find a weight vector *w* which is contained the noise subspace or is orthogonal to signal subspace, and then search for directions such that the steering vector associated with these directions are orthogonal to this vector.

MUSIC (Multiple Signal Classification) is one of the earliest proposed and a very popular method for super-resolution direction finding [70]. In its standard form, also known as spectral MUSIC, the method estimates the noise subspace from available samples. This can be done either by eigenvalue decomposition of the estimated array correlation matrix or singular value decomposition of the data matrix with its N columns being the N array signal vector samples, also known as snapshots. The latter is preferred for numerical reasons. Once the noise subspace has been estimated, a search for M directions is made by looking for steering vectors that are as orthogonal to the noise subspace as possible. This is normally accomplished by searching for peaks in the MUSIC spectrum given by

$$P_{MU}(\theta) = \frac{1}{|S^H(\theta)U_N|^2} \tag{2.79}$$

where U_N denotes an L by L – M dimensional matrix, with L – M columns being the eigenvectors corresponding to the L – M smallest eigenvalues of the array correlation matrix and *S(θ)* denoting the steering vector that corresponds to direction *θ*.

It should be noted that instead of using the noise subspace and searching for directions with steering vectors orthogonal to this subspace, one could also use the signal subspace and search for directions with steering vectors contained in this space. This amounts to searching for peaks in

$$P_{MU}(\theta) = |U_S^H S(\theta)|^2 \tag{2.80}$$

Where U_S denotes an L × M dimensional matrix with its M columns being the eigenvectors corresponding to the M largest eigenvalues of the array correlation matrix.

It is advantageous to use the one with smaller dimensions. For the case of a single source, the DOA estimate made by the MUSIC method asymptotically approaches the Cramer–Rao lower bound, that is, where the number of snapshots increases infinitely, the best possible estimate is made. For multiple sources, the same holds for large SNR cases, that is, when the SNR approaches infinity. The Cramer–Rao lower bound (CRLB) gives the theoretical lowest value of the covariance for an unbiased estimator. In [71], an application of the MUSIC algorithm to cellular mobile communications was investigated to locate land mobiles, and it is shown that when multipath arrivals are grouped in clusters the algorithm is able to locate the mean of each cluster arriving at a mobile. This information then may be used to locate line of sight. Its use for mobile satellite communications has been suggested in [72].

2.4.2.3 Root-MUSIC

Root-MUSIC implies that the MUSIC algorithm is reduced to finding roots of a polynomial as opposed to merely plotting the pseudospectrum or searching for peaks in the pseudospectrum [73]. Barabell simplified the MUSIC algorithm for the case where the antenna is a ULA. The MUSIC pseudospectrum is given in (2.79). The objective is then to find the values of θ that are the poles of $P_{MU}(\theta)$ in (2.79) or the roots of $|S^H(\theta)U_N|^2$.

MUSIC pseudospectrum could be expressed as

$$P_{MU}(\theta) = \frac{1}{S^H(\theta)E_N E_N^H S(\theta)} \tag{2.81}$$

Let $C = E_N E_N^H$, the denominator of (2.86) could be written as $S^H(\theta)CS(\theta)$. Then the denominator is

$$\begin{aligned} S^H(\theta)CS(\theta) &= \sum_{m=0}^{M-1}\sum_{l=0}^{L-1} e^{-jkdmsin\theta} C_{mn} e^{jkdlsin\theta} \qquad (2.82) \\ &= \sum_{r=-L+1}^{L-1} C_r e^{jkdrsin\theta} \end{aligned}$$

where C_r is the sum of the elements along the r^th diagonal of C. Let $z = e^{-jkdsin\theta}$, then

$$D(z) = \sum_{r=-L+1}^{L-1} C_r z^r \tag{2.83}$$

The roots of D(z) that lie closest to the unit circle correspond to the poles of the MUSIC pseudospectrum. These 2(L − 1) roots can be written as

$$z_i = |z_i| e^{jarg(z_i)} \qquad \mathrm{i} = 1, 2, \dots, 2(\mathrm{L} - 1) \tag{2.84}$$

Choosing those roots inside the unit circle whose magnitude $z_i \approx 1$, and comparing $e^{jarg(z_i)}$ to $e^{-jkdsin\theta}$ gives

$$\theta_i = -sin^{-1}\left\{\frac{argz_i}{kd}\right\} \tag{2.85}$$

Obviously, when the root-MUSIC algorithm is implemented there is no prior knowledge of the incoming signal directions or signal powers needed to construct the correlation matrix using (2.79). Therefore the correlation matrix must be estimated using only the information available from the sensor array. There are several methods commonly used to perform this estimation such as temporal averaging, spatial smoothing or, a hybrid combination of both temporal averaging and spatial smoothing.

2.4.2.4 ESPRIT

The ESPRIT method for DOA estimation was first proposed by Roy and Kailath [74]. It is applicable to sensor arrays that consist of two identical and identically oriented subarrays, with one being a shifted “replica” of the other, where the displacement vector between the subarrays has to be known, whereas the geometry of each subarray may be unknown. The steering vectors for the two subarrays can be written as

$$\begin{aligned} S_1(\theta) &= J_1 S(\theta) \\ S_2(\theta) &= J_2 S(\theta) \end{aligned} \tag{2.86}$$

Where J$_1$ and J$_2$ are the selection matrices having in each row a single entry equal to one and all the others zero. Without any loss of generality, we assume that the two identical and identically oriented subarrays are displaced along the x-axis of the coordinate system. Then the steering vectors for the two subarrays are related as

$$S_1(\theta) = S_2(\theta)e^{j\frac{2\pi}{\lambda}d_x sin\theta} \tag{2.87}$$

Where d$_x$ now denotes the displacement between the two subarrays. Similarly, the two subarray steering matrices

$$A_1(\theta) = J_1 A(\theta) \tag{2.88}$$
$$A_2(\theta) = J_2 A(\theta)$$

are related as

$$A_1(\theta) = A_2(\theta)Q(\theta) \tag{2.89}$$

Where

$$Q(\theta) \triangleq diag\left\{e^{j\frac{2\pi}{\lambda}d_x sin\theta_1}, \dots, e^{j\frac{2\pi}{\lambda}d_x sin\theta_M}\right\} \tag{2.90}$$

Note that the signal DOAs can be obtained from the diagonal elements of *Q(θ)*.

The columns of E$_S$, The matrix of eigenvectors of signal correlation matrix, and A(θ) span the same subspace. Therefore,

$$E_s = A(\theta)T \tag{2.91}$$

Where T is non-singular. Then

$$E_{s1} = J_1 E_s = J_1 A(\theta)T = A_1(\theta)T = A_2(\theta)QT = E_{s2}T^{-1}QT \tag{2.92}$$

The matrices $T^{-1}QT\ and\ Q$ have the same eigenvalues. Therefore, the ESPRIT algorithm proceeds in two steps. First, an estimate of $T^{-1}QT$ is computed. Second, the signal DOAs are estimated from the eigenvalues of the $T^{-1}QT$.

Chapter 3 System Description

The system under discussion is a phased array based on digital beamforming. The classical phased array processing is conserved but rather performed for digital signals. The aim of this system is to provide a low cost solution for researchers to develop and test beamforming and DOA estimation algorithms for communication and radar. The system then should be capable of receiving RF signals and condition it. It should also down convert it to IF and digitize it. The digital data is postprocessed to provide desired radiation characteristics or to estimate its direction of arrival.

The proposed system should, in addition to what is stated before, have the capability to be calibrated for different uncertainties. The operation of the system is not application specific. It could be operated with the same configuration for both radar and communication application.

3.1 System Architecture

The System's block diagram is shown in Figure 3.1. It is composed mainly of three major blocks. Eight element linearly distributed antenna array, Software Defined Radio (SDR) boards for full RF to baseband conversion and an FPGA based baseband processor.

The antenna array is composed of eight wideband monopoles linearly distributed with uniform inter elements space. The antenna array should be flexible to handle more elements when needed. For that reason, antenna elements are split and mountable on the rigid reflector part. Its design should allow it to be mountable at base stations.

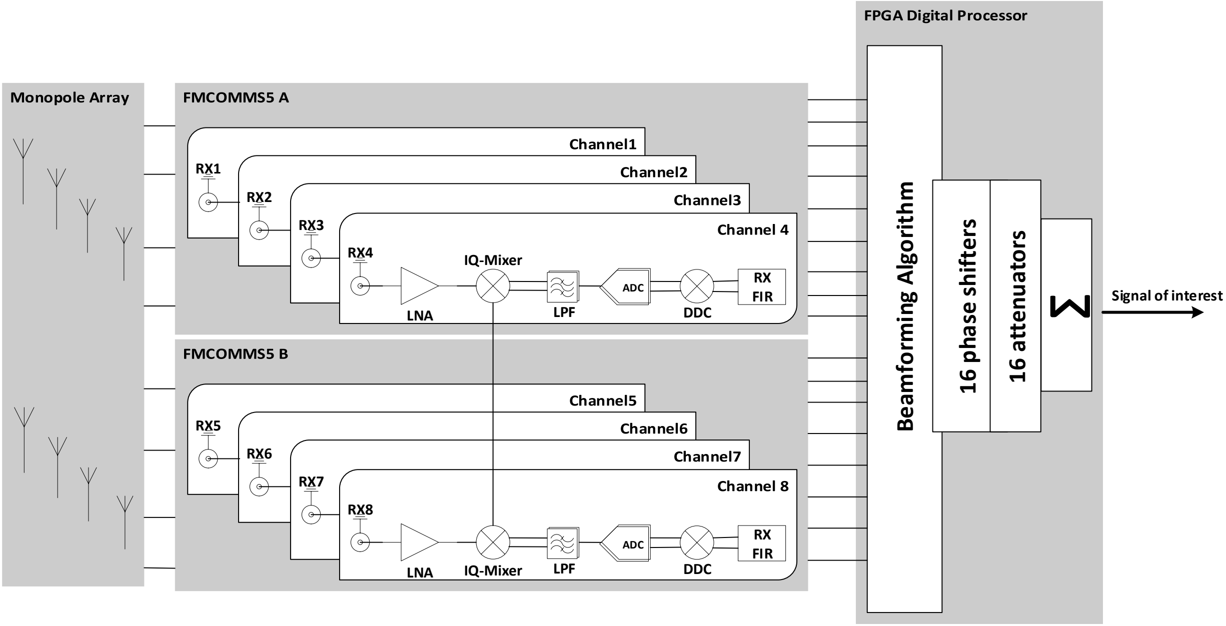

Figure 3.1-System Block Diagram

The second block of the system is the RF-Frontend with the SDR. The SDR is directly connected to the antenna array. It receives RF signals from the eight elements of the array, down converts them to intermediate frequency (IF), converts it to digital I/Q samples stream signal and directs it to the baseband processor. The SDS contains configurable circuitry to amplify and filter received signals. The third block in the testbed is the baseband processor or the FPGA. This block is responsible of controlling the SDR and performing baseband postprocesing on the received digital streams. The baseband processor applies complex weights to digital data in digital beamforming and estimates the direction of arrival of signals transmitted to the array wavefront.

This system is designed to be capable of evaluating various horizontal beamforming algorithms and testing their performance as well as examining the performance of new algorithms. For this purpose, eight chain receivers are used. Beamforming weights are calculated using a beamforming algorithm and applied to the digital baseband signals in the FPGA.

3.2 Broadband Monopole with Directional Pattern and Antenna Array

The testbed is designed to meet the requirements of LTE-A and the incoming 5G for sub 6GHz bands. To test the functionality and performance of the testbed, an antenna matched at mid and higher frequency bands of LTE-A in Europe is designed. The bands considered are from 1.7GHz to 1.9GHz and from 2.5GHz to 2.7GHz. Several attempts to design a dual band antenna with corresponding bandwidth, like fork fed double aperture microstrip patch antenna and wide slot antenna, were unsuccessful. A wide band antenna that covers all the required bands is then placed on track.

In this section, the design and simulation of a single monopole matched at the bands of interest is presented. The measurement results are also included. Also, an 8x1 antenna array based on the single monopole is designed, simulated and measured.

3.2.1 Single Element

The required antenna should be matched from 1.7GHz to 2.7GHz. This is about 46% of bandwidth and thus the antenna should be a Wide band antenna. A wide-band antenna should have reasonable radiation pattern over all the bands of operation.

Wire monopoles are classically the most widely used in wireless mobile communications. Quarter wavelength wire monopole antenna is commonly used for its broadband characteristics, low cost and ease of construction.

3.2.1.1 Antenna Structure

The design consists of a rectangular monopole with rounded corners as shown in Figure 3.2. The radius of the circular corners of the monopole is designated by R_{cor1}. The monopole is printed on a Rogers RO4003C substrate. A ground plane, the reference of the monopole, is printed on the opposite side of the substrate as shown in Figure 3.3.

The monopole is fed by a 50 ohms microstrip line. The feed line merges with the monopole through an elliptical transition with a major access along the terminal of the feed line and minor access along the side edge of the monopole. The minor radius of the ellipse is equal to L_{gap} and its major radius is $\frac{W_{mono}}{2}$.

In addition, the gap between the ground plane edge and the monopole edge, of length L_{gap}, create a slot effect. This effect plays a major role in increasing the bandwidth of the antenna and tuning the operation frequency range.

The length of the monopole, designated by L_{mono}, should be close to quarter wavelength the centre frequency of the operation frequency range. The wideband printed monopole is then a planar quarter wavelength monopole.

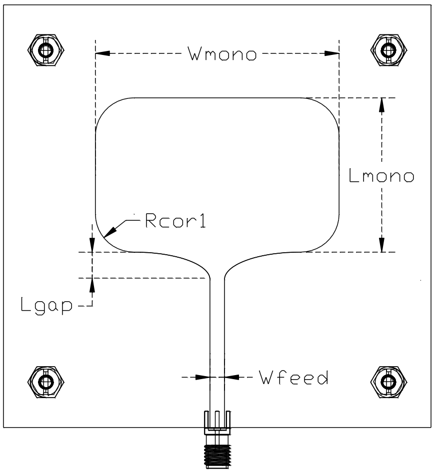

Figure 3.2-Monopole Top View with Dimensions Designators

The ground plane is a metallic copper plane printed on the other side of the substrate. The ground plane's upper edge is separated from the monopole's edge by a distance L_{gap}. Its corners are also made round with radius R_{cor2}. The ground plane is corrugated in the lower edge. Eleven consecutive grooves are formed. These grooves prevent current from returning through the coaxial feed line and eliminates the need for a Balun at the feed connector. The groove beneath the feedline is 7.5mm wide. This makes it difficult for currents circulating in the feedline from circulating back at the lower edge of the ground plane and hence prevent those currents from altering the radiation pattern.

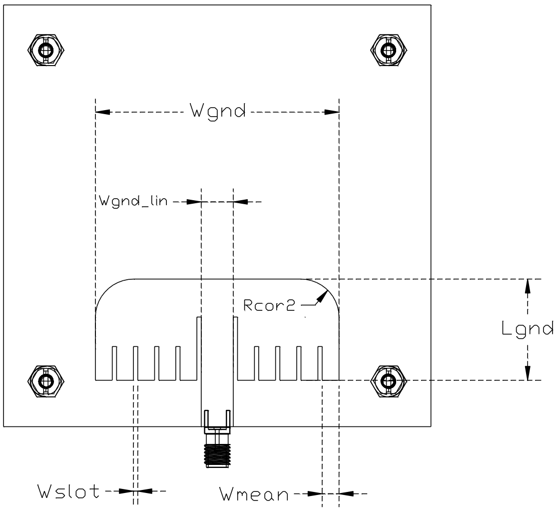

Figure 3.3-Monopole Bottom View with Dimensions Designators

Monopoles are omnidirectional in nature. They usually exhibit donut like radiation patterns. To make the radiation pattern directional, a ground plane is placed beneath the antenna as shown in Figure 3.4. The separation between the antenna and the reflector, H_{ref}, is made to be quarter wavelength of the lowest operating frequency. Nylon spacers are placed at the 4 corners of the substrate to insure separation is fixed and to not alter the radiation pattern of the antenna.

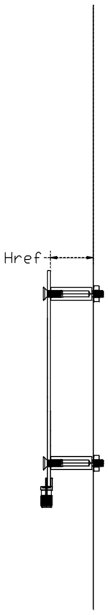

Figure 3.4-Monopole Side View with Reflector Height Designator

Besides the importance of the separation distance between the antenna and the reflector, another important dimension are the offsets from the edges of the antenna as shown in Figure 3.5. These offsets were increased to reduce the back-lobe level and to increase the front to back ratio.

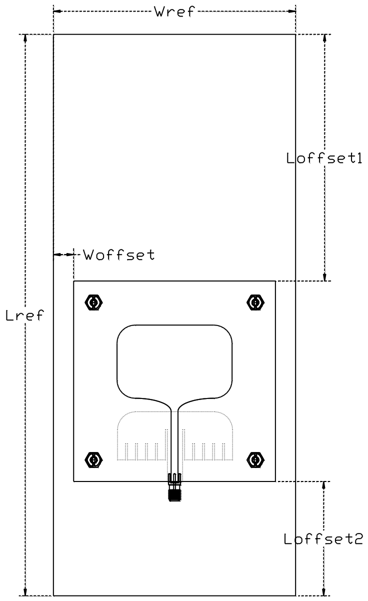

Figure 3.5-Monopole Top View with Reflector

The antenna was designed and simulated in CST microwave studio[75]. The dimensions were tuned to get the best radiation characteristics and convenient impedance matching over the band of interest. The final dimensions are listed in Table II. The antenna is then fabricated and assembled. The realised antenna is shown in Figure 3.6.

Table II- Antenna’s dimensions designators and values

Designator	W_{mono}	L_{mono}	R_{cor1}	R_{cor2}	L_{gap}	W_{gnd}	L_{gnd}	H_{ref}	$L_{offset1}$	$L_{offset2}$	L_{ref}
Value[mm]	57	36.5	9	9	6.5	57	24	44	123	57	280

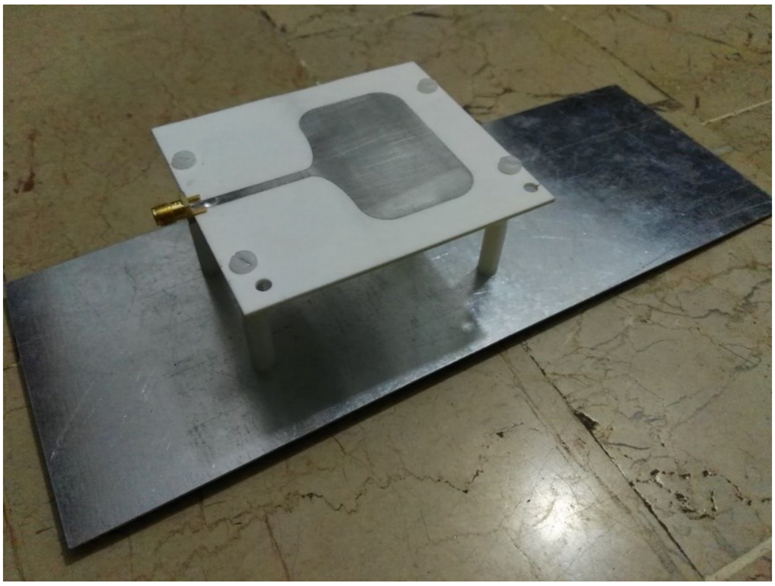

Figure 3.6- Monopole Photo with Reflector and Spacers

3.2.1.2 Antenna Simulation and Measurement

Before manufacturing, the monopole passed through simulation stages due to the big number of parameters that influence the characteristics of the antenna. In the simulation, several parameters are tuned to get the optimized performance. The parameter L_{mono} has a direct impact on the frequency of operation of the monopole. During simulations also, the radii of the elliptical transition and the radius of the round corners were tuned in order to get the widest impedance matching. The grooves in the ground plane in addition to the width of the central corrugation are optimized also to get the best radiation pattern. In addition, the separation between the reflector and the antenna was decided after several simulations with the goal being to increase the front to back ratio.

After simulation is finalized, the antenna is manufactured and assembled. The reflector is connected to the antenna by fixed length 44mm spacers.

3.2.1.2.1 Measurement Setup

The single monopole is measured for impedance characteristics and for radiation characteristics. After assembly of the single element, reflection coefficient is measured using N5227A PNA from Keysight. Before performing the measurement, the network analyser is calibrated with mechanical calibration kit. Measurement was done from 1GHz to 3GHz.

The radiation characteristics are measured in the anechoic chamber. The chamber's walls are covered with absorbing materials to prevent the reflected back signals from interfering with the received ones and, hence distorting the measurements. The antenna is fixed to an azimuth elevation rotating motor. On the other side of the room there is an UWB Vivaldi antenna as shown in Figure 3.7. This antenna is connected to the transmitter through a coaxial cable. A computer outside the chamber then controls the transmission, reception and rotation of the antenna under test. After finishing, the data is postprocessed using Matlab.

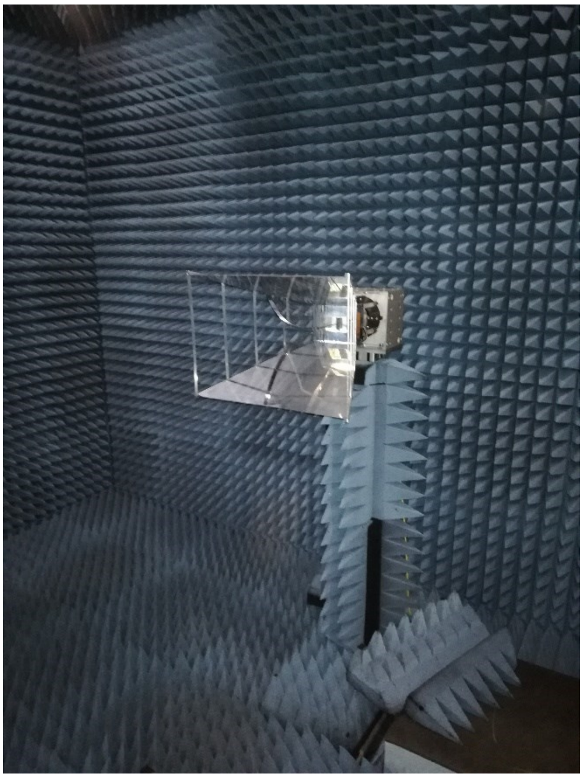

Figure 3.7-Ultra Wideband Vivaldi Antenna

3.2.1.2.2 Measurement Results

The reflection coefficient measurement of the single monopole is shown in Figure 3.8. The results of the antenna simulation showed impedance matching with S_{11} value less than -10dB between 1.75GHz and 2.85GHz. After measuring the reflection coefficient using the network analyser, impedance matching was found to be between 1.6GHz and 2.7GHz.

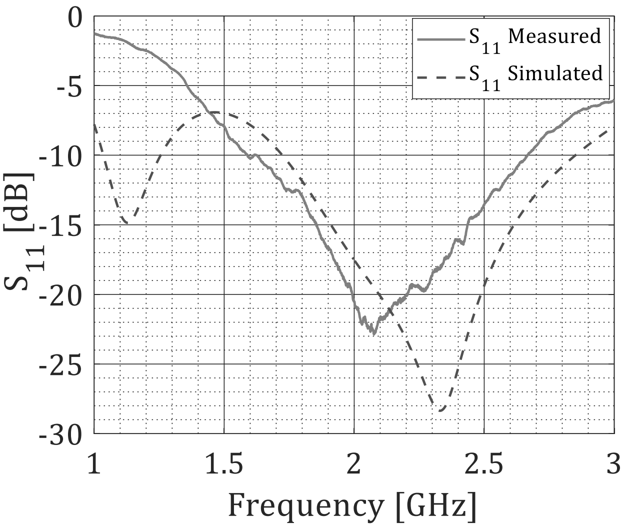

Figure 3.8-S_{11} of the single monopole

The 3-D radiation patterns evaluated through simulation and through measurements are presented in Figure 3.9 and Figure 3.10. Simulated gain radiation patterns at frequencies 1.7GHz, 1.8GHz and 1.9GHz are shown in Figure 3.9 a-1, b1 and c-1 respectively. The measured gain radiation patterns at 1.7GHz, 1.8GHz and 1.9GHz are shown in Figure 3.9 a-2, b2 and c-2 respectively.

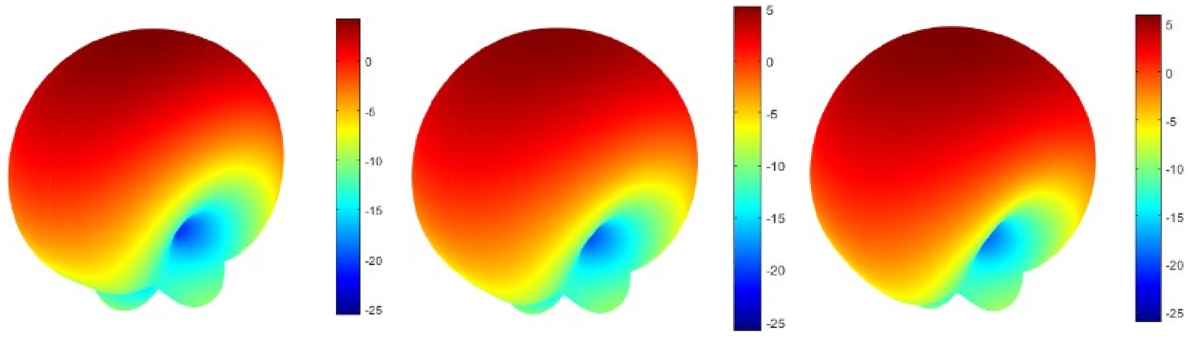

(a-1) (b-1) (c-1)

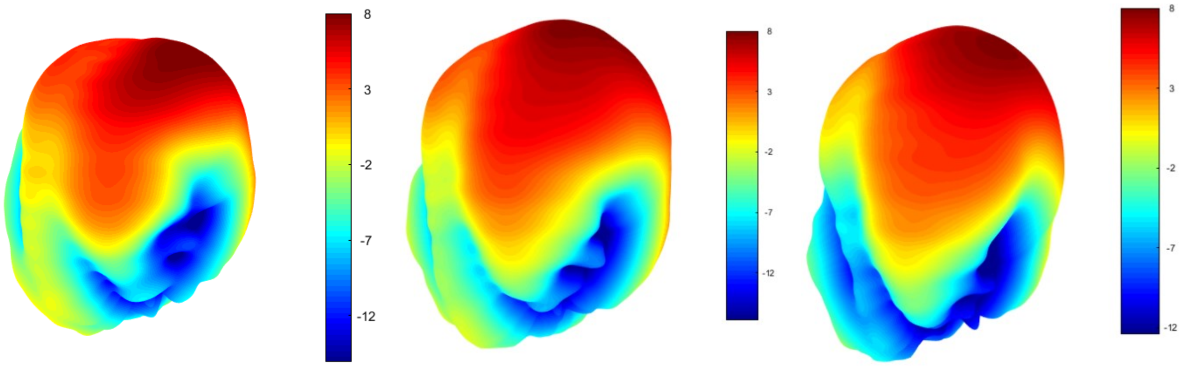

(a-2) (b-2) (c-2)

Figure 3.9- Simulated and measured 3-D radiation pattern of the single monopole at 1.7GHz, 1.8GHz and 1.9GHz

The gain radiation patterns were evaluated also at 2.5GHz, 2.6 GHz and 2.7GHz and the results are presented in Figure 3.10. The simulated gain radiation patters are labelled with index 1 and those corresponding for measurements are labelled with index 2.

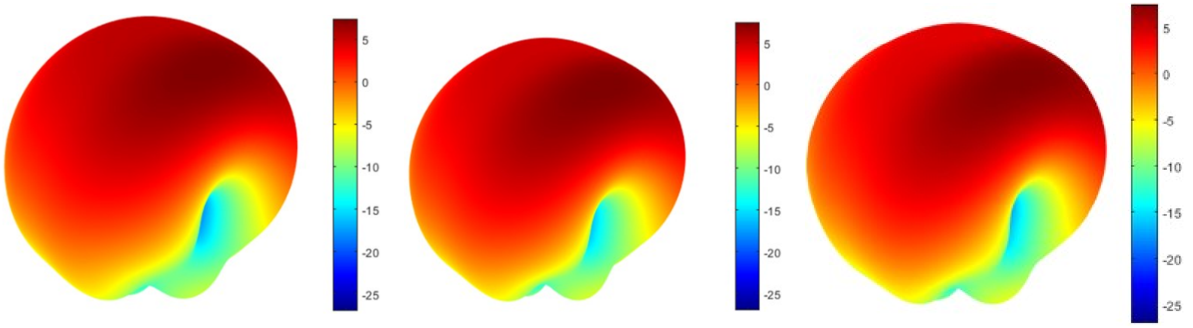

(a-1) (b-1) (c-1)

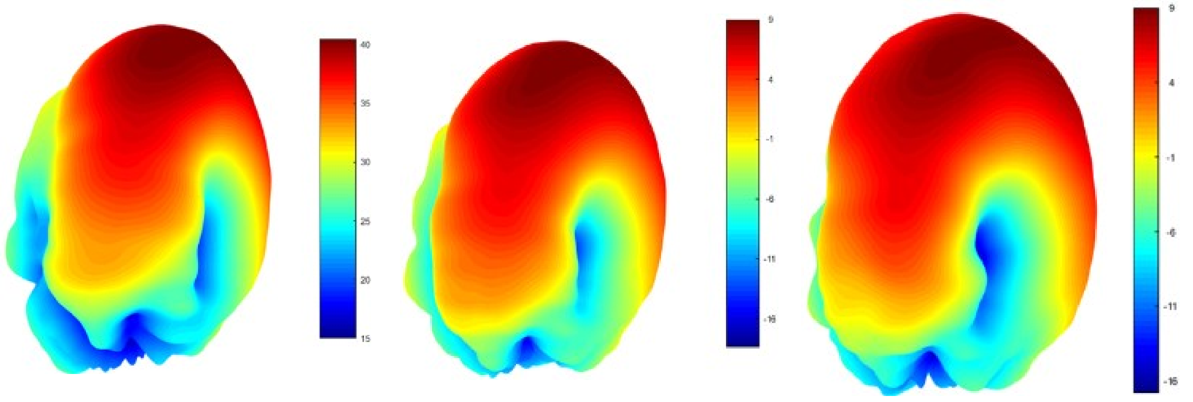

(a-2) (b-2) (c-2)

Figure 3.10- Simulated and measured 3-D radiation pattern of the single monopole at 2.5GHz, 2.6GHz and 2.7GHz

After analysing of the 3-D radiation patterns, the results for the higher frequencies seems very close to those of the simulated ones. Nevertheless, there seems to be a distortion in the radiation patterns at the lower frequencies. The radiation patterns seem to be tilted slightly from the broadside. One possible cause might be the insufficient separation between the reflector and the antenna.

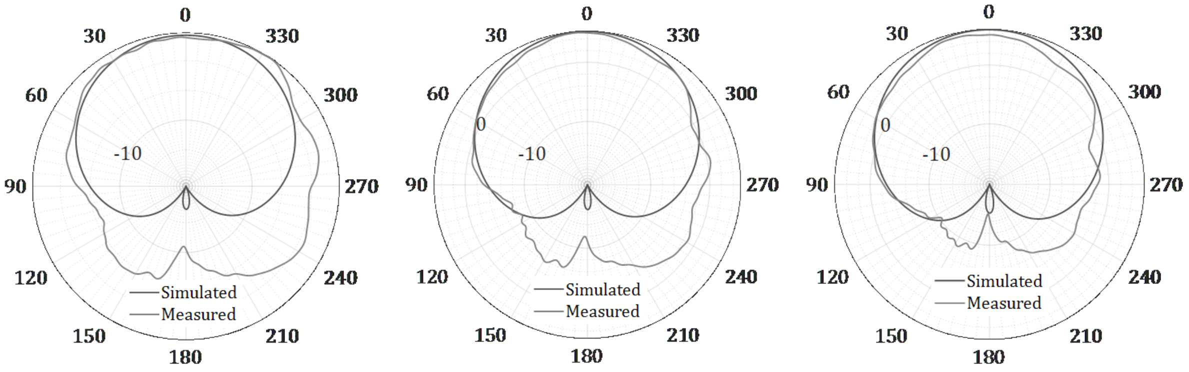

(a) (b) (c)

Figure 3.11- H-plane radiation pattern of the single monopole at 1.7GHz, 1.8GHz and 1.9GHz respectively

H-plane radiation patterns are shown in Figure 3.11 and in Figure 3.12.The simulated and measured radiation patterns at 1.7GHz, 1.8GHz and 1.9GHz are shown in Figure 3.11 a, b and c respectively while those at 2.5GHz, 2.6GHz and 2.7GHz are shown in Figure 3.12 a, b and c respectively. The plots for the measured radiation patterns at 2.5GHz and above are compliant with the simulation results. Measured radiation patterns for lower frequencies show a distortion especially at 1.7GHz and less at 1.8GHz and 1.9GHz. Despite the corruption noticed in the radiation patterns of the lower frequencies, the results are considered acceptable.

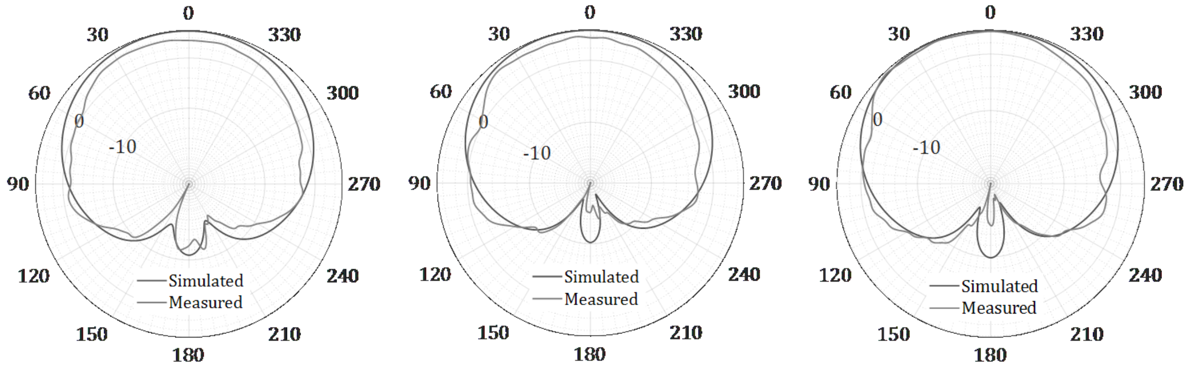

(a) (b) (c)

Figure 3.12- H-plane radiation pattern of the single monopole at 2.5GHz, 2.6GHz and 2.7GHz respectively

3.2.2 Eight-Element Antenna Array

In addition to enhancing the directivity of the antenna, an antenna array combined with beamforming will provide interference cancelling in addition to multibeam formation. An 8x1 linear array is designed based on the single monopole described in 3.2.1.The sketch of the array's top view is shown in Figure 3.13. In this testbed, the antenna array elements outputs should be weighted in the baseband. Hence, no feeding network is designed or provided in the array and each element has a unique port through an SMA connector.

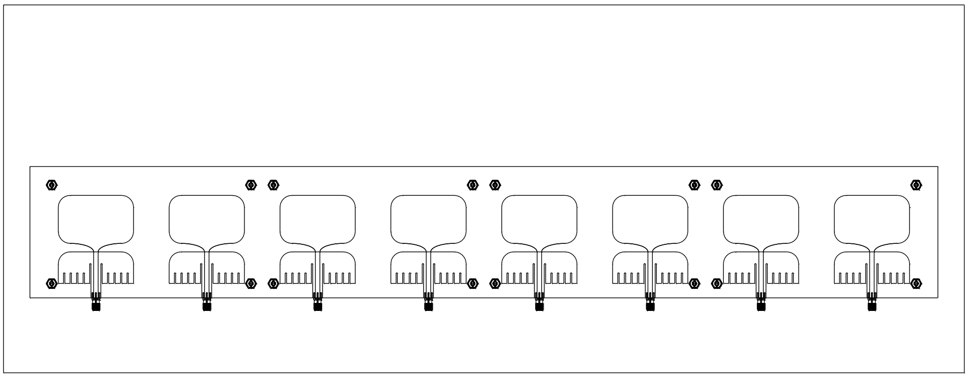

Figure 3.13- Top view sketch of the 8x1 monopole array

3.2.2.1 Array Structure

The array is done by duplicating the single monopole 8 times along the x-axis. The total length of the substrate is 688mm. This length is very big and couldn't be manufactured on a single substrate. For this reason, each two elements are printed on a single substrate. Each substrate is drilled from four corners and nylon spacers are fixed there as shown in Figure 3.14. The reflector is drilled at the exact locations of the substrates' corners and the substrates are fixed using nylon screws and nuts to the reflector. In this way, position uncertainties of the elements are prevented and hence no further calibration of such uncertainties is needed.

The elements are separated from each other by a distance of 84mm which is half wavelength for a frequency if 1.8GHz. The reflector's offsets from the edges of the antenna are maintained the same as those for the single monopole.

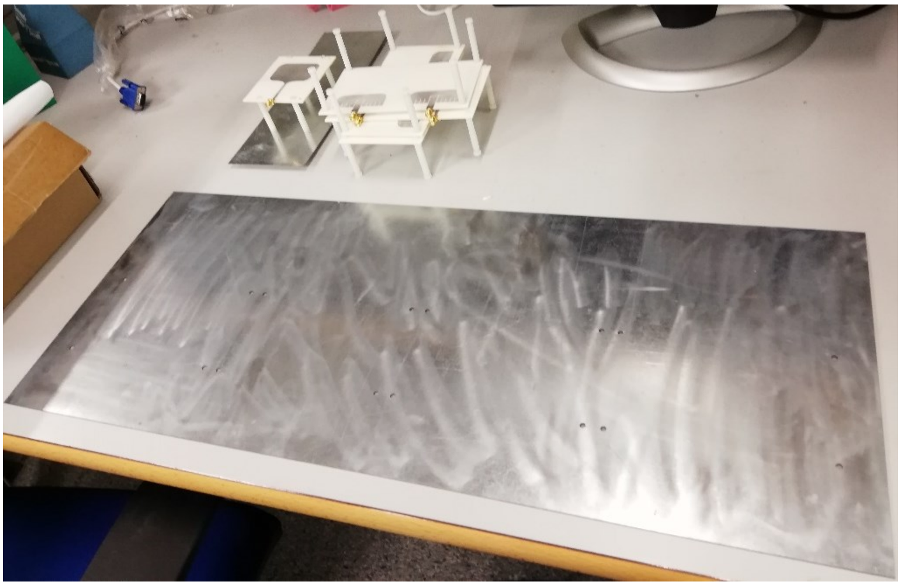

Figure 3.14- Antenna Array Assembly

The fully assembled 8x1 monopole array is shown in Figure 3.15. The four substrates are fixed to the reflector and the nylon screws are shown.

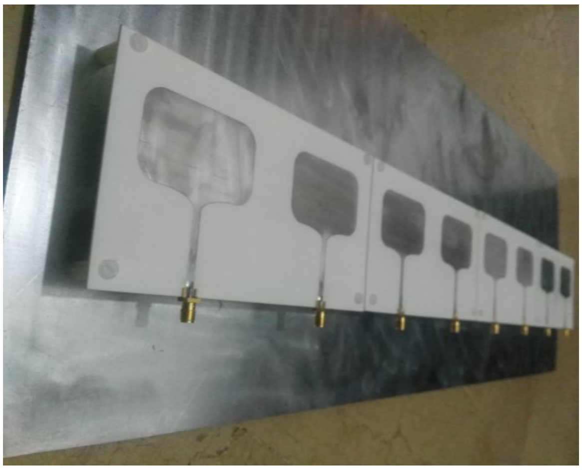

Figure 3.15- 8x1 assembled monopole array

3.2.2.2 Array Simulation and Measurement

The design of the array is based on the same single monopole design hence no parameters were tuned further during the array simulation. The two parameters that were tuned during simulation are the separation between the consecutive elements and the separation between the reflector and the antenna. After getting the optimum results in the simulation, the array has been manufactured and measured.

3.2.2.2.1 Measurement Setup

To measure the radiation pattern of the whole array, the array should be fed simultaneously from the eight ports. For this purpose, an eight-way splitter/combiner is used. The monopoles are connected to the eight-way combiner using phase matched cables. The combiner's output is connected to the network analyser outside the chamber.

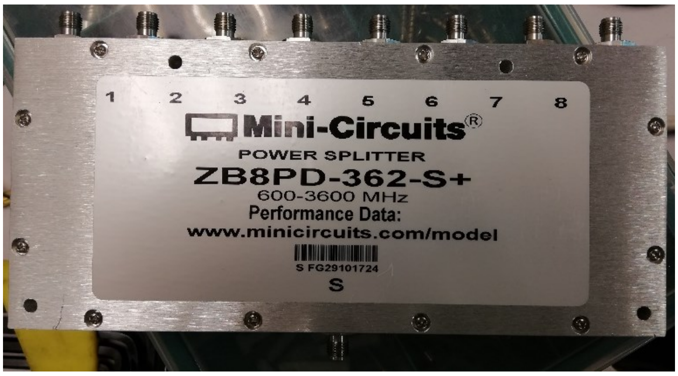

Figure 3.16- 8way phase matched splitter

The transmitter is connected to the Vivaldi antenna shown in Figure 3.17. The 8x1 array is made to rotate both in azimuth and elevation and controlled by an external computer and by an external network analyser. The data is then postprocessed and radiation patterns are produced.

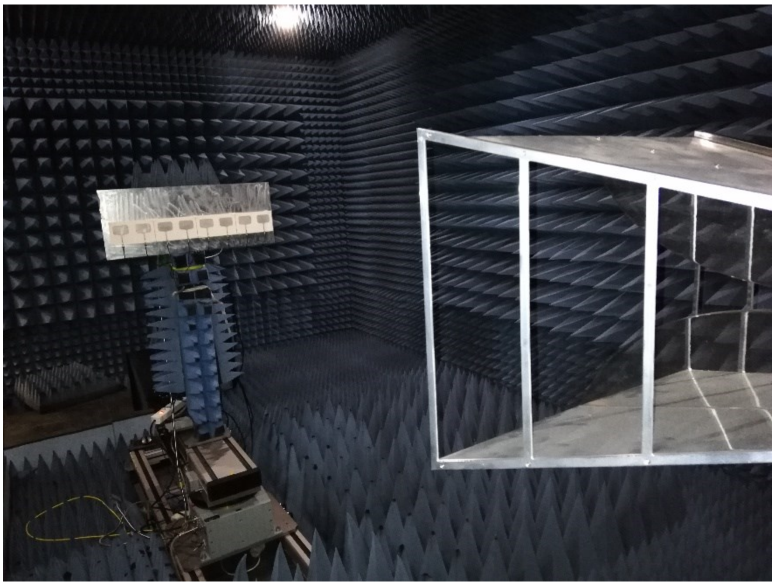

Figure 3.17-8x1 monopole array in the chamber facing the vivladi antenna

3.2.2.2.2 Measurement Results

After the simulation of the 8x1 monopole array, the gain radiation patterns at several frequencies were evaluated. The eight elements are uniformly fed in the simulator, so the results could be considered as a reference for the uniform fed measured array. The simulated

3-D gain radiation patterns at 1.7GHz, 1.8GHz and 1.9GHz are shown in Figure 3.18 a-1, b-1 and c-1 respectively. The results of the measurement at the same frequencies are shown in the same figure a-2, b-2 and c-2. By comparing those radiation patterns, it could be noticed that there is a slight distortion in the radiation patterns of the lower frequencies. The issue is significant at 1.7GHz but it is less at 1.8GHz and at 1.9GHz.

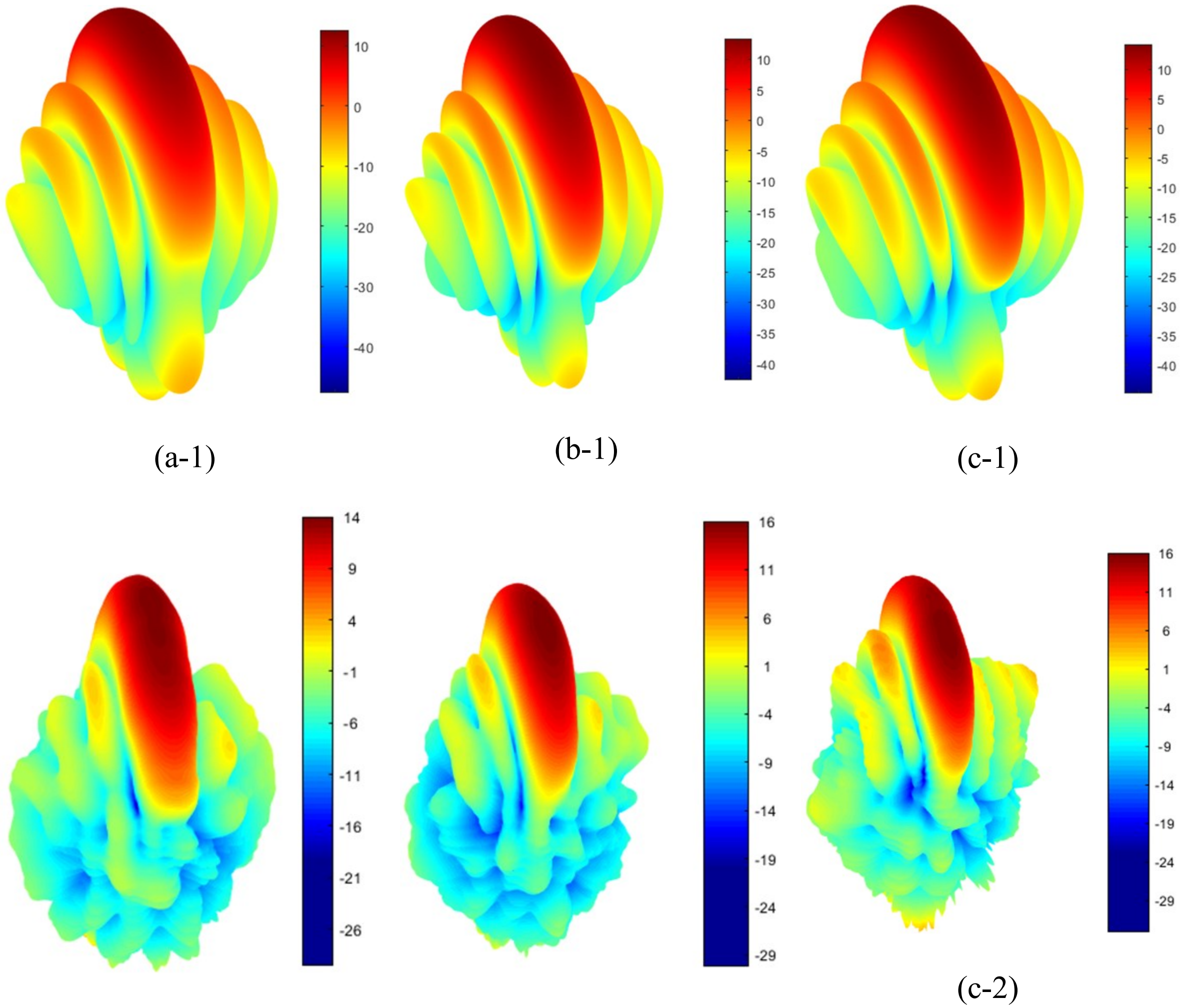

(a-1) (b-1) (c-1)

(a-2) (b-2) (c-2)

Figure 3.18- Simulated and measured 3-D radiation pattern of the 8x1 monopole array at 1.7GHz, 1.8GHz and 1.9GHz

The simulated 3-D gain radiation patterns at 2.5GHz, 2.6GHz and 2.7GHz are shown in Figure 3.19 a-1, b-1 and c-1 respectively. The results of the measurement at the same frequencies are shown in the same figure a-2, b-2 and c-2. The measured radiation patterns at these frequencies are compliant with those obtained by simulation.

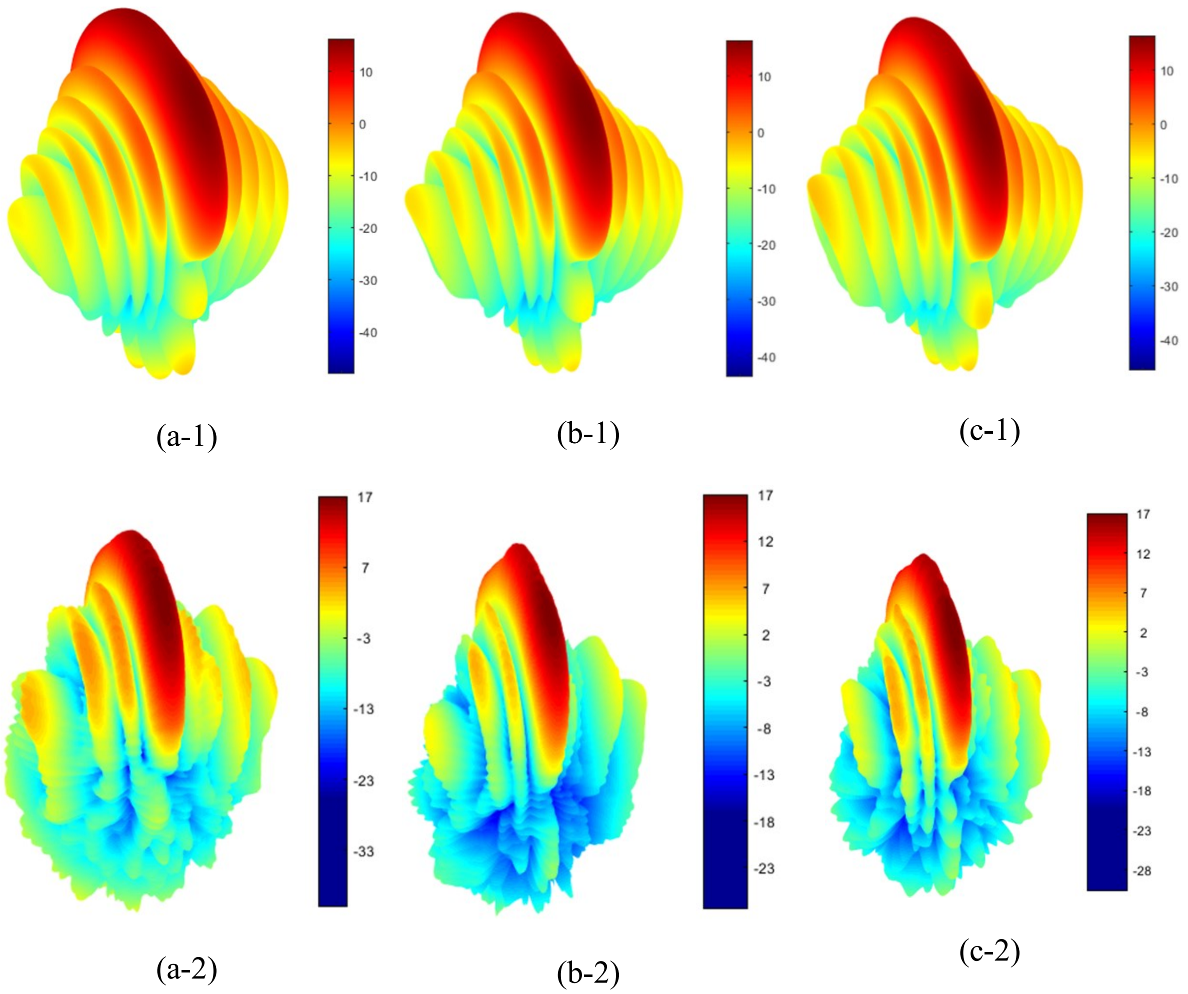

(a-1) (b-1) (c-1)

(a-2) (b-2) (c-2)

Figure 3.19- Simulated and measured 3-D radiation pattern of the 8x1 monopole array at 2.5GHz, 2.6GHz and 2.7GHz

H-plane cuts of simulated and measured radiation patterns at 1.7GHz, 1.8GHz and at 1.9GHz are shown in Figure 3.20 a, b and c respectively. Comparison between simulated and measured H-plane cuts of the radiation patterns show distortion for that corresponding to 1.7GHz and much better compliance at 1.8GHz and at 1.9GHz. In addition, back lobe level is higher for measured patterns.

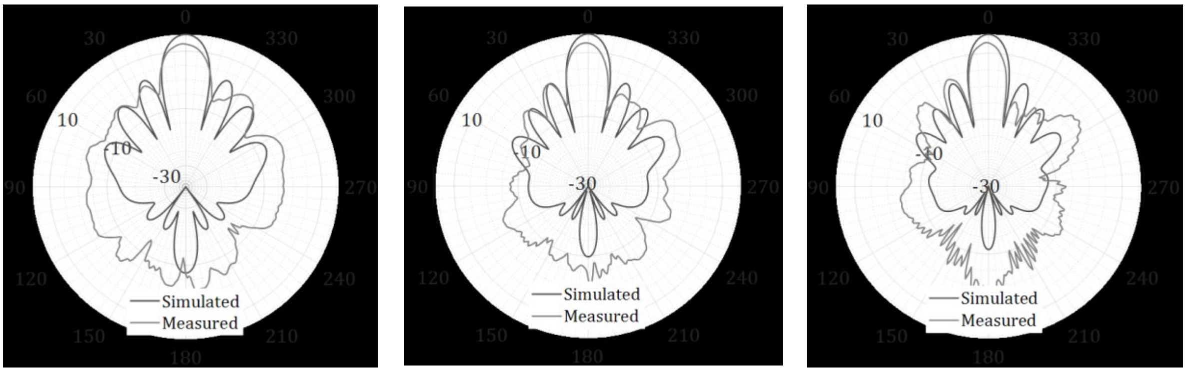

(a) (b) (c)

Figure 3.20- H-plane radiation pattern of the 8x1 monopole array at 1.7GHz, 1.8GHz and 1.9GHz respectively

The H-plane cuts at 2.5GHz, 2.6GHz and at 2.7GHz are shown in Figure 3.21 a, b and c respectively. It is noticed that sidelobe level for these patterns are slightly higher than those obtained from simulation. Maximum gain is almost identical, and the radiation patterns are almost the same. The back-lobe levels are also identical between simulated and measured.

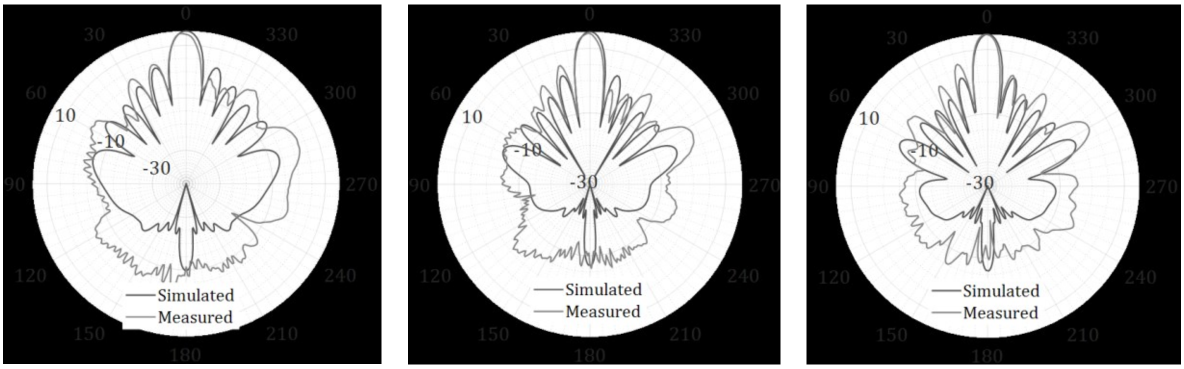

(a) (b) (c)

Figure 3.21- H-plane radiation pattern of the 8x1 monopole array at 2.5GHz, 2.6GHz and 2.7GHz respectively

The mutual coupling between consecutive elements was measured. The measure of mutual coupling indicates if the testbed needs to be calibrated for mutual coupling. S12, S34 and S23 are shown in Figure 3.22. The mutual coupling levels are below -18dB all over the operation band which is low. As a conclusion, no further calibration for mutual coupling is considered in this testbed.

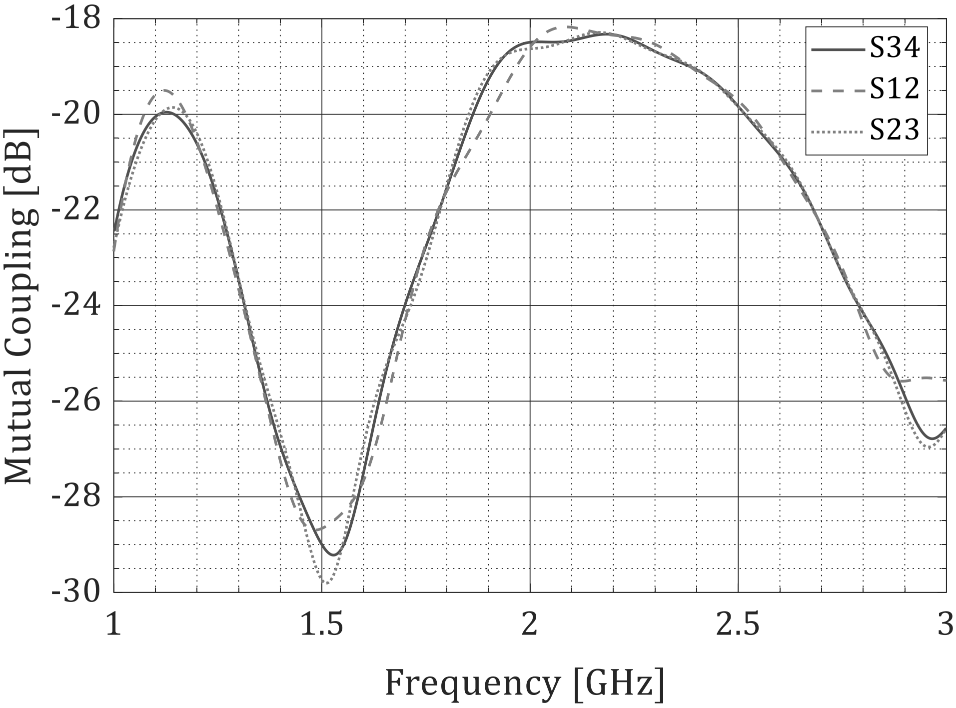

Figure 3.22- Mutual coupling levels for consecutive elements of the antenna array

3.3 RF-Front End and Processing Unit

In digital beamforming, phased array processing is done in the baseband. Algorithms are applied for the digital signals. A digital beamforming testbed should have an analog frontend, a high-speed high resolution analog to digital converter (ADC) and a digital signal processing unit.

The RF frontend's role is to receive RF signal from the antenna and prepare it for digitization. It contains a matching network, low noise amplifier (LNA), IF downconverter mixer and a low pass filter. RF signal from each antenna element have its dedicated analog front end.

The IF analog signal is introduced to the ADC. The I/Q output signals from the ADC are passed through an FMC connector to the FPGA, where all digital beamforming and post processing of received signals is done.

3.3.1 SDR Description

The SDR used in this testbed is FMCOMMS5 from analog devices combined with ZC702 SOC FPGA board from Xilinx. FMCOMMS5 is an evaluation board of AD9361 transceiver from Analog Devices. Each FMCOMMS5 board contains 2 AD9361 integrated circuits. The block diagram of a single AD9361 chip is shown in Figure 3.23. The device is composed of two separate receivers and two separate transmitters. Hence, full duplex communication is possible as each of the transmitters and receivers are standalone.

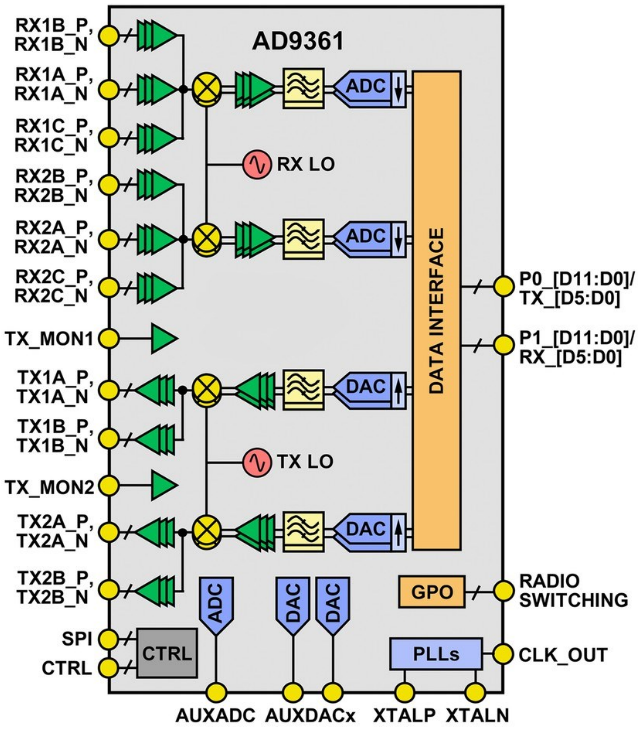

Figure 3.23- Block Diagram of AD9361 Integrated Circuit

AD9361 contains full chain from RF to baseband transceivers. FMCOMMS5 is the board that contains the circuitry required for the proper operation of the transceiver devices. This circuitry will provide proper signals to the RF ports, provide synchronized local oscillator for transmitters and receivers and interface the baseband signals to the baseband processor in the FPGA show in Figure 3.24.

The main DC line is provided from the FPGA through the FMC connector. The 3.3 input voltage is passed through an ADP2164 DC-DC converter to provide 1.8V DC supply. Several ADP1755 LDOs are used to provide several 1.3V DC supplies to bias several blocks of the transceiver chip.

The low noise amplifiers (LNAs) inside AD9361 are fully differential. For the single ended Antenna elements to be connectable to the LNAs, FMCOMMS5's RF ports are equipped with wide band baluns. The balun will then provide a balanced RF signal to the fully differential LNA.

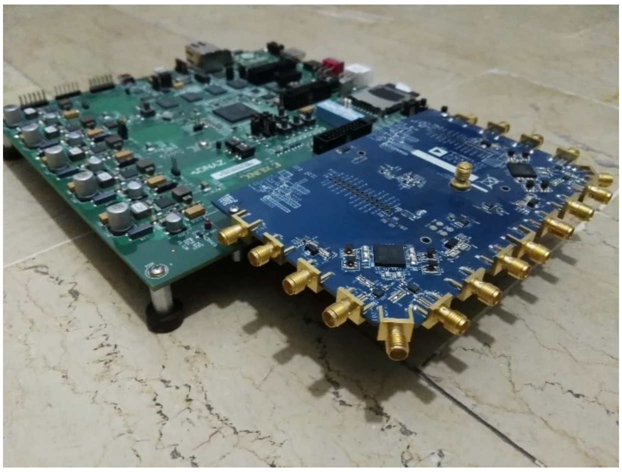

Figure 3.24- FMCOMMS5 SDR with ZC702 Xilinx FPGA

A 40MHz reference temperature compensated crystal oscillator (TCXO) is mounted on board. The reference clock is connected to a clock buffer with 3 outputs, ADCLK846. One of the three buffered 40MHz signals is directed to the local oscillator of the RF mixers as shown in [figure]. The second is passed to the FMC connector, and hence to the FPGA and the third is passed to the transceiver with the option to direct it to an external onboard header. The input 40MHz clock to the transceiver is used as ADC clock and for the digital circuitry inside the chip. The PCB traces from the clock buffer to the two transceiver chips is equal in length and then phase matched. An external reference could also be used with a PCB rework. In this case, the reference 40MHz signal is provided externally through an SMA coaxial connector.

The RF local oscillator is synthesized on the same PCB through a fractional phase locked loop. The 40MHz clock is used as reference for an ADF5355 PLL chip. ADF5355 is a 32-bit high resolution modulus PLL with integrated VCO. The chip can synthesize an output frequency in the range from 54MHz up to 13.6GHz. The high resolution of the modulus provides an output frequency resolution of sub hertz. A loop filter is cascaded with the charge pump output of the PLL circuit. The filtered output is a DC voltage, called V_{tune}, and is connected to the internal VCO of the chip. V_{tune} will force the VCO to generate alternating output frequencies until it reaches the intended one and the loop locks at it. The operation frequency for transmission and reception is programmable. What happens is that the PLL chip is programmed with the required operation frequency. The output of the synthesizer chip is passed to an Inphi 13617 high speed fanout buffer. 4 outputs are then applied to the transmitter local oscillator of the first chip, receiver local oscillator of the first chip, transmitter local oscillator of the second chip and receiver local oscillator of the second chip. The traces from the fanout buffer to the four inputs is constrained to be of the same electrical length. In this way all the 4 local oscillator signals are phase matched. An external Local oscillator could be used instead of the synthesizer circuit through an onboard SMA coaxial connector.

3.3.2 RF Analog Receiver

In AD9361, the receiver is a direct conversion system that contains a low noise amplifier (LNA), followed by matched I/Q amplifiers, mixers, and band shaping filters that down convert received signals to baseband for digitization. External LNAs can also be interfaced to the device, allowing designers the flexibility to customize the receiver front end for their specific application. Gain control is achieved by following a preprogramed gain index map that distributes gain among the blocks for optimal performance at each level. This can be achieved by enabling the internal AGC in either fast or slow mode or by using manual gain control, allowing the BBP to make the gain adjustments as needed. Additionally, each channel contains independent RSSI measurement capability, dc offset tracking, and all circuitry necessary for self-calibration. Block diagram of a single receiver chain is shown in Figure 3.25.

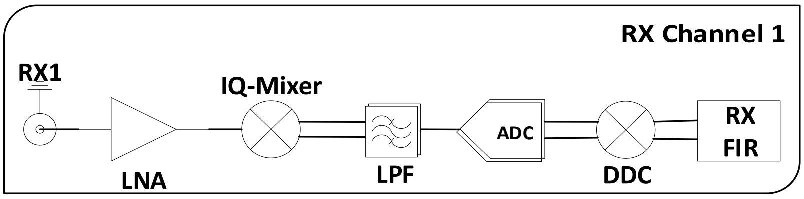

Figure 3.25- Single Receiver Chain

After the signal is converted to I/Q baseband signal, it is passed through I/Q programmable analog low pass filters. These filters reduce spurious signal levels by removing mixer products and providing general low pass filtering. The bandwidths of the filters are programmed according to the desired signal bandwidth. The Rx transimpedance amplifier (TIA) LPF is a single-pole low-pass filter with a programmable 3 dB corner frequency. The corner frequency is programmable over the range of 1 MHz to 70 MHz. However, The Rx base band LPF is a third-order Butterworth low-pass filter with a programmable 3 dB corner frequency. The corner frequency is programmable over the range of 200 kHz to 39.2 MHz.

Afterwards, the filtered signal is digitized by a 12-bit ADC. Four stages of digital decimating filters, that can be bypassed, follow the ADC. The digital Rx half band filters are used to eliminate over-ranging. The programmable digital filters provide the bandwidth limiting and out of band noise and spurious signal reduction after digitization. They also provide decimation needed to generate the correct data rates. In each filter, decimation is performed after the filtering has taken place.

AD9361 has an internal on chip PLL capable of synthesizing the required frequency for the ADC and sampling circuit. The on chip local oscillator circuitry contains a fractional PLL, integrated VCO and a loop filter with no need for external components.

Each receiver channel has three multiplexed RF input ports. Each of the three ports has an LNA operating from 70MHz to 6GHz. The three LNAs have differential inputs that can also be configured as single-ended inputs. The best noise figure is obtained with differential inputs. Inputs to the LNAs are DC biased internally with the required 0.6V. The maximum safe input level is +2.5 dBm peak. Wide band matching networks are used as the input impedance of the LNA is not flat.

One of the three available ports is chosen at a time suing the internal switching circuitry. Knowing that each chip contains 2 receivers, the total number of input ports is six ports. This could be exploited to implement switched phased array topology. In this topology, each input port is connected to an antenna element[76]. The control circuitry will switch between those input ports at a convenient speed. The switching speed should respect Nyquist rate in which the time needed to switch back to the same antenna element should be less than or equal to the Nyquist sampling period. In this way, the signals captured from all the elements will be weighted in phase and amplitude according to the direction of the source transmitting to the array. A single beam switched phased array was proposed and analysed in [77]. The effectiveness of sampled phased array technique was simulated and measured in [78]. Interference cancellation based on time domain sampling is performed in [79]. For the used receiver circuits, the response time for the switches controlling the input ports is significant. This will limit the sampling rate to low value and hence will limit the throughput of communication. For this reason, this approach was not considered in the development of the testbed.

3.3.3 Analog to Digital Converter and Digital Interface

The receivers include 12-bit, Sigma-Delta ADCs and adjustable sample rates that produce data streams from the received signals. The digitized signals can be conditioned further by a series of decimation filters and a fully programmable 128-tap FIR filter with additional decimation settings. The sample rate of each digital filter block is adjustable by changing decimation factors to produce the desired output data rate.

The AD9361 data interface uses parallel data ports to transfer data between the device and the FPGA. The data ports can be configured in either single-ended CMOS format or differential LVDS format. Both formats can be configured in multiple arrangements to match system requirements for data ordering and data port connections. These arrangements include single port data bus, dual port data bus, single data rate, double data rate, and various combinations of data ordering to transmit data from different channels across the bus at appropriate times. Bus transfers are controlled using simple hardware handshake signalling. The two ports can be operated in either bidirectional (TDD) mode or in full duplex (FDD) mode where half the bits are used for transmitting data and half are used for receiving data. The interface can also be configured to use only one of the data ports for applications that do not require high data rates and prefer to use fewer interface pins.

The data sent from the transceiver device to the FPGA is accompanied with a rate adjusting clock signal. This signal provides single data rate timing. The FPGA samples the incoming serial data at the rising edge of this clock signal.

The AD9361 contains a PLL dedicated to synthesize base band related signals. These include the ADC and DAC sampling clocks and the rate adjustment clock signal. This PLL is programmed from 700 MHz to 1400 MHz based on the data rate and sample rate requirements of the system.

3.3.4 ZC702 Xilinx FPGA

ZC702 is an FPGA development board from Xilinx. It contains XC7Z020 System on Chip (SOC) chip that contains dual core ARM CORTEX A9 and an ARTIX-7 FPGA. The FPGA has 85000 logic cells, 4.9MB block RAM, 200DSP slices and 200 I/O pins.

The development board has 16MB Quad SPI Flash memory and an SDIO card interface for booting operating system on the SOC. HDMI PHY and connector are implemented also to drive an external monitor or screen. In addition, the board contains 1GB DDR3 random access memory (RAM) and an I^2C 1KB EEPROM. The processing system of the ZC702 is clocked with a 33.33MHz single ended CMOS clock whereas the programmable logic banks are provided with a 200Mhz fixed frequency differential LVDS oscillator.

The board is supplied with external 12V power supply that feeds several low dropout regulators (LDOs). These LDOs provide the FPGA with the required voltage levels required for different banks and signalling technologies. The board also has the capability of measuring the voltage and the current of the regulators.

ZC702 is equipped with several communication interfaces. In addition to the gigabit ethernet interface, the board provides USB otg interfaced to the processing system section. Also, it contains a CAN bus, external I^2C, USB UART and several input output pins.

General purpose input/output means are available. Three user push buttons, two user switches and eight LEDS are provided. An external header is connected to an onboard ADC connected directly to the FPGA. The most important among all interfaces is the FMC connector. The board exhibits two FMC connector of low pin count (LPC). Each provides 68 single-ended or

34 differential signals. Those double FMC connectors provides the connection between the ZC702 board and the FMCOMMS5 SDR board.

The FPGA board is considered as the base band processor in this SDR. It receives the base band I/Q digital signals through thee double FMC connectors. The block diagram of the FPGA as a base band processor is shown in Figure 3.26. The functional blocks describe how received signals are post processed to be further exploited.

The digital interface consists of 12bits of DDR data and supports full duplex operation in all configurations up to 2×2. The transmit and receive data paths share a single clock. The data is sent or received based on the configuration (programmable) from separate transmit and to separate receive chains. Two receiver cores and two transmitter cores are implemented in the programmable logic of the FPGA. In the receiver core, the I and Q sample streams are processed each in a separate core. The samples pass through a monitor to validate signal capture and timing and then undergo DC filtering.

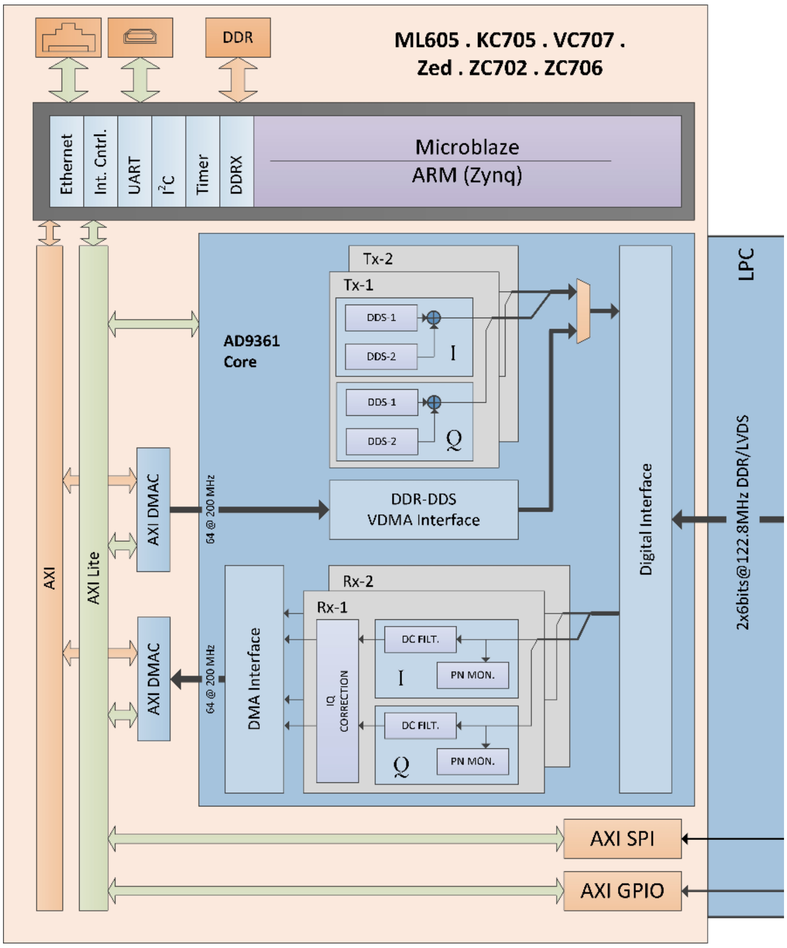

Figure 3.26- FPGA Functional Block Diagram

The outputs of the I and Q ports are then calibrated for I/Q imbalance, amplitude and phase mismatch. The corrected data are then written to the external DDR memory through the direct memory access core (DMA) and the AXI interface.

All the control and monitor signals are interfaced to the FPGA’s general purpose input output (GPIO). An AXI based SPI core is made to control the AD9361 operations.

The transmitter section is composed of two transmitter cores. Each composed of two cores for I and Q. The I and Q samples are made ready for RF transmission with direct digital synthesizer core that is programmable in phase and in frequency. The output samples are then filtered at the AD9361 before mixing with RF carrier.

The digital cores implemented in the FPGA are controlled from the dual core ARM processor on the Zynq SOC. For each block in the FPGA there is a driver to control its operation. Also a Linux based operating system could be used for easy graphical interfacing.

3.3.5 SDRs in Digital Beamforming

Software defined radios are hardware with configurable parameters of operation. These hardware incorporates radio frequency transmitters and receivers that are adjustable by software[80]. As shown in Figure 2.3, digital beamforming in reception requires full radio frequency receiver in addition to an ADC and a base band processor. Basically, this is supported by an SDR. An SDR would provide Radio frequency down conversion to the base band, analog to digital conversion and digital signal processing. SDRs, if incorporated in a phased array system, could provide a test bed for digital beamforming and direction of arrival estimation. This would increase the ability to add more antenna elements and would provide flexibility regarding algorithms used as array processing is performed on the received digital samples.

SDRs were used in beamforming and phased arrays in several projects. USRP N200 from Ettus was used in [81] to evaluate phased array for military applications. This phased array approach addressed the challenge of aligning oscillator’s phases for several elements. 2x2 MIMO was implemented using 7 inch vertical triband antennas and USRP 2920 in [82]. The system was used to study the performance of open loop MIMO schemes for mobile broadband radio access technology. A phased array based on ten RTL-SDRs along with a clock network are presented in [83], an antenna that reconfigures its radiation characteristics, turns on/off the array elements, by means of radio frequency (RF) switches in [84]. The antenna is software controlled by means of a suitable optimization technique that maximizes the signal-to-noise ratio (SNR) using USRP SDRs. In [85], CubeSat phased array ground station is demonstrated. It offers multiple simultaneous beams for communicating with and localizing multiple visible CubeSats. The ground station uses a receiver digital beamformer based on USRP N210 SDR at each antenna element. A project to investigate the possibilities of SDR Radar systems is presented in [86]. SAAB Electronic Defense (EDS) and Chalmers University of technology exploited NI-5791 SDRs from National Instruments to implement the SDR Radar on.

To find the best SDR to be used in this system, a comparison is done on available SDRs in market. The used SDR has several advantages over available SDR based systems regarding the price per element, the flexibility in the number of antenna array elements to handle, The receiver bandwidth and operation frequency range.

Some of the commercial SDRs are listed in Table III. A comparison is provided between the proposed test bed and other SDRs that shows the cost efficiency and dynamicity of the proposed testbed among other SDRs. The price per element describes the average price of utilisation of each channel in the SDR. The total number of channels should be equal to the number of antenna array elements.

According to Table III, DRU-244A is flexible in hardware as it supports multi-channel operation. The price per element for this SDR is about 2000 USD. This requires 16000 USD to have an eight element phased array. NI-5791, from National Instruments, is a generic and well developed solution. This SDR is also adaptable as number of elements could be increased without the need of further development. NI-5791 is equipped with synchronized clocking network provided by *FlexRIO* baseband processing board and daughter cards holder. Nevertheless, it requires *FlexRIO* baseband processing board that costs more than 10000 USD in addition to the 46080 USD as the price of eight elements. There are some very low cost solutions in market, like RTL-SDR. RTL-SDR has a single advantage which is it low cost. The provided receiver channel bandwidth is low (3.2MHz). In addition, ADC's resolution is very low (8 bits). Finally, RTL-SDR doesn't have external local oscillator option so no possibility for multi-receiver phased array operation. The most common SDRs in market are the USRPs from Ettus. USRP N200 covers the frequency range of interest but the price per element is about 1900 USD. Another solution from Ettus is the USRP 2920 SDR. This SDR covers narrower band and the cost per elements is about 3500 USD. LimeSDR competes with price, frequency range and performance but yet it is not a mature product and still under development.

USRP B210 is close to the proposed FMCOMMS5 based system regarding price and specs. The proposed system is of lower implementation cost with 475 USD per element.

Table III- Comparison between available commercial SDRs regarding price and flexibility

Platform/SDR	Frequency Range	Number of channels	Price in USD	Price per element in USD
USRP N200	DC to 6GHz	1	1855	1855
USRP 2920	50MHz to 2.2GHz	1	3440	3440
NI-5791	200MHz to 4.4GHz	2	11520	5760
RTL-SDR	24MHz to 1.76GHz	1	20	20
USRP B210	70MHz to 6GHz	2	1386	693
Crimson TNG	DC to 6GHz	4	13500	3375
LimeSDR	100KHz to 3.8GHz	2	300	150
DRU-244A-1-4PCI	IF 320MHz	1	1990	1990
Proposed System	70MHz to 6GHz	4x2	1900x2	475

Chapter 4 Beamforming and DOA Testing and Measurement

The system demonstrated in this thesis is intended to perform digital beamforming as well as direction of arrival estimation for RF sources transmitting toward the antenna array. The performance of this system should be tested. These tests and measurement will provide information about the performance and efficiency of the system. The tests are done in a controlled environment in order to isolate environmental and external effects.

In this chapter, testing setup procedure and requirements are described in 4.1. This section includes array calibration, chamber setup and transceivers configuration chosen in these measurements. In 4.2, test results are presented. Radiation patterns after beamsteering and beamforming are plotted. Angle estimation errors are evaluated after estimating DOA using various algorithms and the results are plotted. Further analysis of the results are also provided and conclusions are drawn.

4.1 Testing Setup

Before testing, several preparations should be done. These preparations are basically the steps needed to operate a phased array in optimal conditions. The testing conditions are meant to be controlled. Hence analysis of the results will reveal the performance of the testbed.

4.1.1 Array Calibration

Digital Beamforming is a phased array processing technique that is built on the assumption that the array is theoretically error free. Nevertheless, this assumption is not true, and the array requires calibration of various errors that usually exists. There are four types of errors in antenna array processing problems.

1. Array elements location errors
2. Phase and gain errors
3. Loss of coherence
4. Errors due to mutual coupling

Location errors exist due to the non-accurate positioning of the antenna array elements. The antenna array presented in this paper is printed on a substrate. When the antenna array elements are planar, the positioning errors are not likely to happen and are therefore ignored.

The relative phases and magnitudes between the elements are critical information. The errors in magnitudes and phases of the signals will lead to an inaccurate direction of arrival estimation and corrupted beam patterns after beamforming.

The coherence of the eight channels should be maintained. A drift in the local oscillator's frequency of any channel relative to the others will lead to performance degradation of the whole testbed. Hence, for proper operation of the testbed, it is necessary to make sure that the coherence between the eight channels is preserved.

Mutual coupling is the situation when the energy radiated from an antenna element would affect a closely placed antenna element. If the mutual coupling between antenna elements is significant, the performance of the beamforming system will degrade. In this case calibration for mutual coupling should be carried in order to reduce their effects on the steering capabilities of the beamforming system [87][88][89]. Mutual coupling between the 1st, 2nd, 3rd and 4th elements have been measured. As shown in Figure 3.23, the values are below -18 dB for the operation frequency range and hence the calibration for mutual coupling is not performed.

4.1.1.1 Multi-Channel Coherence

A major issue in multichannel operating systems, especially phased array and beamforming systems, is the coherence between the channels[90][91][92]. The operating channels should be frequency synchronized. A relative drift, even in the order of 10 Hz, in the local oscillators' frequencies will lead to the loss of coherence and hence the performance degradation of the testbed.

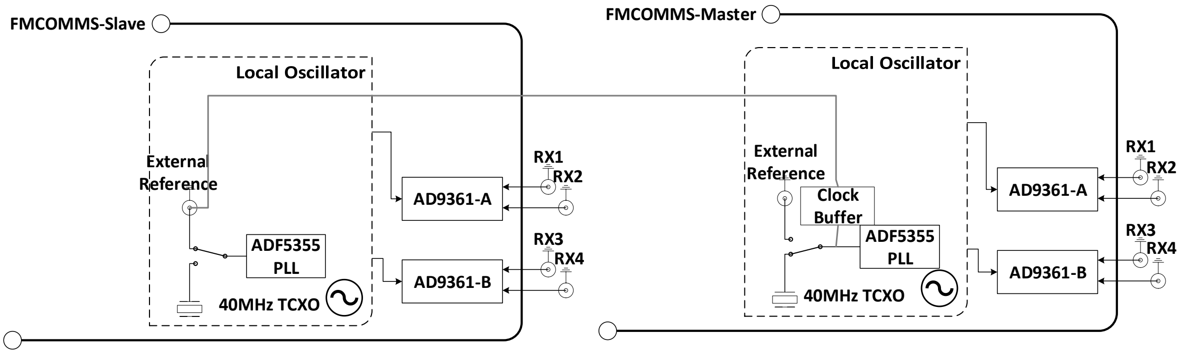

Figure 4.1- Coherent Topology for 8 Simultaneous Receivers Operation

The proposed testbed is composed of eight antenna element and hence requires eight coherent receiving channels. Each SDR board contains four dedicated receivers that can operate simultaneously. For that, two SDR boards are needed. Each of the two boards has its own local oscillator that is common to the four receivers and four transmitters. The local oscillator is a PLL ADF5355 from Analog Devices with a 40MHz TCXO crystal oscillator. There is no guarantee that the two boards' PLLs will lock at the same exact frequency knowing that the reference clocks provided by the 40MHz TCXO has a tolerance of 10ppm.

To ensure coherent operation of the eight receivers, the topology represented in Figure 4.1 is implemented. One of the SDR boards is considered as a clock master. The PLL in this board is driven by the 40MHz TCXO. The reference clock is then buffered and transferred through a coaxial cable to the external reference SMA connector on the slave board, as show in Figure 4.2, after enabling the external reference and disabling the built-in TCXO. When configured, both local oscillators will lock to the same exact frequency. In this way coherence is insured for the eight receiver channels.

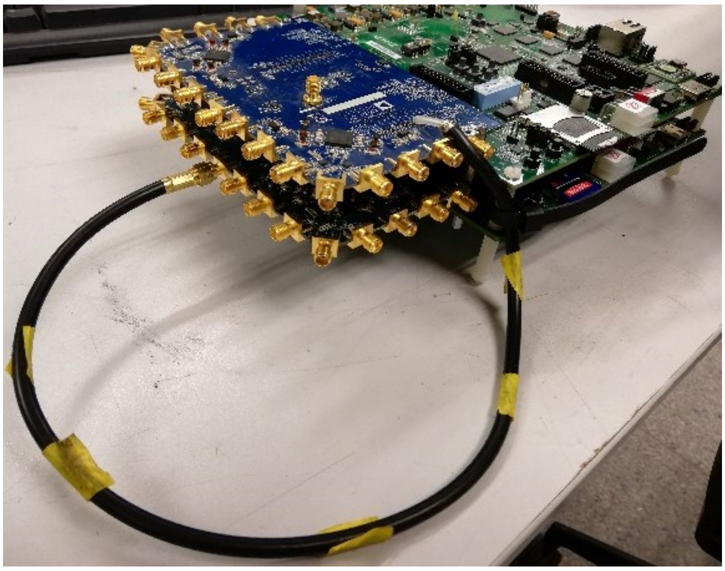

Figure 4.2- Reference clock sharing for 8 Simultaneous Receivers

4.1.1.2 Magnitude and Phase Uncertainties Calibration

Beamforming, as a phased array technique, requires the knowledge of the accurate phases and magnitudes perturbations. A major cause of these perturbations is the electronics incorporated. However, the parameters of electronic components vary with temperature and can drift over time. For that, each element of the antenna array should be calibrated for phase and magnitude errors[93]. Phase and magnitude calibration have been considered extensively in phased array contexts. A Control Circuit Encoding (CCE) technique is used for calibrating digitally controlled phased arrays[94]. The CCE method employs sets of orthogonal codes that are sequentially applied to all attenuators and phase-shifters in the beamformer, allowing elements to be measured simultaneously with a calibration probe in the far or near field of the array. a variable gain amplifier (VGA) in conjunction with the phase shifter to is exploited to compensate for the variable losses of the phase shifter and simultaneously provide a means of adjusting the amplitude of the signal [95]. An automatic calibration method using transmitting signals for adaptive base station antennas that is suitable for TDD communication systems is also presented in[96].

In this testbed, the eight signals received from the eight antenna elements pass through analog circuitry before being downconverted and digitized. The RF paths for each 4 receivers on the two boards, 8 receivers in total, are designed to have almost the same electrical length. As previously described and as shown in Fig. 10, beamforming for the eight-element array proposed in this system requires two SDR boards. Due to the master slave clock topology used, there is a phase introduced between the eight receivers. In addition, tolerances in PCB manufacturing and aging of various RF components perturb the phases of the eight signals. The perturbations in phases of the eight received signals make it a necessity to calibrate and align phases of all eight receivers. Also, the relative magnitudes of the received signals are crucial for beamforming. In order for this quantity to be consistent, calibration of gain uncertainties is done.

The magnitudes and the phases of the signals are translated from the RF signals to the digital baseband signals. i.e. the phase of the digital baseband signal is equal to the phase of the received RF signal at the level of the antenna added to the phase introduced due to the electrical length of the PCB traces. Also, the magnitude of the digital signal is the same as that of the RF signal multiplied by all the gains and attenuations of the LNA, transmission lines, filters etc.

The phase and magnitude calibration procedure is as follows:

1. A coherent channel topology is implemented for the two SDR boards used.
2. The 8 receiver channels are connected to the eight outputs of an eight-way power divider. The common input is connected to one of the available transmitters sharing the same local oscillator as the receiver channels.
3. A pilot signal is transmitted from the transmitter and received through coaxial cables by the eight receiver channels. The digitized signals will contain the magnitudes and phases of the original signals added to all the phase shifts and attenuations due to transmission lines, cables and receivers’ chain.

4. The phase of each signal is estimated as described in Appendix A.
5. The magnitude of each signal is estimated by using the I and Q components of the digital baseband signals.
6. After estimating the phases and magnitudes of all received signals, the phases should be compensated in order to have a zero-phase relative to the signal received from the first element. In this way all the phases that are non-relevant to the array processing are removed. An image of the magnitude and phase setup is shown in Figure 4.3. The magnitudes should be scaled to have all the received signals of unity relative magnitude to the first received signals.
7. The calculated phases and magnitudes are stored in a non-volatile memory and applied to each received signal accordingly in the post processing of the received data before any application of an array processing algorithm.

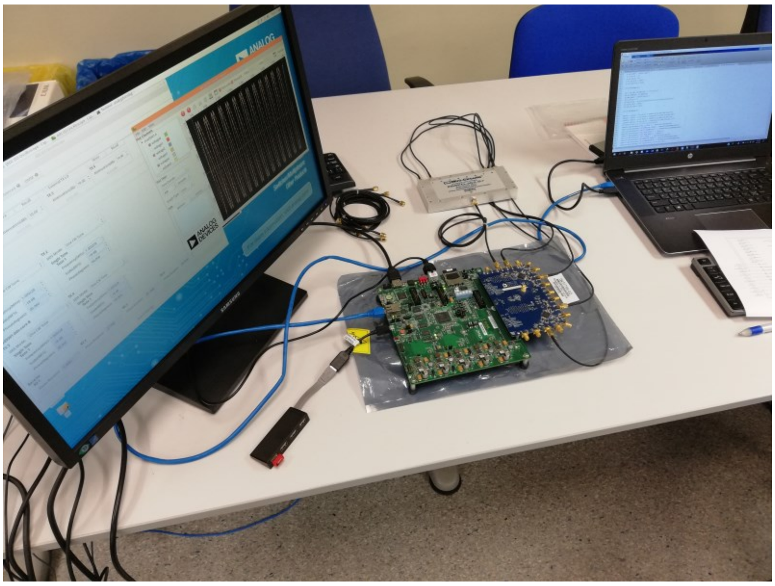

Figure 4.3- Phase Calibration Setup

4.1.2 Test Signal and Scenario

The performance and reliability of the system is tested. The tests conducted should have conditions similar to the real standard communication protocols. This includes RF carrier frequency, receiver channel bandwidth, modulation scheme, etc. In addition, performance of the system is tested for digital beamforming and DOA estimation. So the tests are performed on baseband digital signals and the test scenarios are chosen to capture digital signals from needed directions.

4.1.2.1 Test Signal

The test mimics a User Equipment (UE) signal transmitted toward a BS antenna array. Baseband data in LTE-A and in 5G NR are modulated with Quadrature Amplitude Modulations (QAM) [97] so the modulation scheme chosen is QPSK or 4-QAM. The test is performed with a signal of 2400 QPSK samples. The frequency of the RF carrier is set to 1.8GHz which is in the lower band of LTE-A[18]. For the receiver, the sampling rate is set to 200MS/s and the baseband channel bandwidth to 50MHz. The test signal is transmitted with an output power of 1dBm.

Table IV- Test Signal's Parameters

Carrier Frequency	Modulation	Receiver Bandwidth	Sampling Rate	Number of Samples	Output Power
1.8GHz	QPSK	50MHz	200MS/s	2400	1dBm

In this system, original amplitude and phase are necessary information. For this reason, the automatic gain control block is turned off. In addition, auto phase aligning function is disabled. The parameters of the test signals are summarized in Table IV. An example of received QPSK samples constellation is shown in Figure 4.24-a.

4.1.2.2 Test Scenario

The test is done on QPSK digitally modulated baseband data. An arbitrary bit stream is generated then modulated to QPSK. The I and Q streams are then filtered with a raised cosine filter and upsampled by 2. The modulated QPSK samples are converted to analog then modulated on an RF carrier of 1.8GHz. The RF signal is transmitted and the array of monopoles receive it on all the eight elements.

To test the system, signals at various angles should captured by the antenna array. The received digital baseband signals demodulated from these are then processed to perform beamforming or to estimate the direction of arrival of the signal. After post processing the recorded data, the system could be evaluated as good or need more work.

The measurements are done in an anechoic chamber to isolate the effects of scattering and signal echoes. The receiver channel, and as described in 3.3.2, down converts the received signal and digitizes it. The baseband data is then passed through a digital receiver block whose block diagram is shown in Figure 4.4.

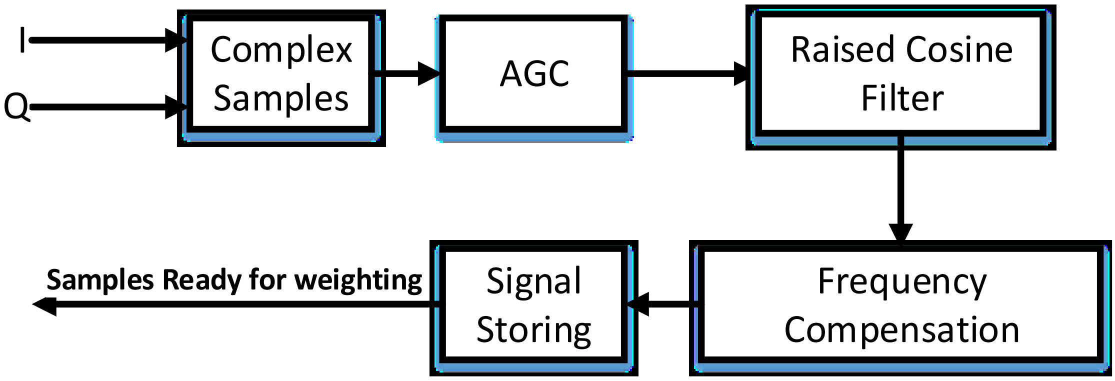

Figure 4.4- Single Channel Baseband QPSK Receiver

The I and Q digital samples are adjusted in amplitude if there is amplitude mismatch. The fixed samples are then downsampled by 2 by a raised cosine filter. Then frequency compensation of the received signal performed. This sequence is repeated for all the eight signals received by the eight elements antenna array. The data from the eight receivers is now stored. for Each angle of rotation of the Vivaldi antenna, there are 8 baseband signals available for postprocesing.

4.1.3 Anechoic Chamber Setup

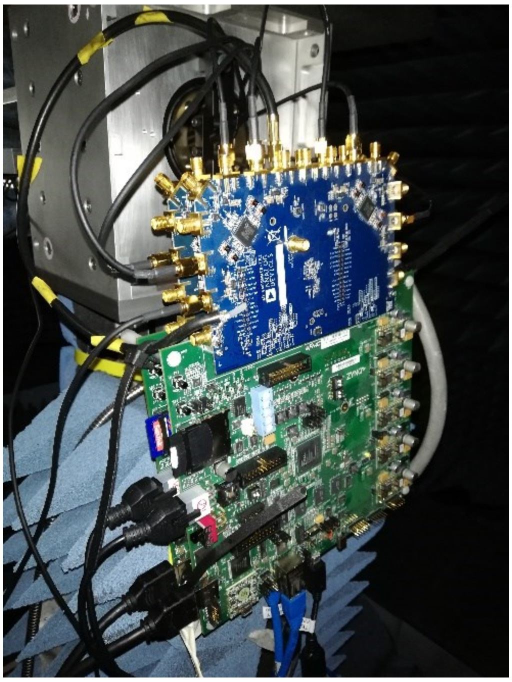

Figure 4.5- 8-elements SDR Unit in Anechoic Chamber

The SDR boards are connected as shown in Figure 4.5. The two cascaded boards are fixed to the metallic fixture as shown in Figure 4.5. The eight elements monopole array is mounted on the other side of the metallic fixture. Eight receiver channels from the SDR boards are connected through sma coaxial cables to the antenna array. The two boards are supplied with a 12V DC voltage source. Master clock board drives the slave clock board with the clock needed for coherent operation of the eight channels.

The transmitting antenna is a Vivaldi ultra wideband antenna. One of the transmitters on the boards, that share the same local oscillator with the receivers, is connected through rugged phase stable coaxial cable.

Initially, the eight channel receivers are connected to the eight way splitter that is connected in turn to one of the transmitters on the board. The phase and amplitude calibration procedure is then initiated as described in 4.1.1.2. The calibration setup is shown in Figure 4.6.

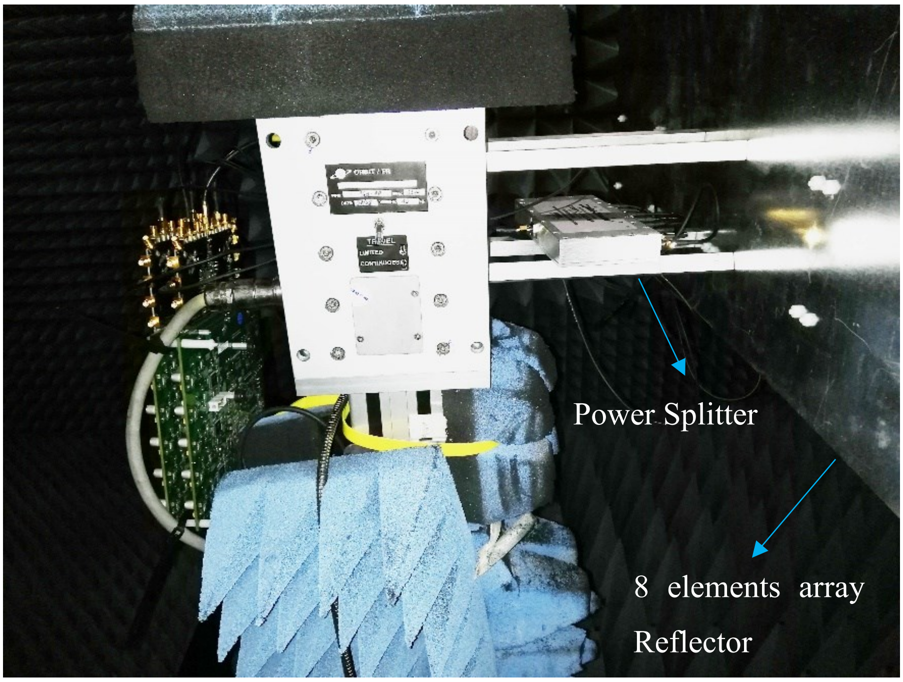

Figure 4.6- 8-elements Array Phase Calibration

After calibration is done, the eight receiver channels are connected directly to the antenna array. The transmitter needs 9 seconds to transmit one burst of data so the motor that rotates the Vivaldi antenna in azimuth is adjusted to an angular speed of 1/9 degree/s and is made to rotate from -90° to 90°.

While the antenna is transmitting, the receiver is made to capture signals at each 1/9 s that corresponds to a single degree. After the cycle is done, 8 different signals will be available for each of the 181° rotated angles.

4.2 Testing Results

The received signals are recorded with a one degree resolution as described in 4.1.2.2. The recorded digital data are postprocessed with beamforming algorithms in 4.2.1. Radiation patterns synthesized with Conventional beamformer's weights and LCMV beamformer's weights. DOA estimation is performed with one degree angle step in 4.2.2.

4.2.1 Beamforming

In these tests, weights calculated using Conventional beamformer, MVDR and LCMV beamformer are applied to the stored digital QPSK data. After weights application, radiation patterns are evaluated. The power is for the received signals is calculated based on the amplitudes of the digitally stored data after application of weights. This power is normalized to the maximum power in the look direction.

Complex samples, comprised of I samples and Q samples, are multiplied with complex weights. The signal received from first antenna element and re first receiver chain is multiplied by the first calculated complex weight and so on till the eighth signal and weight. Then all the weighted samples, at each angle alone, are summed up and power of the summed signal at each angle is evaluated.

4.2.1.1 Conventional Beamformer

The conventional beamformer is beamsteering beamformer. The weights produced by it are all of unity magnitude. The phases of the weights are derived to steer the main beam toward certain direction as stated in 2.4.1.1. The measurements conducted are done by postprocesing the received data with conventional beamformer's weights calculated using (2.45).

The radiation pattern evaluated using conventional beamformer's weights to steer the main beam to 60° is shown in Figure 4.7. The radiation pattern is normalized and it could be noticed that main beam to side lobe ratio is about -15dB.

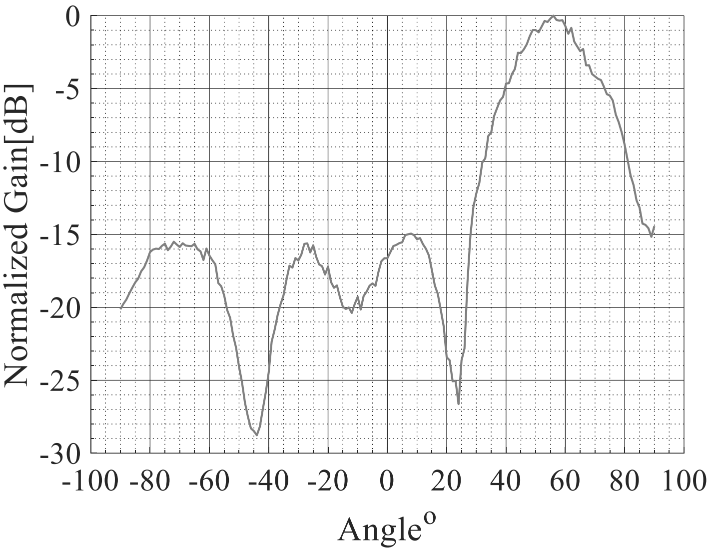

Figure 4.7- Conventional Beamformer's Response

Steering angle 60°

The test is performed also using weights for -55° steering angle. The radiation pattern produced is shown in Figure 4.8. Main beam to side lobe level is about -12dB. The peak of the radiation pattern is steered to -55° exactly without any drift.

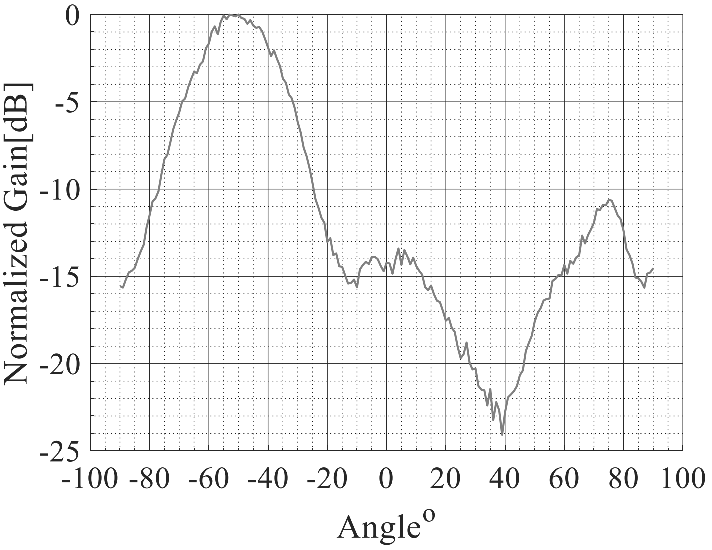

Figure 4.8- Conventional Beamformer's Response Steering angle -55°

Test was done also using the weights calculated for two intermediate angles. Weights at -40° steering angle and 20°. The radiation patterns are shown in Figure 4.9 and Figure 4.10 respectively. Side lobes levels are –15dB and less.

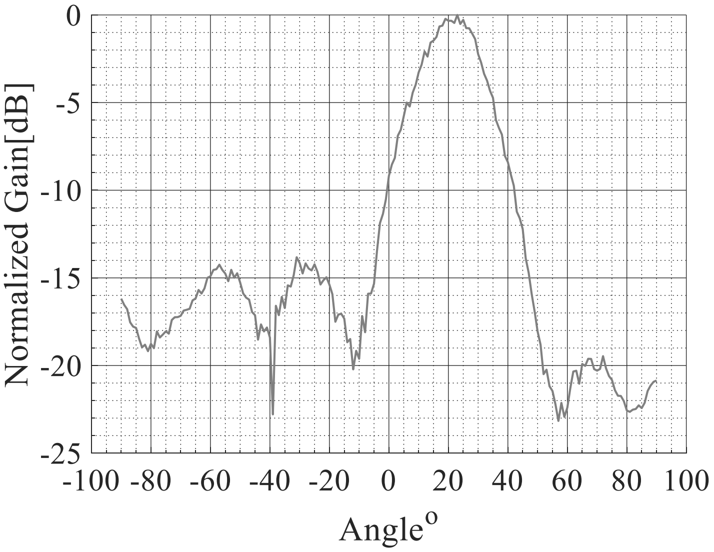

Figure 4.9- Conventional Beamformer's Response

Steering angle 20°

When scan angle approaches ±60°, the side lobe level starts increasing significantly. This is due to the formation of grating lobes.

In between ±60°, conventional beamforming reveals good results and convenient beamsteered radiation patterns.

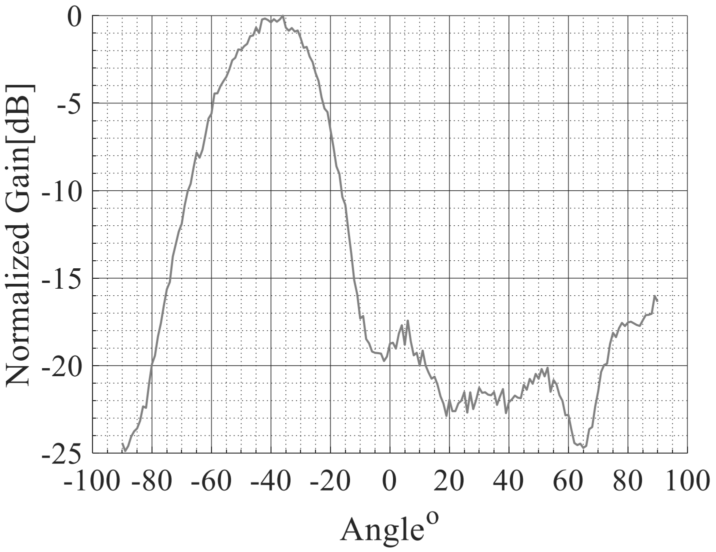

Figure 4.10- Conventional Beamformer's Response

Steering angle -40°

4.2.1.2 LCMV Beamforming

Steering vector beamforming gave good results regarding main beam gain level and side lobes levels. Nevertheless, steering vector beamforming capabilities are very limited. For example, it neither can provide null at interference direction nor it can support multi-beam.

LCMV beamformer algorithm was used in this context as an example to test beamsteering as well as null suppression capabilities of the system. As it is beamspace based beamforming algorithm, it is capable of producing multi-beams and multi-nulls.

Complex weights are calculated based on (2.56). The beamformer is constrained to have a maximum gain at -50° and 20° directions and a null in the supposed interference direction at -10°. The radiation pattern evaluated after signals weighting is shown in Figure 4.11. The radiation pattern complies with the constraints introduced to the beamformer. Two beams are produced at 20° and at -50°. A null is produced in the radiation pattern at -10°. The signal to interference ratio is -25dB. The difference in levels between the primary and the secondary beams is -2dB.

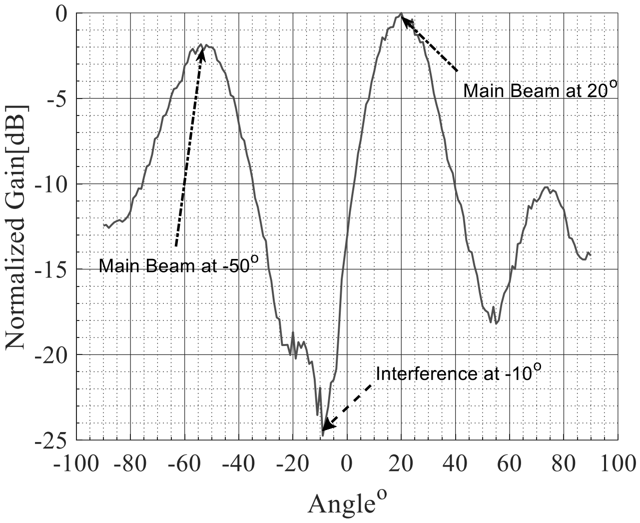

Figure 4.11- Radiation Pattern with LCMV Beamformer Weights with 2 Beams and 1 Null

The second test with LCMV beamformer is done with the weights being calculated for different constrains. The constraints are set to have a beam at -30° and two nulls at 5° and 40°. The radiation pattern produced reveals that the main beam is at -30° and two nulls are formed at the intended directions at 5° and 40° as shown in Figure 4.12. Signal to interference ratio is -26dB.

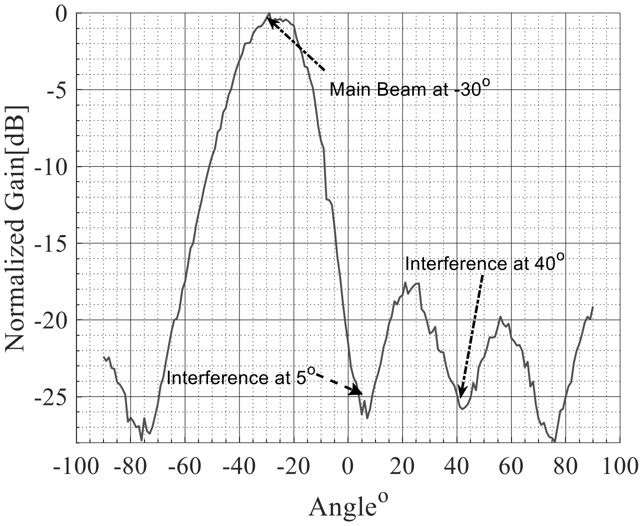

Figure 4.12- Radiation Pattern with LCMV Beamformer Weights with 2 Nulls and 1 Beam

4.2.1.3 MVDR Beamforming

MVDR Beamformer's weights are selected by minimizing the mean output power of the processor while maintaining unity response in the look direction according to (2.62). The constraint ensures that the signal passes through the processor undistorted. Therefore, the output signal power is the same as the look direction source power. The minimization process then minimizes the total noise including interference and the uncorrelated noise.

The first test was done by calculating and applying the MVDR Beamformer's weight for main beam direction at 10°. The beamformed signal contains two interferes at -40° and at 30°. The radiation pattern shows main beam steered to 10° and shows two nulls at 30° and -30° as show in Figure 4.13. The signal to interference ratio is -25dB in this case.

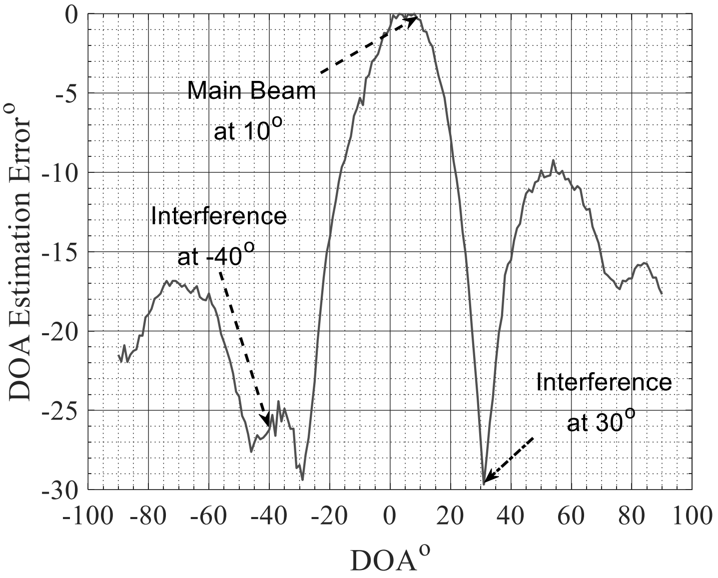

Figure 4.13- Radiation Pattern with MVDR Beamformer Weights with Beam at 10°

The second test was done by calculating and applying the MVDR Beamformer's weight for main beam direction at 40°. The beamformed signal contains two simultaneous interferes at -45° and at -10°. The radiation pattern shows main beam steered to 40° and shows two nulls at 0° and -50° as show in Figure 4.13. The signal to interference ratio is -20dB in this case.

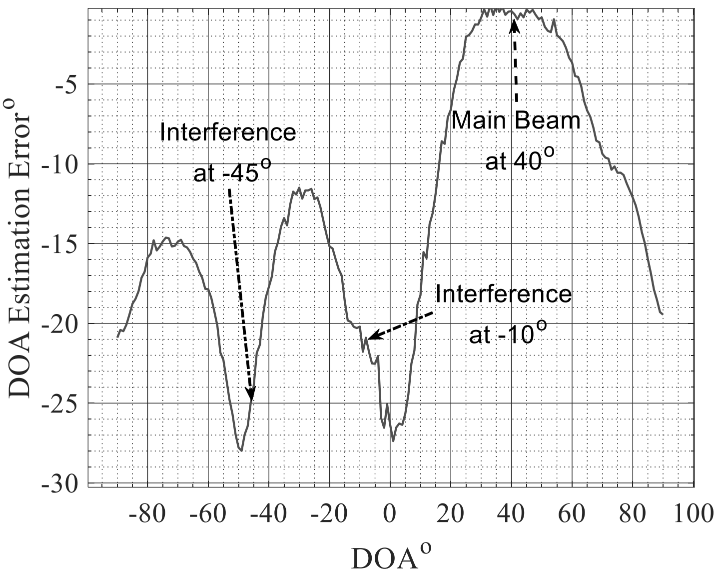

Figure 4.14- Radiation Pattern with MVDR Beamformer Weights with Beam at 40°

4.2.1.4 Radiation Patters Evaluation

From the conducted tests and its results, several issues could be noticed. The main beam steered to a certain angle is relatively wide. The half power beamwidth observed is about 10°. In addition, the maximum scan angle, or steering angle, in all beamforming algorithms is ±60°. Grating lobes start to form if the steering angle is driven beyond ±60°. Also, the primary and secondary beams are not of the same gain. The primary beam has the maximum gain and the secondary beam's gain is less by about 2dB.

On the other side, the resolution that is achieved by the system in beam and null steering is good. The system, by adjusting the beamformer's weights could attain a steering resolution of 1°. In addition, the signal to interference ratio (SIR) that is provided by MVDR and LCMV beamformers is high. The minimum achieved value is -20dB. MVDR gave the best SIR level of -30dB. It is worth noting that Nulls in MVDR radiation patterns are not at interference directions but the response of the MVDR weighted array with an interference is similar to a conventional beamformer without interference.

4.2.2 DOA Estimation

The system is tested with several direction of arrival algorithms. The purpose is to evaluate the system's reliability to estimate DOA of far field sources. The procedure followed is as follows. After received data is stored as described in 4.1.2.2, there is 8 digital signals from the 8 elements of the array at each angle. The transmitting Vivaldi Antenna is made to rotate from -90° to 90°. The DOA estimation algorithm is applied at the 8 signals from each angle and the angle is then estimated. This is repeated for the 181 directions.

4.2.2.1 MUSIC

MUSIC algorithm was performed on the received data at all angles. In MUSIC, pseudospectrum is calculated according to (2.79). The peaks in this spectrum is the estimated angle of arrival of the signal. A plot of the pseudospectrum evaluated on the signal when the Vivaldi antenna was rotated by -40° is shown in Figure 4.15. This angle is equivalent to 40o angle rotation of the antenna array.

The figure shows a peak in the pseudospectrum at 40°. In this case, the estimated DOA is equal to the incident angle. The power of the pseudospectrum plotted is normalized to the maximum power level. Nevertheless the peak is not sharp and it is considerably low.

The low pseudospectrum power level is not a good indication. It tells that a degradation in the performance of MUSIC DOA estimation algorithm might be happening. This degradation, even if it is not affecting the accuracy of angle estimation, is due to the *threshold effect*[98]. The peak level corresponding to the source emitting at a certain direction is reduced due to one if two causes. Either the SNR of the signal is low or when the sample size of the received digital signal is relatively small.

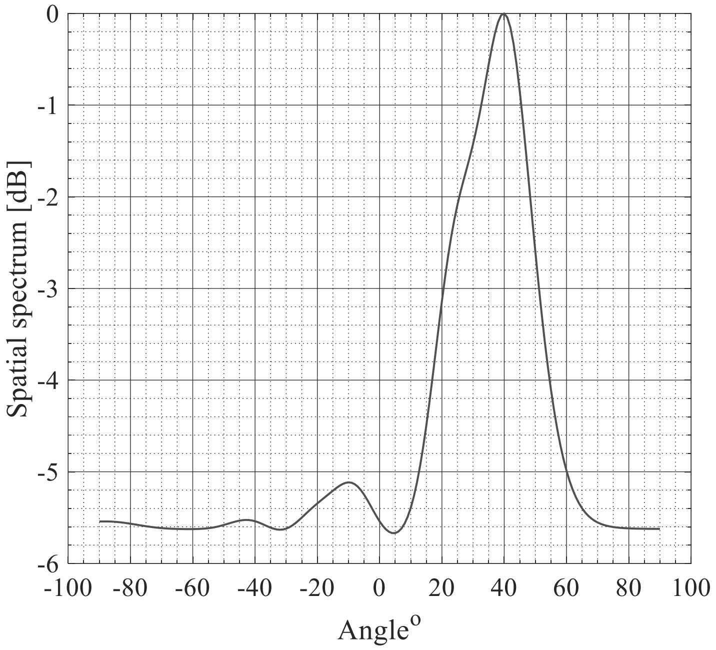

Figure 4.15- DOA Pseudospectrum for source at 40°

In conventional beamformer evaluation in 4.2.1.1, scan angle limitation is discussed. To analyze the effect of this limitation on DOA estimation, MUSIC pseudospectrum is plotted at which the received signal corresponds to-65°. The pseudospectrum is shown in Figure 4.16. The peak in the pseudo spectrum is formed at -60°. In addition, the pseudospectrum power level increased at the 90° direction. This justifies the degradation of the performance of DOA estimation outside the effective scanning range. This is mainly due to the formation of grating lobes.

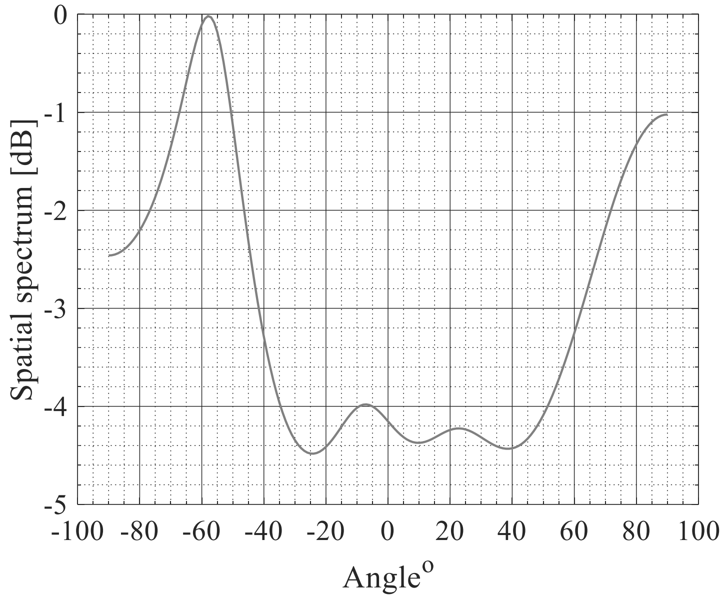

Figure 4.16- DOA pseudospectrum for source at -65°

DOA estimation using MUSIC is done on all the range of scan angles. The error between the estimated and actual angles is evaluated and plotted. DOA estimation error using MUSIC algorithm is shown in Figure 4.17.

The plot shows that the error of DOA estimation by this system using MUSIC algorithm is reasonable. It is enclosed between -0.5° and 0.5° over the angle scan range. It is noted that the error starts to increase as the angle approaches ±60°. This is predictable and complies with the pseudospectrum shown in Figure 4.16 as grating lobes start to form above ±60°.

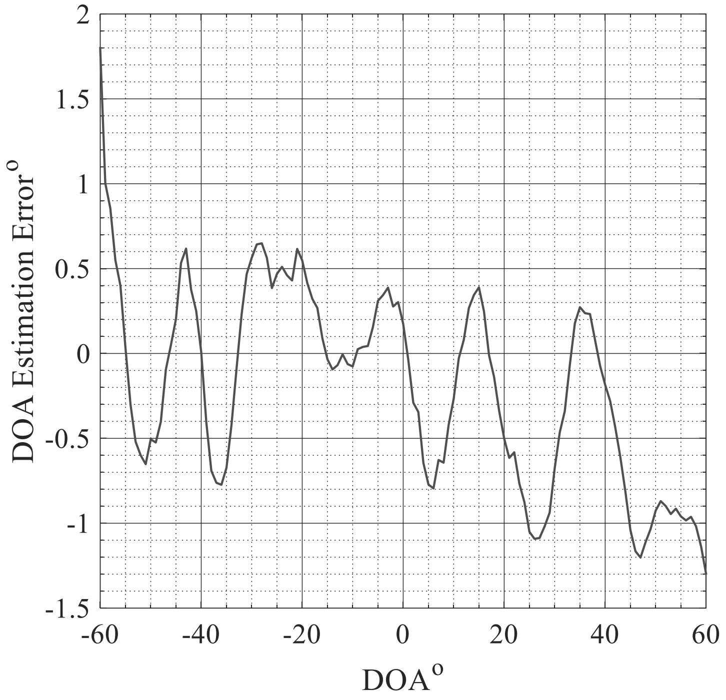

Figure 4.17- DOA estimation error by using 8-elements array and MUSIC algorithm

4.2.2.2 ESPRIT

ESPRIT DOA estimation algorithm is based on dividing the array into two subarrays. The signal autocorrelation matrices of each of the sub arrays are used to estimate, indirectly, the angles of arrival of the sources. The signal autocorrelation matrices of each of the two subarrays are evaluated. After that, a matrix whose eigenvalues are the directions of arrival, is calculated using (2.90). Then the angles are estimated from the eigenvalues. For this test scenario, ESPRIT is used to estimate direction of arrivals for the stored digital signals. The error between the actual and estimated angle is plotted in Figure 4.18

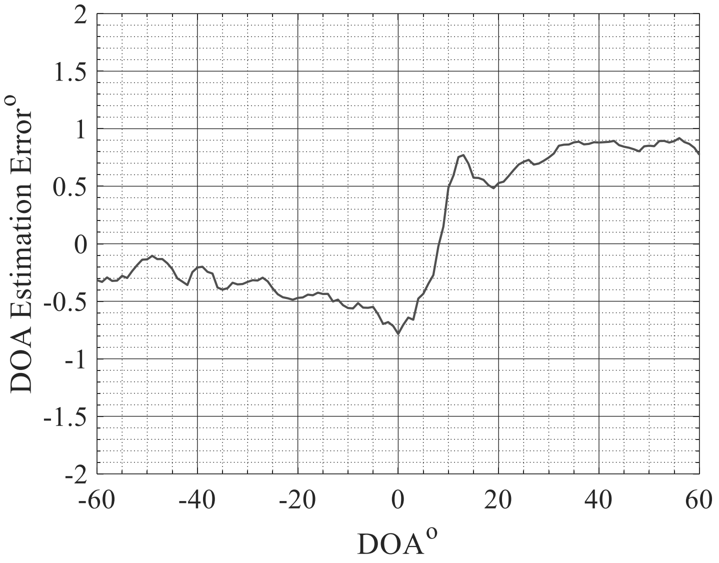

Figure 4.18- DOA estimation error by using 8-elements array and ESPRIT algorithm

By comparing Figure 4.17 and Figure 4.18, it could be noticed that ESPRIT produced more stable estimates. The positive negative alternation that exists in the MUSIC estimates is not present in ESPRIT estimates. The error is approximately enclosed between 0.5° and -0.5°. Nevertheless, the error is not symmetric. The error of estimated angles in the positive portion is slightly higher than that of the negative angles.

4.2.2.3 MVDR

Using MVDR DOA estimation algorithm, the digital data is used to extract the signal autocorrelation matrix. The power spectrum is calculated using (2.78) at each angle and using the calculated autocorrelation matrix and the steering vector at the specific angle.

In this test, the power spectrum is evaluated at each angle using the recorded digital data at each angle. The peaks in each spectrum at each angle reveals the estimated directions of arrival. A power spectrum plot for a source emitting at an angle of -19° is shown in Figure 4.19. At the direction of the source, the power spectrum has a peak that indicated the direction of the source.

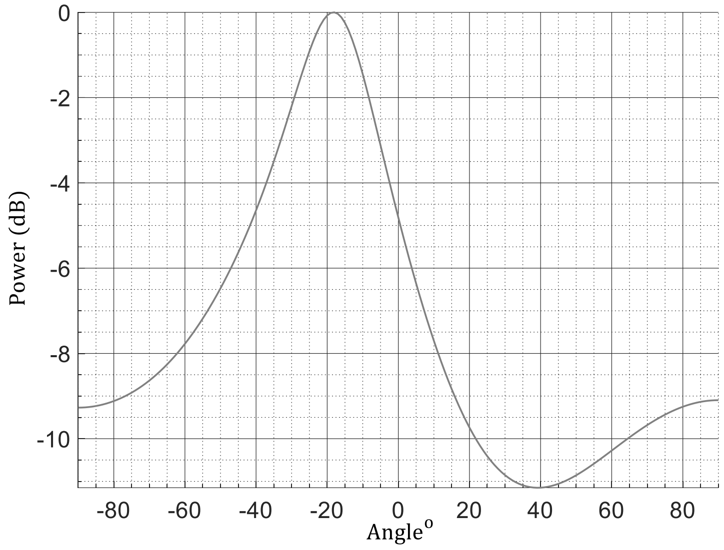

Figure 4.19- MVDR Power Spectrum for Source at -19°

As the source approaches the limit of the scan angle, the power spectrum starts to deform and no more peaks are formed. The power spectrum for a source emitting at -70° is shown in Figure 4.20. The peak formed at -70° is very weak and could not be discriminated.

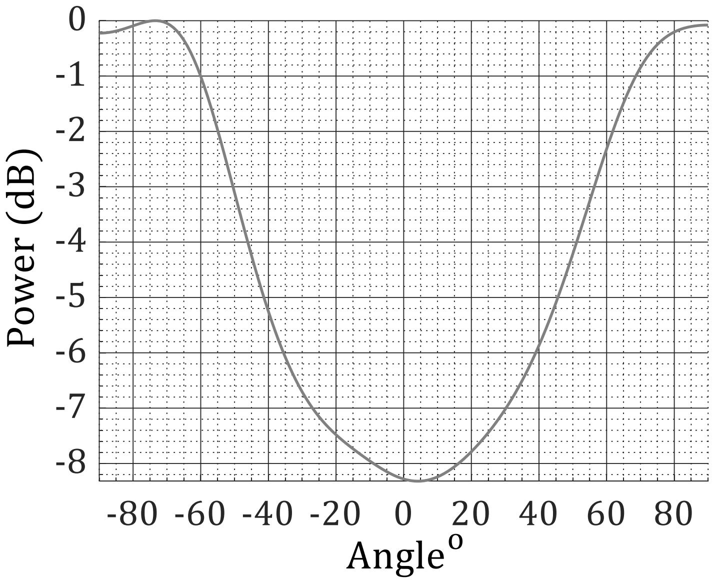

Figure 4.20- MVDR Power Spectrum for Source at -70°

The angle estimation error using MVDR algorithm is shown in Figure 4.21. The error plot asymmetric. The error is stable for negative angles and is around -0.5°. The error for angles above 0 is slightly more than 0.5° and is somehow not constant.

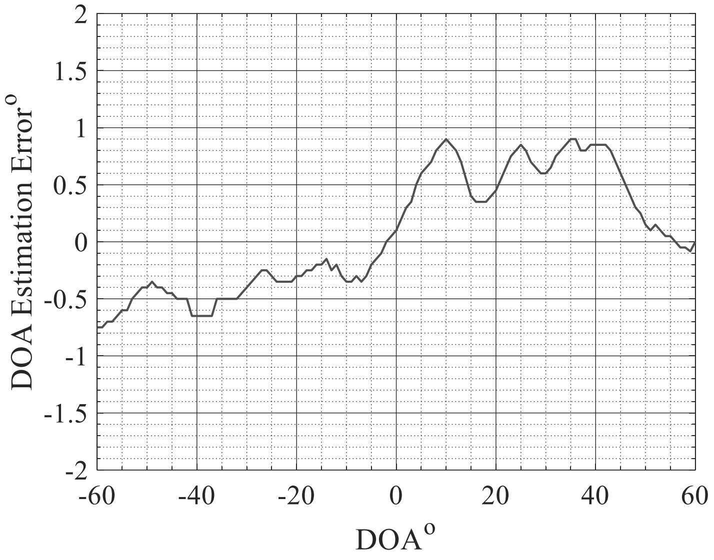

Figure 4.21- DOA estimation error by using 8-elements array and MVDR algorithm

4.2.2.4 Root MUSIC

Root MUSIC, as described in 2.4.2.3, relies on solving the polynomial equation of MUSIC pseudospectrum in (2.79). The roots calculated using (2.84) are used to estimate the direction of arrival of the rotating source using (2.85). Root MUSIC thus doesn't require the calculation of the pseudospectrum. Instead, roots of L^{th} degree equation are calculated.

The algorithm is applied at the 8 digital signals received by the eight monopoles at each angle. The algorithm estimates the direction of arrival at each angle step. The error between estimated and actual angles of arrival is shown in Figure 4.22. In addition to the asymmetry in the error, Root MUSIC estimated angles errors are alternating. Nevertheless, the error of estimation lies almost between -0.5° and 0.5° except at some positive angles.

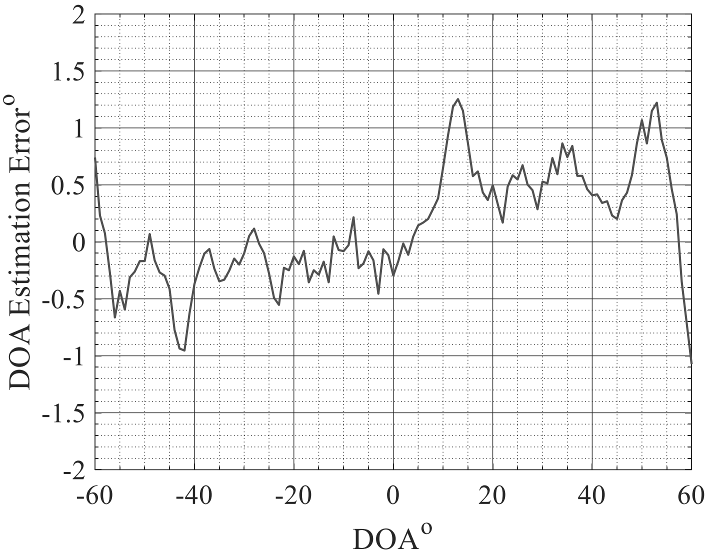

Figure 4.22- DOA Estimation Error for Root MUSIC Algorithm

By comparing Figure 4.17 and Figure 4.22, it could be noticed that the accuracy of estimation using Root MUSIC algorithm is better than that using spectral MUSIC. Estimation error bounces are smaller.

Conclusion

New digital communication standards, especially the upcoming 5G, relies on beamforming. Beamforming provides the base station with the power to maximize throughput and efficiency towards specific directions and minimize the effect of other directional interferers. This in turn will lead to higher SNR and though higher datarates. In addition, significant power could be saved. As the radiated power in concentrated toward certain directions, the demanded radiated power will be much less to fulfil the same channel budget.

Research in this domain is limited to specific research labs and companies as the equipment used are so expensive. Researches in personal basis or researchers from small institutes with limited budget do not have the ability to contribute and develop new algorithms for digital beamforming and direction of arrival estimation. In addition, they will never have the chance to do realistic trials for the performance of digital beamforming especially for radar and communication fields.

In this thesis, a phased array capable of digital beamforming is designed, simulated, assembled and tested. The system is constituted of 8x1 linear monopole array, SDR boards for RF to baseband conversion and an FPGA based base band processor. The system, as proposed, is a low cost and affordable solution for researchers.

Several Challenges faced the development of the system. The two SDR boards used were not designed to work in multi board topology. This required plenty amount of work to accomplish synchronous multi-board operation. In addition, several uncertainties are known to degrade the phased array performance. Phase and amplitude uncertainties are calibrated through a specific procedure. At the beginning, the results were bad. There was a problem with calibration sequence. Another challenge was that there was no way to estimate if the operation and calibration of the system is good until it is tested in the anechoic chamber.

After the system evaluation and measurements conducted, there are several points that could be concluded and improved. MUSIC pseudospectrum should have sharp peaks. In the measurements, the peaks levels are not high. This might risk measurement robustness in the case of noisy environment or high power interference. This indicates that finer tuning of the calibration should be considered. In addition, there is a point that should be investigated more in the DOA estimation. Error plots show asymmetry. The errors of estimation for positive angles are slightly greater than those of negative ones. This might be an indication of antenna array defect. This actually might need optimization of the reflector distance to the monopole.

From operational point of view, and despite the system is wide band, one major problem is the scan angle limitation. As the frequency of operation increases, the maximum scan angle decreases. And trying to steer for angles above the threshold will cause grating lobes formation and false DOA estimation. According to (2.41), in order to increase the maximum scan angle, the separation between antenna array elements should be decreased. Nevertheless, this will cause the mutual coupling to increase and hence degrade the performance of the system. This could be solved in the future work by decreasing inter-element distance and design a convenient mutual coupling calibration algorithm.

Nevertheless, the system's measurements show that its angle estimation accuracy is good. All the angle estimation error plots fall approximately between -0.5° and 0.5°. In addition, the system is capable of steering main beam and forming secondary beams with a high angular resolution. Angular steps of 1° are achieved. The system also provides high interference rejection. The recorded SIR values are more than -25dB. As a conclusion, the system provides an affordable, efficient and dynamic solution for researchers to contribute in building the new beam based radios for digital communication.

For the future, several points could be worked on or even enhanced in this system. As the system is evaluated and measured in a perfect and controlled environment, it is good to evaluate its performance in open space and in multipath propagation channels. Field trials for LTE-A, 5G and any Massive MIMO based technology could be performed. So in future releases it would be possible to include channel estimation and equalization in the system. DOA estimation measurements are done for a single radiating source. It will be also good to have trials with multi-sources, coherent and non-coherent ones. Narrower beams could be synthesized by increasing number of antenna array elements. Overall system performance could be enhanced by providing a single board solution. A single PCB with 4 AD9361 transceivers could be designed and tested to decrease the effects of noises, parasitic and uncertainties on system's performance.

Appendix A Phase Estimation

The received band-pass MQAM waveform may be represented as:

$$
\begin{aligned}
r(t) = G_a \sum_k \{ & a_0(k) p(t - kT_s) \sqrt{2} \cos(\omega_0 t + \theta) \\
& - a_1(k) p(t - kT_s) \sqrt{2} \sin(\omega_0 t + \theta) \} + w(t)
\end{aligned}
\tag{4.1}
$$

where $a_o(k)$ and $a_1(k)$ are the inphase and quadrature components of the k-th symbol, *p(t)* is the unit-energy pulse shape with support on $-L_pT_s \leq t \leq L_pT_s$, T_s is the symbol time, w_o is the center frequency in radians/second, θ is the unknown carrier phase offset, and w(t) is the additive white Gaussian noise. The constant G_a represents all the amplitude gains and losses through the antennas, propagation medium, amplifiers, mixers, filters, and other RF components. The received signal is sampled at a rate $F_s = 1/T$ samples/s. The n^{th} sample of the received signal is:

$$
\begin{aligned}
r(t) = G_a \sum_k \{ & a_0(k) p(nT - kT_s) \sqrt{2} \cos(\Omega_0 n + \theta) \\
& - a_1(k) p(nT - kT_s) \sqrt{2} \sin(\Omega_0 n + \theta) \} + w(nT)
\end{aligned}
\tag{4.2}
$$

where $\Omega = w_o T$ radians/sample. To estimates the carrier phase θ, the received samples should be downconverted from band-pass to I/Q baseband. This Quadrature sinusoids with a fixed frequency and phase to perform the translation from band-pass to I/Q baseband are used. Carrier phase offset compensation is performed by rotating the downsampled matched filter outputs to remove rotation due to carrier phase offset [99]. The phase compensation is realized by the "CCW Rotation". The block diagram of the phase estimation technique is shown in Figure 4.23.

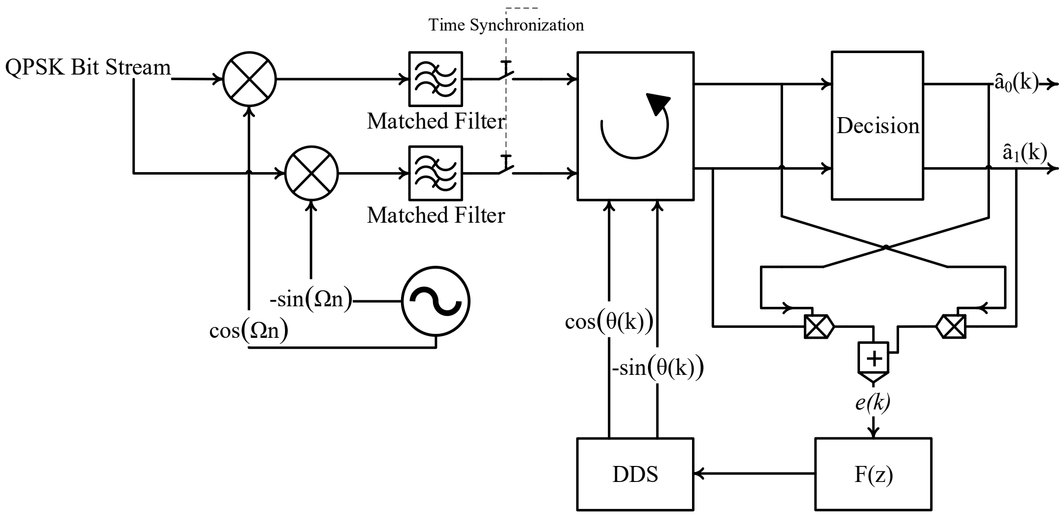

Figure 4.23-Block Diagram of the PLL Used for Phase Estimation

The signal space projections are given by:

$$\begin{bmatrix} x(kT_s) \\ y(kT_s) \end{bmatrix} = K \begin{bmatrix} \cos(\theta) & -\sin(\theta) \\ \sin(\theta) & \cos(\theta) \end{bmatrix} \begin{bmatrix} a_0(k) \\ a_1(k) \end{bmatrix} + \begin{bmatrix} v_I(kT_s) \\ v_Q(kT_s) \end{bmatrix} \tag{4.3}$$

The sampled matched filter outputs $\big(x(kT_s), y(kT_s)\big)$ are de-rotated by the estimated carrier phase offset $\hat{\theta}(k)$. The DDS provides carrier phase estimate as $\cos(\hat{\theta}(k))$ and $-\sin(\hat{\theta}(k))$. The point $\big(x(kT_s), y(kT_s)\big)$ is rotated by $-\hat{\theta}(k)$ to form the de-rotated signal space projection:

$$\begin{bmatrix} x'(kT_s) \\ y'(kT_s) \end{bmatrix} = K \begin{bmatrix} \cos\big(\hat{\theta}(k)\big) & \sin\big(\hat{\theta}(k)\big) \\ -\sin\big(\hat{\theta}(k)\big) & \cos\big(\hat{\theta}(k)\big) \end{bmatrix} \begin{bmatrix} x(kT_s) \\ y(kT_s) \end{bmatrix} \tag{4.4}$$

This relationship defines the operation of the "CCW Rotation" block in Figure 4.23. Using (4.3, the de-rotated signal space projection may be expressed as

$$\begin{bmatrix} x'(kT_s) \\ y'(kT_s) \end{bmatrix} = K \begin{bmatrix} \cos\big(\theta - \hat{\theta}(k)\big) & -\sin\big(\theta - \hat{\theta}(k)\big) \\ \sin\big(\theta - \hat{\theta}(k)\big) & \cos\big(\theta - \hat{\theta}(k)\big) \end{bmatrix} \begin{bmatrix} a_0(k) \\ a_1(k) \end{bmatrix} + \begin{bmatrix} v_I'(kT_s) \\ v_Q'(kT_s) \end{bmatrix} \tag{4.5}$$

This shows that the signal space projections $\big(x(kT_s), y(kT_s)\big)$ are rotated versions of the constellation point $\big(a_0(k), a_1(k)\big)$ where the rotation angle is the phase error $\theta - \hat{\theta}(k)$.

Constellation plots of qpsk signal and a rotated version of it using the CCW rotation block is shown in Figure 4.24.

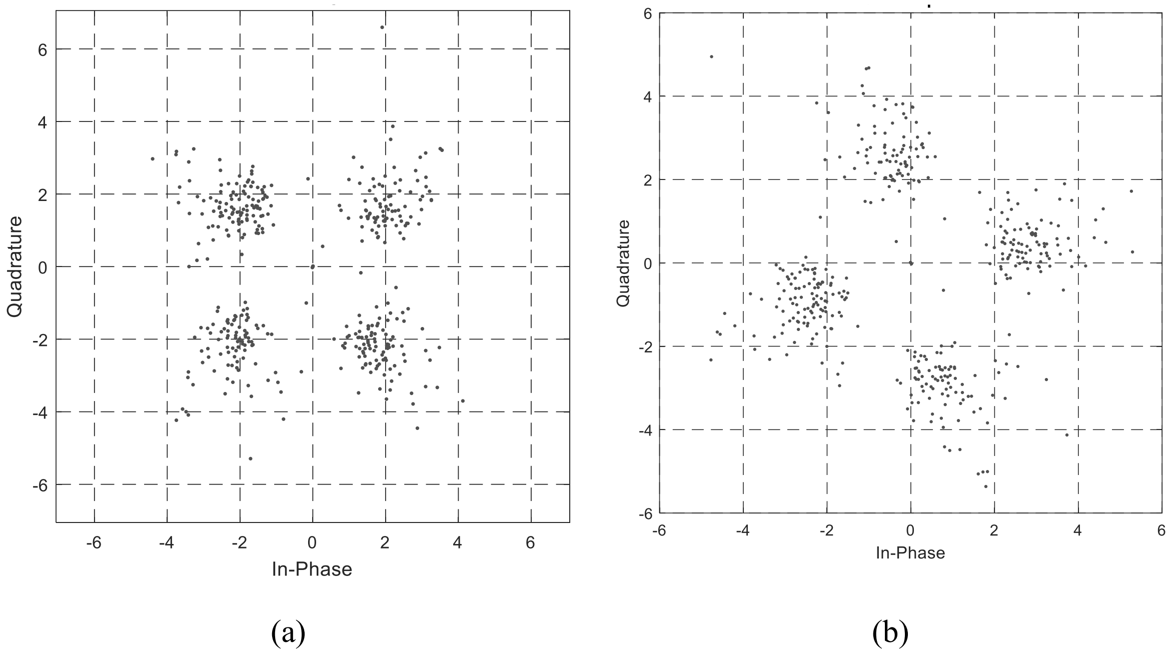

Figure 4.24- Impact of Counter clock wise rotation on the QPSK constellation in the ML PLL

The carrier phase PLL is formed by the closed-loop path created by the phase detector, loop filter, and DDS as illustrated in Figure 4.23. The PLL locks when the error signal is forced to zero. The error signal is generated by the "Compute Phase Error" block using the de-rotated signal space projections and the data symbols. The error signal is proportional to the uncompensated phase error $\theta - \hat{\theta}(k)$. Thus, the loop locks when $\hat{\theta}(k)$ is equal to θ.

Because the sampled matched filter outputs form a discrete-time sequence, this approach is a purely discrete-time approach. When the phase error detector uses the symbol estimates to compute the phase error, the resulting PLL is called a decision-directed loop. Alternatively, the phase error may be computed using knowledge of the transmitted data symbols. Usually, the known data takes the form of a predefined data sequence, known as a training sequence that is inserted at the beginning of the transmission for the purposes of phase acquisition. This approach is commonly used for packetized data links where the training sequence forms part of the packet header or preamble. A carrier phase PLL that uses known data is often called a data aided PLL. Most PLLs operate in the decision-directed mode. This being the case, decision-directed PLLs are emphasized in the following sections. Application of the ideas presented in the following sections to the data-aided case is straightforward.

The maximum likelihood (ML) phase error detector selects a phase estimate $\hat{\theta}$ that minimizes the energy in the phase error $\theta_e = \theta - \hat{\theta}$. A derivation of the ML phase error detector starts with the heuristic phase and uses the sine of the phase error rather than the actual phase error. Using sine identity,

$$\cos\big(\theta_r(k) - \theta_d(k)\big) = \sin\big(\theta_r(k)\big)\cos\big(\theta_d(k)\big) - \cos\big(\theta_r(k)\big)\sin\big(\theta_d(k)\big) \tag{4.6}$$

$$= \frac{y'(kT_s)a_0(k) - x'(kT_s)a_1(k)}{\sqrt{x'^2(kT_s) + y'^2(kT_s)}\sqrt{a_0(k)^2 + a_1(k)^2}} \tag{4.7}$$

The ML phase error for the data-aided case is

$$e(k) = y'(kT_s)a_0(k) - x'(kT_s)a_1(k) \tag{4.8}$$

The decision-directed version of the ML phase error detector is obtained by replacing

$a_0(k)$ and $a_1(k)$ in (4.8 with $\hat{a}_0(k)$ and $\hat{a}_1(k)$:

$$e(k) = y'(kT_s)\hat{a}_0(k) - x'(kT_s)\hat{a}_0(k) \tag{4.9}$$

For QPSK, the decisions are

$$\hat{a}_0(k) = A \times sgn\{x'(kT_s)\} \tag{4.10}$$

$$\hat{a}_1(k) = A \times sgn\{y'(kT_s)\}$$

The PLL will keep processing samples until it converges to a 0 phase error. In that case, the estimated phase will be the phase of the QPSK signal. A QPSK test signal was applied to the

ML phase estimator shown in Figure 4.23. The constellation of the test signal is shown in Figure 4.25.

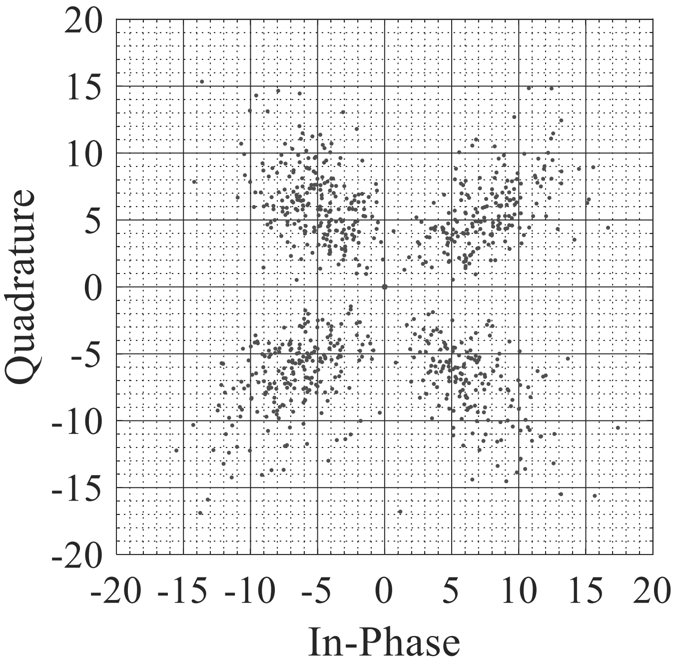

Figure 4.25-Test signal Constellation

Phase estimation convergence is shown in Figure 4.26. In the beginning, the estimated phase was 0°. As the number of iterations increases, the slope of variation of the estimated phase starts decreasing until it reaches a stable phase estimate of -45° after 400 samples as shown in Figure 4.26. The phase estimate is consistent with the test signal's phase.

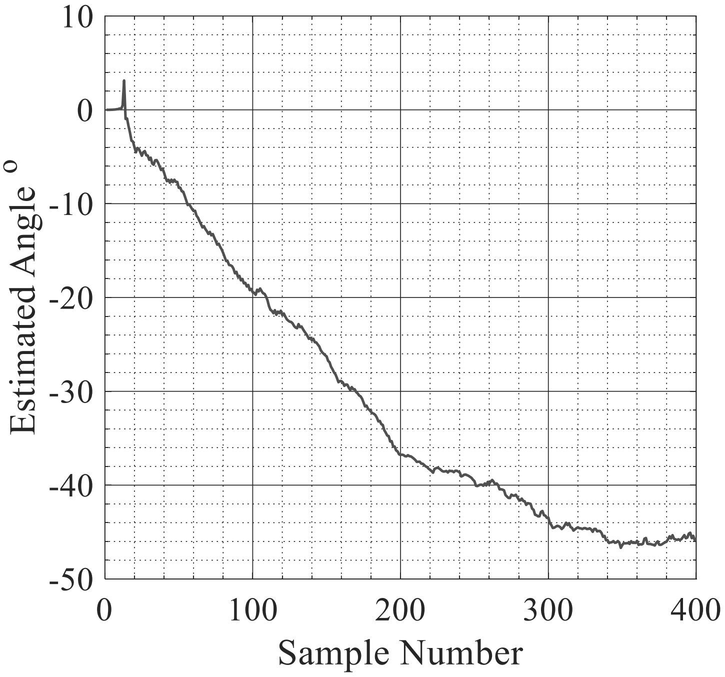

Figure 4.26- Convergence of the Estimated Angle with Samples Number

References

[1] A. T. Glossary, "http://www.atis.org/glossary." .

[2] J. Wenger, "Automotive Radar - Status and Perspectives," *IEEE Compd. Semicond. Integr. Circuit Symp.*, pp. 21–24, 2005.

[3] P. Bocon, T. McGree, and J. Renfro, "Phased Array Performance Characteristics and Compliance with SATCOM Military Standards," in *Military Communications Conference*, 2005, pp. 1–7.

[4] T. Maese *et al.*, "Dual-Use Shipborne Phased Array Radar Technology And Tactical Environmental Sensing," in *Radar Conference*, 2001, pp. 7–12.

[5] S. P. Stapleton and G. S. Quon, "A Cellular Base Station Phased Array Antenna System," in *IEEE International International Conference on Selected Topics in Wireless Communications*, 1992, pp. 93–96.

[6] T. B. Vu and G. Jonas, "On smart base-station antennas for mobile communications," in *IEEE Antennas and Propagation Society International Symposium. 1996 Digest*, 1996, vol. 1, pp. 710–713 vol.1.

[7] H. T. Friis, C. B. Feldman, and W. M. Sharpless, "The Determination Of The Direction Of Arrival Of Short Radio Waves," *Proc. Inst. Radio Eng.*, vol. 22, no. 1, 1934.

[8] H. T. Friis and C. B. Feldman, "A Multiple Unit Steerable Antenna For Short-Wave Reception," *Proc. Inst. Radio Eng.*, vol. 25, no. 7, 1937.

[9] H. T. FRIIS and W. n. LEWIS, "Radar antennas," *Bell Syst. Tech. J.*, vol. XXVI, no. 2, 1947.

[10] A. Kuchar, M. Taferner, M. Tangemann, and C. Hoek, "Field Trial With a Gsm /

Dcs1800 Smart Antenna Base Station," in *IEEE VTS 50th Vehicular Technology Conference*, 1999, pp. 42–46.

[11] H. Im, S. Hyeon, W. Lee, and H. Bahk, "Implementation of smart antenna base station for IS-2000 1X," in *The 57th IEEE Semiannual Vehicular Technology Conference, 2003. VTC 2003-Spring.*, 2000, vol. 1, pp. 582–586.

[12] K. Maichalernnukul and S. Jitapunkul, "A combined blind beamforming and interference cancellation for a smart antenna system in MC-CDMA base station," *IEEE 60th Veh. Technol. Conf. 2004. VTC2004-Fall. 2004*, vol. 1, no. 1, pp. 155–159, 2004.

[13] ArrayComm, "A Fully Adaptive Approach to Smart Antennas," San Jose.

[14] A. Goldsmith, "Designing Reliable Wi-Fi for HD Delivery throughout the Home," Fremont, 2009.

[15] I. C. Society, "IEEE Std 802.11ac," New York, 2013.

[16] 3GPP, "Overview of 3GPP Release 8 V0.3.3," 2014.

[17] 3gpp, "Overview of 3GPP Release 10 V0.2.1 (2014-06)," 2014.

[18] 3gpp, "3GPP TS 38.201 V15.0.0 Technical Specification Group Radio Access Network; NR; Physical layer." 2017.

[19] 3gpp, "3GPP TS 38.300 V15.2.0 Technical Specification 3rd Generation Partnership Project;NR and NG-RAN Overall Description." 2018.

[20] 3gpp, "R4-1700199_NR specific beamforming new requirements for NR." 2017.

[21] J. Zhang, W. Wu, and D. G. Fang, "Single RF channel digital beamforming multibeam antenna array based on time sequence phase weighting," *IEEE Antennas Wirel. Propag. Lett.*, vol. 10, pp. 514–516, 2011.

[22] M. T. Islam, N. Misran, and B. Yatim, "Smart antenna UKM testbed for digital

beamforming system," *EURASIP J. Adv. Signal Process.*, vol. 2009, 2009.

[23] R. M. Rodríguez-Osorio, L. G. García, A. M. Ollero, F. J. G. M. Velázquez, L. H. De Ariet, and M. C. Ramón, "ADAM: A realistic implementation For a W-CDMA smart antenna," *EURASIP J. Appl. Signal Processing*, vol. 2004, no. 9, pp. 1384–1406, 2004.

[24] M. Sayginer and G. M. Rebeiz, "An Eight-Element 2-16-GHz Programmable Phased Array Receiver with One, Two, or Four Simultaneous Beams in SiGe BiCMOS," *IEEE Trans. Microw. Theory Tech.*, vol. 64, no. 12, pp. 4585–4597, 2016.

[25] J. Jang *et al.*, "Smart Small Cell with Hybrid Beamforming for 5G: Theoretical Feasibility and Prototype Results," *IEEE Wirel. Commun.*, vol. 23, no. 6, pp. 124–131, Dec. 2016.

[26] Y. Kim *et al.*, "Feasibility of Mobile Cellular Communications at Millimeter Wave Frequency," *IEEE J. Sel. Top. Signal Process.*, vol. 10, no. 3, pp. 589–599, 2016.

[27] A. Simonsson *et al.*, "Beamforming Gain Measured on a 5G Test-Bed," *IEEE Veh. Technol. Conf.*, vol. 2017–June, 2017.

[28] M. Thurfjell, A. Simonsson, O. Lundberg, and O. Rosin, "Narrow Beam Channel Characteristics Measured on an 5G NR Grid-of-Beam Test-bed," *2018 IEEE 87th Veh. Technol. Conf. (VTC Spring)*, pp. 1–4, 2018.

[29] K. Tateishi *et al.*, "Indoor experiment on 5G radio access using beam tracking at 15 GHz band," *IEEE Int. Symp. Pers. Indoor Mob. Radio Commun. PIMRC*, pp. 1–6, 2016.

[30] K. Hiltunen, A. Simonsson, P. Ökvist, and B. Halvarsson, "5G trial system coverage evaluation utilizing multi-point transmission in 15 GHz frequency band," in *2017 European Conference on Networks and Communications (EuCNC)*, 2017, pp. 1–5.

[31] K. Nishimori, R. Kudo, N. Honma, Y. Takatori, and M. Mizoguchi, "16x16 Multiuser MIMO Testbed Employing Simple Adaptive Modulation Scheme," in *VTC Spring 2009 - IEEE 69th Vehicular Technology Conference*, 2009, pp. 1–5.

[32] Y. Inoue *et al.*, “Field Experimental Trials for 5G Mobile Communication System Using 70 GHz-Band,” in *2017 IEEE Wireless Communications and Networking Conference Workshops (WCNCW)*, 2017, pp. 1–6.

[33] T. Obara, Y. Inoue, Y. Aoki, S. Suyama, J. Lee, and Y. Okumura, “Experiment of 28 GHz Band 5G Super Wideband Transmission Using Beamforming and Beam Tracking in High Mobility Environment,” in *IEEE 27th Annual International Symposium on Personal, Indoor, and Mobile Radio Communications (PIMRC)*, 2016, pp. 1–5.

[34] J. Gozalvez, “Fifth-Generation Technologies Trials [Mobile Radio],” *IEEE Veh. Technol. Mag.*, vol. 11, no. 2, pp. 5–13, Jun. 2016.

[35] G. Liu, X. Hou, F. Wang, J. Jin, H. Tong, and Y. Huang, “Achieving 3D-MIMO With Massive Antennas From Theory to Practice With Evaluation and Field Trial Results,” *IEEE Syst. J.*, vol. 11, no. 1, pp. 62–71, Mar. 2017.

[36] N. Instruments, “5G Massive MIMO Testbed: From Theory to Reality,” 2017.

[37] A. Nordrum, “5G Researchers Set New World Record For Spectrum Efficiency,” *IEEE Spectr.*, 2016.

[38] C. Shepard *et al.*, “Argos: Practical Many-antenna Base Stations,” in *Proceedings of the 18th Annual International Conference on Mobile Computing and Networking*, 2012, pp. 53–64.

[39] E. Everett, C. Shepard, L. Zhong, and A. Sabharwal, “SoftNull: Many-Antenna Full-Duplex Wireless via Digital Beamforming,” *IEEE Trans. Wirel. Commun.*, vol. 15, no. 12, pp. 8077–8092, Dec. 2016.

[40] T. H. Ismail and M. M. Dawoud, “Null steering in phased arrays by controlling the element positions,” *IEEE Trans. Antennas Propag.*, vol. 39, no. 11, pp. 1561–1566, Nov. 1991.

[41] R. T. Al-Mushcab, M. M. Dawoud, and H. A. Ragheb, “Null steering in adaptive arrays

by controlling the elevations of the antenna array elements," in *Proceedings of IEEE Antennas and Propagation Society International Symposium and URSI National Radio Science Meeting*, 1994, vol. 2, pp. 1244–1247 vol.2.

[42] J. A. Hejres, "Null steering in phased arrays by controlling the positions of selected elements," *IEEE Trans. Antennas Propag.*, vol. 52, no. 11, pp. 2891–2895, Nov. 2004.

[43] C. L. Dolph, "A Current Distribution for Broadside Arrays Which Optimizes the Relationship between Beam Width and Side-Lobe Level," *Proc. IRE*, vol. 34, no. 6, pp. 335–348, Jun. 1946.

[44] R. L. Haupt, "Linear and Planar Array Factor Synthesis," in *Antenna Arrays: A Computational Approach*, IEEE, 2010.

[45] R. C. Hansen, *Phased Array Antennas*. Wiley, 2009.

[46] R. S. Elliot, *Antenna Theory and Design*. Wiley India Pvt. Limited, 2006.

[47] T. T. Taylor, "Design of line-source antennas for narrow beamwidth and low side lobes," *Trans. IRE Prof. Gr. Antennas Propag.*, vol. 3, no. 1, pp. 16–28, Jan. 1955.

[48] Y. Hua, Y. Ma, A. Gholian, Y. Li, A. C. Cirik, and P. Liang, "Radio self-interference cancellation by transmit beamforming, all-analog cancellation and blind digital tuning," *Signal Processing*, vol. 108, pp. 322–340, 2015.

[49] A. Gholian, Y. Ma, and Y. Hua, "A numerical investigation of all-analog radio self-interference cancellation," in *2014 IEEE 15th International Workshop on Signal Processing Advances in Wireless Communications (SPAWC)*, 2014, pp. 459–463.

[50] U. K. Revankar, K. T. Sophy, K. Sreenivasulu, and K. M. Veerabhadra, "Transmit/receiver module for active phased array antenna." Google Patents, 2004.

[51] V. Venkateswaran and A. van der Veen, "Analog Beamforming in MIMO Communications With Phase Shift Networks and Online Channel Estimation," *IEEE*

Trans. Signal Process., vol. 58, no. 8, pp. 4131–4143, Aug. 2010.

[52] T. Tanaka, R. Miura, I. Chiba, and Y. Karasawa, “An ASIC implementation scheme to realize a beam space CMA adaptive array antenna,” *IEICE Trans. Commun.*, vol. 78, no. 11, pp. 1467–1473, 1995.

[53] I. Chiba, R. Miura, T. Tanaka, and Y. Karasawa, “Digital beam forming (DBF) antenna system for mobile communications,” *IEEE Aerosp. Electron. Syst. Mag.*, vol. 12, no. 9, pp. 31–41, 1997.

[54] D. D. Curtis, R. W. Thomas, W. J. Payne, W. H. Weedon, and M. A. Deaett, “32-Channel X-band digital beamforming plug-and-play receive array,” in *IEEE International Symposium on Phased Array Systems and Technology, 2003.*, 2003, pp. 205–210.

[55] I. Gupta and A. Ksienski, “Dependence of adaptive array performance on conventional array design,” *IEEE Trans. Antennas Propag.*, vol. 30, no. 4, pp. 549–553, 1982.

[56] R. Kohno, “Spatial and temporal communication theory using adaptive antenna array,” *IEEE Pers. Commun.*, vol. 5, no. 1, pp. 28–35, 1998.

[57] S. Applebaum, “Adaptive arrays,” *IEEE Trans. Antennas Propag.*, vol. 24, no. 5, pp. 585–598, 1976.

[58] V. C. Anderson and P. Rudnick, “Rejection of a coherent arrival at an array,” *J. Acoust. Soc. Am.*, vol. 45, no. 2, pp. 406–410, 1969.

[59] H. d’Assumpcao, “Overview of signal processing for arrays of receivers.,” *J. ELECT. ELECTRON. ENG. AUST.*, vol. 4, no. 1, pp. 6–19, 1984.

[60] L. C. Godara and A. Cantoni, “Uniqueness and linear independence of steering vectors in array space,” *J. Acoust. Soc. Am.*, vol. 70, no. 2, pp. 467–475, 1981.

[61] L. C. Godara, “Application of antenna arrays to mobile communications, part II: Beam-

forming and direction-of-arrival considerations," *Adapt. Antennas Wirel. Commun.*, vol. 85, no. 8, pp. 95–145, 2009.

[62] L. J. Mason, "Adaptive nulling with a multiple-beam antenna in FH/FDMA satellite communications," in *Proceedings of Canadian Conference on Electrical and Computer Engineering*, 1993, pp. 413–416 vol.1.

[63] P. Angeletti, "Multiple Beams From Planar Arrays," *IEEE Trans. Antennas Propag.*, vol. 62, no. 4, pp. 1750–1761, Apr. 2014.

[64] Q. Xue, X. Fang, and C. Wang, "Beamspace SU-MIMO for Future Millimeter Wave Wireless Communications," *IEEE J. Sel. Areas Commun.*, vol. 35, no. 7, pp. 1564–1575, Jul. 2017.

[65] O. L. Frost, "An algorithm for linearly constrained adaptive array processing," *Proc. IEEE*, vol. 60, no. 8, pp. 926–935, Aug. 1972.

[66] K. Ahmed and R. Evans, "An adaptive array processor with robustness and broad-band capabilities," *IEEE Trans. Antennas Propag.*, vol. 32, no. 9, pp. 944–950, 1984.

[67] L. E. Brennan and L. S. Reed, "Theory of adaptive radar," *IEEE Trans. Aerosp. Electron. Syst.*, no. 2, pp. 237–252, 1973.

[68] M. Nagatsuka, N. Ishii, R. Kohno, and H. Imai, "Adaptive array antenna based on spatial spectral estimation using maximum entropy method," *IEICE Trans. Commun.*, vol. 77, no. 5, pp. 624–633, 1994.

[69] J. Capon, "High-resolution frequency-wavenumber spectrum analysis," *Proc. IEEE*, vol. 57, no. 8, pp. 1408–1418, 1969.

[70] R. Schmidt, "Multiple emitter location and signal parameter estimation," *IEEE Trans. Antennas Propag.*, vol. 34, no. 3, pp. 276–280, Mar. 1986.

[71] R. W. Klukas and M. Fattouche, "Radio signal direction finding in the urban radio

environment.," in *PROC NATL TECH MEET INST NAVIG, INST OF NAVIGATION, ALEXANDRIA, VA(USA), 1993,* 1993, pp. 151–160.

[72] T. Gebauer and H. G. Gockler, "Channel-individual adaptive beamforming for mobile satellite communications," *IEEE J. Sel. areas Commun.*, vol. 13, no. 2, pp. 439–448, 1995.

[73] A. Barabell, "Improving the resolution performance of eigenstructure-based direction-finding algorithms," in *ICASSP '83. IEEE International Conference on Acoustics, Speech, and Signal Processing*, 1983, vol. 8, pp. 336–339.

[74] R. Roy and T. Kailath, "ESPRIT-estimation of signal parameters via rotational invariance techniques," *IEEE Trans. Acoust.*, vol. 37, no. 7, pp. 984–995, 1989.

[75] Dassault, "CST 2017."

[76] M. A. Johnson, "Phased-array beam steering by multiplex sampling," *Proc. IEEE*, vol. 56, no. 11, pp. 1801–1811, Nov. 1968.

[77] R. Blanco and M. Manteghi, "A new sampling scheme for digital phased arrays," in *2013 IEEE Antennas and Propagation Society International Symposium (APSURSI)*, 2013, pp. 109–110.

[78] M. Manteghi and R. Blanco, "A Novel Technique for a Low-Cost Digital Phased Array Design," *IEEE Trans. Antennas Propag.*, vol. 61, no. 7, pp. 3495–3501, Jul. 2013.

[79] R. Ekholdt, "Adaptive Interference Cancellation in Nyquist Rate Scanned Arrays," *IEEE Trans. Aerosp. Electron. Syst.*, vol. AES-11, no. 3, pp. 359–362, May 1975.

[80] P. B. Kenington, *RF and Baseband Techniques for Software Defined Radio*. Artech House, 2005.

[81] H. Chen, T. Lin, H. T. Kung, C. Lin, and Y. Gwon, "Determining RF angle of arrival using COTS antenna arrays: A field evaluation," in *MILCOM 2012 - 2012 IEEE Military*

Communications Conference, 2012, pp. 1–6.

[82] G. Soni, G. Kaur, and V. K. Banga, “Implementation amp;amp; BER Analysis of 2×2 MIMO Using USRP 2920- Universal Software Radio Peripheral,” in *2016 Second International Conference on Computational Intelligence Communication Technology (CICT)*, 2016, pp. 523–527.

[83] E. A. Ball, “A cost-effective technique for concurrent IQ stream capture for prototyping phased arrays,” *IET Conf. Proc.*, p. (1), Jan. 2017.

[84] M. Donelli and C. Sacchi, “Implementation of a low-cost reconfigurable antenna array for SDR-based communication systems,” *IEEE Aerosp. Conf. Proc.*, 2012.

[85] C. Sheldon, J. Bradfield, E. Sanchez, J. Boye, D. Copeland, and N. Adams, “UHF Phased Array Ground Stations for Cubesat Applications,” *Annu. AIAA/USU Conf. Small Satell.*, no. 240, pp. SSC16-IX-01, 2016.

[86] A. Stockman, N. Glavmo, and A. Stockman, “Software Development For a Radar Application Based on SDR Technology,” CHALMERS TEKNISKA HÖGSKOLA, 2014.

[87] M. Lin and L. Yang, “Blind calibration and DOA estimation with uniform circular arrays in the presence of mutual coupling,” *IEEE Antennas Wirel. Propag. Lett.*, vol. 5, pp. 315–318, 2006.

[88] B. Friedlander and A. J. Weiss, “Direction finding in the presence of mutual coupling,” *IEEE Trans. Antennas Propag.*, vol. 39, no. 3, pp. 273–284, Mar. 1991.

[89] K. R. Dandekar and and, “Smart antenna array calibration procedure including amplitude and phase mismatch and mutual coupling effects,” in *2000 IEEE International Conference on Personal Wireless Communications. Conference Proceedings (Cat. No.00TH8488)*, 2000, pp. 293–297.

[90] S. Tahcfulloh and G. Hendrantoro, “Phased MIMO radar with coherent receive arrays,”

in *2017 International Conference on Signals and Systems (ICSigSys)*, 2017, pp. 72–76.

[91] S. Chaudhary and A. Samant, “Characterization and calibration techniques for multi-channel phase-coherent systems,” *IEEE Instrum. Meas. Mag.*, vol. 19, no. 4, pp. 44–50, Aug. 2016.

[92] P. M. Freitag and S. R. Forrest, “A coherent optically controlled phased array antenna system,” *IEEE Microw. Guid. Wave Lett.*, vol. 3, no. 9, pp. 293–295, Sep. 1993.

[93] R. Sorace, “Phased array calibration,” *IEEE Trans. Antennas Propag.*, vol. 49, no. 4, pp. 517–525, Apr. 2001.

[94] E. Lier, M. Zemlyansky, D. Purdy, and D. Farina, “Phased array calibration and characterization based on orthogonal coding: Theory and experimental validation,” in *2010 IEEE International Symposium on Phased Array Systems and Technology*, 2010, pp. 271–278.

[95] C. T. Charles and D. J. Allstot, “A Calibrated Phase and Amplitude Control System for a 1.9 GHz Phased-Array Transmitter Element,” *IEEE Trans. Circuits Syst. I Regul. Pap.*, vol. 56, no. 12, pp. 2728–2737, Dec. 2009.

[96] K. Nishimori, K. Cho, Y. Takatori, and T. Hori, “Automatic calibration method using transmitting signals of an adaptive array for TDD systems,” *IEEE Trans. Veh. Technol.*, vol. 50, no. 6, pp. 1636–1640, Nov. 2001.

[97] 3GPP, “TS 36.211 version 10.0.0 Release 10; Evolved Universal Terrestrial Radio Access (E-UTRA); Physical channels and modulation,” *Tech. Specif.*, vol. 0, p. 9, 2011.

[98] J. K. Thomas, L. L. Scharf, and D. W. Tufts, “The probability of a subspace swap in the SVD,” *IEEE Trans. Signal Process.*, vol. 43, no. 3, pp. 730–736, 1995.

[99] M. Rice, *Digital Communications: A Discrete-time Approach*. Pearson/Prentice Hall, 2009.